

**Polarization, Passivation, Intercalation, and Generation:  
An Examination of In-Situ and Ex-Situ Analytical Techniques for  
the Study of Carbon Anode Materials for the Electrochemical  
Generation of Elemental Fluorine.**

By

**Kelvin S.-H. Seto**

A Thesis Submitted in Partial Fulfillment  
of the Requirements for the Degree of

Master of Applied Science

In

The Faculty of Energy Systems and Nuclear Science  
Nuclear Engineering

University of Ontario Institute of Technology

December 2011

©Kelvin Seto, 2011

## Abstract

The field of industrial fluorine generation has not made significant progress in the past 60 years due to the difficulty and hazards surrounding the use of hydrofluoric acid (HF) and fluorine gas. This work examines various carbon materials for their use as electrodes in the electrochemical generation of elemental fluorine. An experimental apparatus was designed and constructed to melt and maintain the temperature of the  $\text{KF}\cdot 2\text{HF}$  electrolyte in a suitable range for electrochemical measurements. An electrochemical cell was designed and tested for operations in a highly corrosive atmosphere at elevated temperatures. The importance of safe operating procedures surrounding HF is outlined in this work. Various in-situ electrochemical techniques were used to study the ability of the different carbon anode materials in their ability to carry out the fluorine discharge reaction (FDR) as well as study the growth of passivating film. Ex-situ analytical techniques were used to examine the microstructure and composition of the carbon materials before and after electrochemical polarization. The results suggest that the level of non-carbon impurities had the most significant effect on the ability of the carbon material to carry out the FDR efficiently at most potentials tested. The results show that multiple analytical techniques are required to obtain a better understanding of a chemical system, and that no single method can be used to fully explain a single set of results.

## Acknowledgements

First of all, I would like to thank my family for their support throughout this whole ordeal, and my friends for reminding me that there is life outside of work/school.

I would like to thank Cameco Corporation for their generous financial support.

I would like to thank various members of Cameco ITD&RC for their valuable discussions, expertise, and making this project possible.

I would like to thank Dr. Bradley Easton for the use of the TGA instrument and Dr. Liliana Trevani for use of the Raman instrument during the course of this project.

I would like to thank Mr. Andrew Prior for his assistance and generosity in the construction of the electrochemical cell.

I would like to thank various members of the Ikeda research group, past and present for laying the groundwork to make all the work I have currently done, easier.

I would like to thank Dr. Ranganathan Santhanam for his knowledge, valuable discussion, and assistance in various aspects of this project.

Last but not least, I would like to thank my supervisor, Dr. Brian Ikeda for his patience, knowledge, and words of encouragement through this experience. As well as teaching me all that I currently know about electrochemistry.

## Table of Contents

List of Figures .....	vii
List of Tables .....	x
Terminology.....	xi
1. Introduction.....	1
1.1. Background .....	1
1.1.1. Application of Fluorine in the Nuclear Industry .....	1
1.1.2. Background on Fluorine Generation .....	1
1.1.3. Application of Carbon Electrodes .....	2
1.1.4. Issues in the Fluorine Generation Process.....	3
1.2. Objective .....	4
2. Literature Review.....	6
2.1. Carbons for Electrochemical Applications .....	6
2.1.1. Background.....	6
2.1.2 Basic Amorphous Carbon Precursors.....	8
2.1.3. Graphite .....	8
2.1.4. Pyrolytic and Highly-Oriented Pyrolytic Graphite.....	10
2.1.5. Graphite Intercalation Compounds (GICs) .....	11
2.1.6. Vitreous Carbon.....	12
2.1.7. Amorphous Carbons.....	13
2.2. Fluorine and the Fluorine Evolution Reaction .....	14
2.2.1. Background.....	14
2.2.2. Application of Fluorine in the Nuclear Industry .....	15
2.2.3. Industrial Generation of F <sub>2</sub> .....	17
2.2.4. Electrochemical Response in the C/KF·2HF System.....	19
2.2.5. Passivation.....	21
2.2.6. Influence of Water in the C/KF·2HF System.....	23
2.2.7. Graphite Fluorides, CF <sub>x</sub> .....	26
2.2.8. Polarization.....	28
2.2.9. Intercalation.....	30
2.2.10. Bubble Formation.....	35
2.3. Galvanostatic Discharge Studies .....	39
2.3.1. Background.....	39
2.3.2. Deintercalation Process/Mechanism .....	41

2.3.3. Carbon Cathode Materials .....	44
3. Theory .....	46
3.1 Raman Spectroscopy .....	46
3.2 EIS .....	46
3.2.1. Electrochemical Impedance Spectroscopy Theory and Model .....	46
3.2.2. Description of Circuit Diagram .....	47
3.2.3. Simplifying a Circuit Diagram .....	49
3.2.4. Calculation of Double-Layer Thickness.....	51
3.3. Galvanostatic Discharge Studies .....	51
4. Experimental .....	53
4.1. Materials, Supplies, Chemicals .....	53
4.1.1. Carbon Anode Materials.....	53
4.1.2. Chemicals and Materials .....	53
4.2. Experimental Apparatus .....	55
4.2.1. Cell Heater Design Features and Construction .....	55
4.2.2. Electrochemical Cell Design Features and Construction .....	59
4.2.3. Instrumentation.....	63
4.3. Experimental Methods .....	65
4.3.1. Operating Personal Safety Measures .....	65
4.3.2. Methodology.....	69
4.4. Sample Experimental Procedure .....	77
4.5. Characterization of Carbon Electrode Materials by TGA.....	79
4.5.1 Background.....	79
4.5.2. Sample Impurity .....	79
4.5.3. Summary.....	82
5. Results.....	86
5.1. Polarization Experiments .....	86
5.1.1. Steady State Currents ( $I_{ss}$ ) .....	86
5.1.2. Charge vs. Potential.....	86
5.1.3. Cyclic Voltammetry .....	92
5.2. Raman Spectroscopy Results .....	99
5.3. Electrochemical Impedance Spectroscopy (EIS) .....	104

5.3.1. CF <sub>x</sub> Film Thicknesses.....	104
5.4. Galvanostatic Discharge Experiments .....	109
6. Discussion.....	113
6.1. Polarization Experiments .....	113
6.1.1. Sustainable Rate of Reaction.....	113
6.1.2. Electrode Effectiveness for Fluorine Generation .....	115
6.1.3. Electrode Passivation.....	116
6.1.4. Summary of Polarization Studies .....	118
6.2. Raman Spectroscopy .....	120
6.3. Electrochemical Impedance Spectroscopy .....	121
6.3.1. Capacitance and Surface Layer Relationship .....	121
6.3.2. Discussion of the Capacitance and Surface Layer .....	122
6.4. Galvanostatic Experiments.....	125
6.5. Discussion Summary .....	127
7. Concluding Remarks.....	133
8. Recommendations for Future Work.....	136
9. References.....	138
Appendices.....	145

## List of Figures

Figure 2.1	Representation of Crystal Analogs of Carbon	7
Figure 2.2	Cross-section of an Industrial Electrochemical Fluorine Generation Cell	18
Figure 2.3	Sample Voltammetric Curve for Graphite in $\text{KF}\cdot 2\text{HF}$	20
Figure 2.4	Effect of Passivation of Graphite on Subsequent Potential Sweeps in $\text{KF}\cdot 2\text{HF}$	22
Figure 2.5	Representation of Fresh and Fluorinated Electrode Surfaces	23
Figure 2.6	Graphite and Different Stages of Fluorine-Intercalated Compounds	32
Figure 2.7	Raman Spectra of Fluorinated Graphite	34
Figure 2.8	Fluorine Bubble Evolved on Carbon Electrode	36
Figure 2.9	Process of Fluorine Bubble Evolution and Detachment	37
Figure 2.10	“Fluidized Layer” Model of Carbon/Fluorine Interface	38
Figure 2.11	Galvanostatic Discharge Curve for $\text{C}_{1.4}\text{F}$	43
Figure 2.12	Galvanostatic Discharge Curves for Various Graphite Fluorides and Oxyfluorides	45
Figure 3.1	Raman Spectrum of Graphite	47
Figure 3.2	Circuit Model and Representation of $\text{C}/\text{KF}\cdot 2\text{HF}$ Interface for Non-Uniform Microstructure	49
Figure 3.3	Circuit Model and Representation of $\text{C}/\text{KF}\cdot 2\text{HF}$ Interface for Uniform Microstructure	50
Figure 4.1	Image of Assembled Cell Electrolyte Heater	56
Figure 4.2	Circuit Diagram of Cell Electrolyte Heater	57
Figure 4.3	Schematic of Heater Compartment for Cell Electrolyte	58
Figure 4.4	Image of Fully Assembled Electrochemical Cell	60
Figure 4.5	PTFE Cell Lid	61
Figure 4.6	PTFE Gas Shroud and Electrode Holders	62

Figure 4.7	Images of Rod, Block, and Plate Electrodes	64
Figure 4.8	Photograph of Full Personal Protective Equipment	67
Figure 4.9	Photograph of Cu/CuF <sub>2</sub> Reference Electrode	69
Figure 4.10	Photograph of Ag/AgI Reference Electrode	71
Figure 4.11	Selection of Potential for in Double-Layer Region	76
Figure 4.12	Representation of CF <sub>x</sub> Layer as Electrical Double-Layer	77
Figure 4.13	TGA of Carbon Anode Materials in Ar	80
Figure 4.14	TGA of Graphite Rod in Ar	82
Figure 4.15	TGA of Vitreous Carbon in Ar	83
Figure 4.16	TGA of Carbon Rod in Ar	83
Figure 4.17	TGA of Toyo Tanso Amorphous Carbon in Ar	84
Figure 4.18	TGA of Cameco Amorphous Carbon in Ar	84
Figure 4.19	TGA of Coal-Tar Pitch in Ar	85
Figure 5.1	Potentiostatic Response of Graphite Rod Polarized from 4.0 to 8.0 V	87
Figure 5.2	Potentiostatic Response of Carbon Rod Polarized from 4.0 to 8.0 V	87
Figure 5.3	Potentiostatic Response of Toyo Tanso Carbon Polarized from 4.0 to 8.0 V	88
Figure 5.4	Potentiostatic Response of Cameco Carbon Polarized from 4.0 to 8.0 V	88
Figure 5.5	Potentiostatic Response of Vitreous Carbon Polarized from 4.0 to 8.0 V	89
Figure 5.6	Steady State Current Density vs. Potentials from 4.0 to 8.0 V	90
Figure 5.7	Charge vs. Potential for Different Carbon Materials	91
Figure 5.8	Total Cumulative Charge Over Polarization Series vs. Potential for Different Carbon Materials	91
Figure 5.9	Voltammograms of Graphite Rod Initially and After Fluorination	94

Figure 5.10	Photograph of Fluorine Bubble on Graphite Rod	95
Figure 5.11	Voltammograms of Toyo Tanso Initially and After Fluorination	96
Figure 5.12	Voltammograms of Cameco Amorphous Carbon Initially and After Fluorination	97
Figure 5.13	Voltammograms of Vitreous Carbon Initially and After Fluorination	98
Figure 5.14	Raman Spectra of Non-Fluorinated Carbon Materials	100
Figure 5.15	Raman Spectrum of Initial and Immersed Graphite Rod	100
Figure 5.16	Raman Spectrum of Graphite Rod Following Polarizations	101
Figure 5.17	Raman Spectrum of Toyo Tanso Amorphous Carbon Following Polarizations	103
Figure 5.18	Raman Spectrum of Cameco Amorphous Carbon Following Polarizations	103
Figure 5.19	Nyquist and Bode Plots for Graphite Rod Polarized at 6 V After 2340 s	107
Figure 5.20	Nyquist and Bode Plots for Graphite Rod Polarized at 6 V After 2640 s	108
Figure 5.21	Fluorine Discharge from Graphite at Various Current Densities	110
Figure 5.22	Tafel Plot for Discharge of Fluorine Ions	111
Figure 5.23	Discharge Curves for $CF_x$ CPE vs. Fluorinated and Fresh Graphite Rods	112

## List of Tables

Table 1.1	Physical Properties of Various Carbon Materials	9
Table 3.1	Fitted Values for Simple and Complex Circuit Models of Graphite	50
Table 4.1	Selected Carbon Anode Materials and the Commercial Source	53
Table 4.2:	Carbon-PTFE Electrode Samples	53
Table 4.3:	Parts List for Cell Electrolyte Heater	59
Table 4.4:	List of Personal Protective Equipment	66
Table 4.5:	Operations and Required Personal Protective Equipment	66
Table 5.1:	Initial Peak Intensity Ratios of Carbon Materials	99
Table 5.2:	Summary of Peak Intensity Ratios and Shifts Following Polarization	102
Table 5.3:	Measured Capacitance Values and Calculated $CF_x$ Layer Thickness	105
Table 5.4:	Calculated Amount of Intercalated Fluorine and Discharge Times	111
Table A3.1:	Full Table of Fitted Data for EIS Results	149

## Terminology

**aHF:** anhydrous hydrogen fluoride

**Anode:** electrode where the oxidation takes place

**CE:** counter electrode. Electrode that helps pass the current flowing through the cell; the current travels between the working electrode and the counter electrode

**Cathode:** electrode where the reduction takes place

**Cell Potential (E[V]):** the sum of electrical potentials within an electrochemical cell that also accounts for all redox processes occurring at the electrodes

**CF<sub>x</sub>:** graphite fluorides. Carbon fluorine materials containing covalent C-F bonds, normally containing high concentration of F atoms

**C<sub>x</sub>F (or F-GICs):** fluorine-graphite intercalation compounds. Carbon fluorine materials containing ionic or semi-ionic C-F bonds, normally at a low concentration

**Covalent bonding:** a type of bonding in which electrons are shared by atoms

**CPE:** carbon paste electrode

**CV:** cyclic voltammetry. A potential sweep method in which the voltage applied to the cell is increased at a constant rate in one direction, before being swept in the return direction

**Electrochemical Cell:** device that involves the presence of faradaic currents as a result of redox chemical reactions; it can be either a galvanic cell, when the reactions are spontaneous, or an electrolytic cell, when the reactions are non-spontaneous

**EIS:** electrochemical impedance spectroscopy

**Electrode:** it represents an electrical conductor/semiconductor in an electrochemical cell; in electrochemistry, it is the conductive phase where the electron transfer occurs; it can be an anode or a cathode

**Electrolytic Cell:** energy-consuming device that converts electrical energy into chemical energy; it consists of at least two electrodes and an electrolyte solution; cathode is negative as compared to the anode

**FDR:** fluorine discharge reaction. The reaction involving the splitting of HF at the carbon anode to yield an absorbed F· radical, which may lead to fluorination of the surface, F<sub>2</sub> formation, or reaction of F· and other gases present. This may be used to describe a region above 4.0 V (vs. Cu/CuF<sub>2</sub>)

**FEP:** fluorinated ethylene propylene

**FER:** fluorine evolution reaction. The reaction involving the formation of F<sub>2</sub> gas

**GF (also, CF<sub>x</sub>):** graphite fluoride

**GFO/GOF:** graphite oxyfluoride

**GO:** graphite oxide

**GIC:** graphite intercalation compound. A graphitic material with intercalated ions, in which the conductivity is higher than natural graphite

**Half-cell:** the anode or the cathode compartment of an electrochemical cell, including all reactions that occur at that particular electrode

**Half-reaction:** the redox reaction that occurs in one half-cell, either at the anode or at the cathode

**HF:** hydrogen fluoride (or, hydrofluoric acid)

**HOPG:** highly oriented pyrolytic graphite. A highly ordered form of graphite containing long-range order. It is considered to be a single crystal of pure graphite.

**Interface (Junction):** in an electrochemical cell, it represents the location where two distinct phases come in contact with each other: solid-liquid (electrode-solution), two liquids of different concentrations and/or compositions (reference electrode-solution), etc.

**Ionic bonding:** the electrostatic attraction between oppositely charged ions.

**IR:** infrared spectroscopy

**NMR:** nuclear magnetic resonance spectroscopy

**NHE/SHE:** Normal/Standard Hydrogen Electrode. The standard reference electrode; all standard potentials are referred to NHE; its potential is by definition 0.000 V

**OCP:** open-circuit potential. The potential associated with an electrode when all redox processes are in equilibrium; the net current is zero under these conditions and the electrode potential is given by the Nernst equation

**Overpotential ( $\eta$  [V]):** deviation of the electrode/cell potential from its equilibrium value,  $\eta = E - E_{eq}$ ; it can either be positive or negative

**Oxidation:** refers to the process in which a chemical species loses one or more electrons and an increase in oxidation state

**Oxidized Species/Oxidizing Agent/Oxidant (O):** the chemical species that undergoes the reduction, enabling the oxidation of a different species

**PAN:** polyacrylonitrile. A semi-crystalline organic polymer with a repeating mer unit of  $(C_3H_3N)_n$

**Potentiometry:** electrochemical methods that utilize near zero currents and have the output potential readings vs. time, using the Nernst equation to find analyte concentrations

**PMP:** polymethylpentene. A chemically resistant, transparent, thermoplastic

**PPE:** personal protective equipment

**PTFE:** polytetrafluoroethylene. A high molecular weight polymer consisting of only carbon and fluorine atoms. It has a mer unit of  $(C_2F_4)_n$

**PG:** pyrolytic graphite. A highly uniform form of graphite

**Redox:** a reaction in which one or more electrons are transferred

**Reduction:** refers to the process in which a chemical species gains one or more electrons (a decrease in oxidation state)

**RE:** reference electrode. Electrode that can maintain a constant potential under changing experimental conditions; the WE potential is referenced vs. the RE potential; REs are typically anodes in electrochemical cells

**RS:** raman spectroscopy

**Supporting Electrolyte:** an ionic substance (typically a salt) that is present in a solution

to ensure its conductivity; the supporting electrolyte reduces the migration effects in the solution; it does not undergo redox chemistry, and thus its ions are called spectator ions. Sometimes the supporting electrolyte is referred to as the electrolyte

**STM:** scanning tunnelling microscopy

**Voltammetry:** electrochemical methods that utilize a potential ramp (e.g., increase or decrease with time) and have the output current vs. potential

**WE:** working electrode. Electrode where the redox processes under study occur

**XPS:** x-ray photoelectron spectroscopy

**XRD:** x-ray diffraction

# 1. Introduction

## 1.1. Background

### 1.1.1. Application of Fluorine in the Nuclear Industry

Fluorine has been produced industrially for the past 70 years, a majority of that production going towards the nuclear industry for the isotopic enrichment of fuel for nuclear reactors [1]. A unique characteristic of fluorine that makes it especially suited for the task is that it has only one naturally occurring isotope,  $^{19}\text{F}$ . In addition forming the only volatile compound of uranium that is relatively chemically stable,  $\text{UF}_6$ , the masses of individual molecules of  $\text{UF}_6$  differ only by the number of neutrons in the uranium atom. Thus, it makes it possible to separate the fissile isotope of uranium,  $^{235}\text{U}$ , from  $^{238}\text{U}$  through a host of techniques such as ultracentrifugation or gaseous diffusion [2].

Other applications of fluorine include its use in metallurgy (etching surfaces for analysis), the preparation of semi-conductors, organic fluorochemicals, sulphur hexafluoride, and other inorganic fluorides [1].

### 1.1.2. Background on Fluorine Generation

Fluorine is the ninth element in the periodic table and is the most reactive of all the elements. Fluorine was first isolated by Henri Moissan in 1886 by an electrochemical method using anhydrous hydrofluoric acid (aHF) as the media (the solvent) [3]. At this time, fluorine was generated simply by the electrolysis of aHF containing a small concentration of potassium fluoride. The overall reaction for the generation of molecular fluorine is:



The process used by Moissan was, overall, inefficient and costly for several reasons. First, anhydrous HF had to be prepared by thermal decomposition of potassium bifluoride,  $\text{KF}\cdot\text{HF}$ , but it was necessary to cool the cell below room temperature to reduce the partial pressure of HF over the electrolyte [1,4]. HF is an extremely hazardous gas at room temperature, and work with fluorine had claimed many lives through the early stages of research. Second, aHF has very low conductivity, and required a large

input of energy to produce  $F_2$ , due to high resistance in the solution [5]. Finally, the HF media and evolved  $F_2$  gas caused extensive corrosion to the platinum positive electrode (anode), which was considered to be one of the most corrosion resistant elements in a fluorine atmosphere.

Developments in the fluorine generation system include the use of a high temperature cell ( $>239\text{ }^\circ\text{C}$ ) [1], that utilized molten  $\text{KF}\cdot\text{HF}$  as the electrolyte for fluorine generation, rather than  $\text{aHF}$ . The presence of  $\text{KF}$  increased the conductivity of the media, lowering the energy requirement to produce  $F_2$ . Next, increasing the concentration of  $\text{HF}$  in the electrolyte to yield  $\text{KF}\cdot 2\text{HF}$  lowered the operating temperature because it has a melting point of only  $71.7\text{ }^\circ\text{C}$  [6]. The higher concentration of  $\text{HF}$  in the electrolyte also delayed the frequency at which the electrolyte had to be replaced due to the depletion of  $\text{HF}$ . Platinum electrodes were also replaced with graphite electrodes, and later with non-graphitized carbon electrodes [1,5]. Since this work was carried out in the mid-1950s, there has been little very little progress improve the industrial fluorine generation process. Almost all modern industrial fluorine generation cells use  $\text{KF}\cdot 2\text{HF}$  as the electrolyte media at  $\sim 85\text{ }^\circ\text{C}$  with non-graphitized anodes in mild steel cells, that also serve as the cathode [1,5].

### 1.1.3. Application of Carbon Electrodes

Carbon is an interesting element and material due to the range of physical properties it is capable of, depending on the type of bonding involved. Carbon has 4 valence electrons and can form stable bonds with three or four other atoms ( $\text{sp}^2$ - or  $\text{sp}^3$ -hybridization). This variety in bonding gives rise to the two well-known crystalline forms of carbon: graphite ( $\text{sp}^2$ -hybridized) and diamond ( $\text{sp}^3$ -hybridized). While graphite is considered to be soft and electronically semi-conducting, diamond is the hardest material on earth and is electronically insulating [7,8]. Graphite is composed of planar sheets of carbon atoms (called graphene) that has long-range uniform C-C bonding in two dimensions, diamond is composed of tetrahedrally bonded carbon atoms giving three dimensional uniformity. The electron configurations about the carbon atoms yield the different electronic properties.

Carbons, in general, are particularly well-suited for electrochemical applications because

they have relatively low chemical and electrochemical reactivity, are relatively inexpensive (except for in the case of diamond), and are available in a variety of physical structures [8]. The characteristic of graphite that makes it unsuitable for fluorine generation (but highly favoured in electronic applications) is the sheets of carbon that make up its microstructure. During electrochemical fluorination, fluorine atoms are inserted between individual layers of graphene (called intercalation), causing the material to physically expand. Repeated expansion in the liquid media led to sheets of carbon layers exfoliating from the electrode, resulting in the disintegration of the graphite electrode [5]. For this reason, non-graphitized carbon anodes are used. Non-graphitized carbon anodes have the low chemical and electrochemical reactivity, are still considered inexpensive, but most of all, avoid the issue of electrode degradation.

#### **1.1.4. Issues in the Fluorine Generation Process**

The generation of fluorine, however, is not a simple process. There are three products from the fluorine discharge reaction (FDR) on the surface of the carbon electrode: electrode passivation, electrode intercalation, and fluorine generation [5,9]. Electrode passivation is the formation of a protective, insulating layer on the surface of a material that inhibits the electron transfer mechanism. In the case of carbon electrodes, fluorine generation in  $\text{KF}\cdot 2\text{HF}$  media causes the formation of a  $\text{CF}_x$  layer, which is not only electronically insulating, but also causes the electrode surface to be non-wetting to the electrolyte. The repelling effect of the surface limits the transfer of electroactive species to the electrode, and in general, inhibits the fluorine generation process.

Electrode intercalation is a process in which small ions insert into the microstructure (particularly carbon). The intercalated species the electronic properties of the material and, in the case of intercalated fluorine, modifies the mechanism for producing fluorine gas. Finally, fluoride discharge to produce fluorine gas is simply the electrochemical oxidation of fluoride ions to produce fluorinated gaseous products from the surface of the electrode.

The combination of processes, in addition to the relatively low conductivity of the  $\text{KF}\cdot 2\text{HF}$  electrolyte, leads to the requirement of large overvoltages ( $>6$  V) in order to keep a cell running at an optimal rate. These large operating voltages require a large

input of electricity, introduce an additional hazard to workers, and increase the operating costs to the nuclear field as a whole. By understanding the fundamental effects of the FDR on carbon electrodes, one may be able to develop novel electrode materials that improve the overall efficiency of fluorine generation.

## 1.2. Objective

By building an understanding of the underlying chemical properties and processes involved with various aspects of fluorine generation, to improve existing electrode designs or develop novel carbon electrodes. The primary issues involved with the generation of elemental fluorine include passivation, bubble adhesion, and subsequent polarization of the carbon electrode. These issues can be traced back to the properties of the materials: chemistry, microstructure, surface structure, and so on. In this thesis various carbon materials were selected and their applicability as anode materials for fluorine generation compared on the basis of electrochemical and microstructural characteristics. The goal is to examine why non-graphitized carbons are used as electrodes for fluorine generation. This work will involve the use of various *in situ* electrochemical methods for the examination of chemical processes between fluorine and carbon electrodes ( $F_2$  generation and passivation), as well as *ex situ* spectroscopic and compositional analysis techniques to examine the microstructural changes due to intercalation and the chemical composition of the electrode materials. The suitability of each analytical technique for the evaluation of passivation, intercalation, and generation of fluorine on different carbons will be determined.

Using that goal as a guideline, the research is designed to achieve the following objectives:

- Develop a general understanding of electrochemical performance of various carbon anode materials for the fluorine evolution reaction;
- Determine the effectiveness of different carbon materials as anodes for the generation of elemental fluorine, based on the generalized categories of graphitic, amorphous, or vitreous carbons;

- Determine whether the thickness of  $\text{CF}_x$  surface layers can be estimated using impedance measurements on carbon materials of different compositions, microstructures, and surface structures;
- Determine whether galvanostatic discharge experiments can be used to evaluate and estimate the amount of fluorine that is electrochemically intercalated in graphitic materials, as opposed to chemically fluorinated graphite powders; and
- Determine whether the design, construction, and operation of the cell electrolyte heater and electrochemical cell were successful for use in fluorine generation research.

Details regarding the background of carbon anode materials are given in chapter 2. A general review of processes and issues surrounding fluorine production, including electrode passivation and polarization are also given in chapter 2. Chapter 3 involves the theory behind some of the analytical techniques that are used in this work. Chapter 4 describes the experimental apparatus and work required to carry out the current study. Results of the series of electrochemical and analytical experiments are provided in chapter 5. A discussion of the results is provided in chapter 6. Finally, chapter 7 and 8 contains the conclusions and recommendations for future work, respectively.

## 2. Literature Review

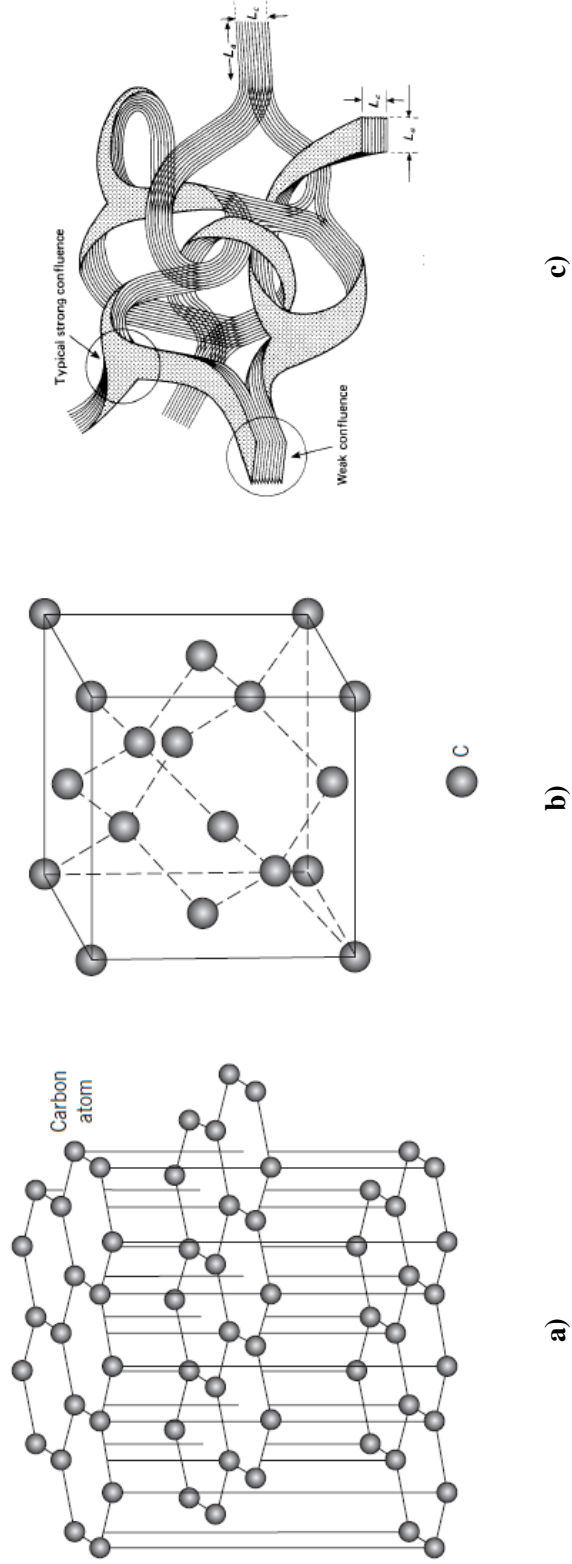
### 2.1. Carbons for Electrochemical Applications

#### 2.1.1. Background

Carbon is the sixth element in the periodic table and is part of the Group IVA elements containing 4 valence electrons. Carbons have an uncommon feature in that there are two naturally occurring crystalline allotropes of pure carbon: graphite and diamond. The two crystalline forms are highly dissimilar in physical, chemical, and electrochemical properties due to the characteristic bonding involved. Whereas graphite is composed of  $sp^2$ -hybridized carbon atoms arranged in planar sheets (Fig. 2.1a), diamond is composed of  $sp^3$ -hybridized carbon atoms bonded in a three-dimensional, tetrahedral configuration (Fig. 2.1b). The arrangement of bonding electrons in the carbon atom defines their properties. Whereas graphite has three  $\sigma$ -bonded electrons and one  $\pi$ -electron, all of the valence electrons in diamond are bonding. The delocalized  $\pi$ -electrons are “free” and give rise to the highly conductive properties of graphite. The fully  $\sigma$ -bonded diamond lattice has no delocalized electrons and is an electrical insulator. Conversely, whereas graphite is soft owing to a lack of direct interplanar bonding, diamond has exceptional strength due to the chemical bonding in three-dimensions. The amorphous form of carbon is made up of mixed hybridizations and has a spectrum of physical, chemical, and electrochemical properties between graphite and diamond.

Carbon is a widely used material for electrodes because of its relatively low chemical and electrochemical reactivity, as well as its availability in a wide variety of physical structures [8]. It may be used as either the electrode itself, or as conductive support for other electrochemically active material. The decomposition potential for the oxidation or reduction of the solvent or electrolyte is usually the determining factor for the useful potential limits for carbon electrodes. In aqueous solutions, the practical potential range for a carbon electrode is limited by two background processes: hydrogen evolution and oxygen evolution [8]. Graphite electrodes can be used at more positive and negative potentials than platinum in the same aqueous electrolyte: 1.3 to -1.3 V at pH values between 1 and 7 [8]. In addition to a wide potential range, other advantages of carbon

**Fig. 2.1: Representation of Crystal Analogs of Carbon**



Representations of crystalline analogs of carbon: a) graphite, showing  $sp^2$ -hybridized carbon atoms; b) diamond, showing  $sp^3$ -hybridized carbon atoms; and c) vitreous carbon, showing interwoven graphitic ( $sp^2$ -bonded carbon) ribbons. Used with permission from [10,11].

electrodes are a relatively high electrical and thermal conductivity, low thermal expansion, high purity, and relatively low cost [8]. A table of physical properties of various carbon materials, as well as copper alloy and platinum (common electrode materials) are given in Table 1.1.

### 2.1.2 Basic Amorphous Carbon Precursors

**Petroleum coke** is a heavy residue of high-boiling polyaromatic compounds from petroleum refining. It is the purest form of carbon available in large quantities and is now the principle raw material for the manufacture of graphite products. Among all the carbon materials, petroleum coke is considered the most graphitizable of all raw materials commonly used as fillers because it develops the highest degree of crystallinity upon treatment to temperatures of 2500 °C or higher [12].

**Carbon black** is produced commercially by thermal or oxidative decomposition of various hydrocarbons. Particle sizes of carbon blacks have an average diameter ranging from 20 to 300 nm. Surface area determination studies by nitrogen adsorption have found that carbon blacks generally have surface areas between 10 and 500 m<sup>2</sup>/g [12]. Carbon blacks play a major role as a structural component, conductive support, and electrocatalyst in batteries and fuel cells.

**Coal-tar pitch** is produced from the distillation of coal tar and is, therefore, a by-product of the production of metallurgical coke. Coal-tar pitch consists of a complex mixture of predominantly aromatic hydrocarbons and various heterocyclic compounds. It has a high specific gravity, a high carbon content (>93%), and exhibits a broad softening range at temperatures used in the molding and extrusion of carbon products [12]. Coal-tar pitch is the most commonly used binder in manufactured carbon materials.

### 2.1.3. Graphite

Graphite is a crystalline form of carbon consisting of sp<sup>2</sup>-hybridized carbon atoms in a trigonal bonding conformation. It has a layered structure, in which carbon atoms form sheets of condensed hexagonal rings with a C-C bond distance of 0.142 nm (Fig. 2.1a) [13]. The delocalized electron gives the C-C bond a partial double-bond character. Consecutive layers overlap in a staggered, ABAB, configuration and are held together

**Table 1.1: Physical Properties of Various Carbon Materials**

Physical Property	Artificial Graphite (extruded)	Glassy Carbon	Amorphous Carbon	Diamond (synthetic)	Copper (alloys)	Platinum (commercially pure)
<b>Bulk density</b> (g·cm <sup>-3</sup> )	1.6 – 1.71 * , ‡	1.3 – 1.55 *	1.4 – 1.8 †	3.2 – 3.515 †, ‡	8.25 – 8.94 ‡	21.45 ‡
<b>Gas permeability</b> (cm <sup>2</sup> ·s <sup>-1</sup> )	10 <sup>-2</sup> *	10 <sup>-6</sup> – 10 <sup>-12</sup> *	Varies over wide range	Unavailable	Unavailable	Unavailable
<b>Tensile strength</b> (MPa)	13.8 – 41.2 * , ‡	39.2 – 98.0 *	Varies over wide range	800 – 1400 ‡	220 – 1310 ‡	125 – 240 ‡
<b>Coefficient of thermal expansion</b> (10 <sup>-6</sup> (°C) <sup>-1</sup> )	1 – 2.7 * , ‡	2 – 3.5 *	Unavailable	0.11 – 1.23 ‡ (natural)	16.2 – 20.5 ‡	9.1 ‡
<b>Thermal conductivity</b> (W/m·K)	125.5 – 190 * , ‡	4.2 – 25.1 *	Unavailable	3150 ‡	29 – 388 ‡	71 ‡
<b>Electrical resistivity</b> (Ω·m)	7 × 10 <sup>-6</sup> – 20 × 10 <sup>-6</sup> * , ‡ (with grain direction)	1 × 10 <sup>-5</sup> – 5 × 10 <sup>-5</sup> *	Varies over wide range	1.5 × 10 <sup>-2</sup> ‡	1.72 × 10 <sup>-8</sup> – 1.15 × 10 <sup>-7</sup> ‡	10.60 × 10 <sup>-8</sup> ‡
<b>Conductivity at room temperature</b> (Ω·m) <sup>-1</sup>	2.5 × 10 <sup>6</sup> (axial direction) †	10 <sup>4</sup> – 10 <sup>5</sup> †	10 <sup>-5</sup> – 10 <sup>-14</sup> †	10 <sup>-16</sup> †	1.52 × 10 <sup>-7</sup> ‡	9.43 × 10 <sup>-6</sup> ‡
<b>Hardness</b> (kg mm <sup>-2</sup> )	Varies over wide range	800 – 1200 †	1250 – 6000 †	10 <sup>4</sup> †	2940 – 3580 ‡	1225 – 2350 ‡
<b>Modulus of elasticity</b> (GPa)	11 ‡	Unavailable	Unavailable	800 – 925 ‡	97 – 150 ‡	171 ‡

Physical properties of various carbon materials, copper alloys, and platinum

\*[8], †[10], ‡[14]

with weak van der Waals forces (Fig. 2.1a). The interlayer spacing of graphite is 33.54 nm [13]. The difference between covalent interplanar bonding and van der Waal interlayer bonding gives rise to the highly anisotropic properties of graphite. These are reflected in the differences in electrical conductivity, thermal conductivity, and thermal expansion in the two directions. Electrical conductivity in the direction parallel to the graphitic layers is higher than that in the perpendicular direction by a factor of 1000 [8]. Thus, graphite has metallic conductivity in the planar direction, but has semiconducting conductivity in the direction perpendicular to the graphitic layers. Similarly, thermal expansion and thermal conductivity are approximately a third and 100 times higher in the two respective directions [8]. Graphite has an electrical resistivity that is only several hundredfold higher than polycrystalline copper [8]. In addition, due to the weak interlayer bonding between lamellar sheets of graphite, small ions may intercalate between adjacent layers producing a new type of material, graphite intercalated compounds (GICs).

Although graphite occurs naturally, artificial graphite is generally made from petroleum coke. The coke is first heated to remove volatile compounds, is mixed with coal-tar pitch, and then molded or extruded into its desired form. It is further heated to about 1000 °C in a non-oxidizing atmosphere (pyrolysis) to remove other volatile constituents, and then is transformed into graphite by heat treatment between 2500 and 3000 °C [8]. Depending on the heat treatment, the resulting product is a carbonaceous material with crystalline graphitic regions oriented in multiple directions, which gives the overall material isotropic properties.

#### **2.1.4. Pyrolytic and Highly-Oriented Pyrolytic Graphite**

Pyrolytic and highly oriented pyrolytic graphite (PG and HOPG, respectively) are both forms of artificial graphite with markedly higher crystallinity (order) than regular graphite. HOPG, in particular, is analogous to a single-crystal metal because of the long-range ordered arrangement of the carbon atoms within a graphene sheet. The high degree of order in the lamellar structure at the surface makes the material quite useful for studying electrochemical reactions, molecular adsorption, and potential-induced

microstructural degradation at the atomic level. In an electrochemical system, additional care must be taken to orient the crystal properly (due to the high degree of anisotropy in the crystal). The electrochemical activity of the edge-plane sites differ greatly from the basal plane sites, as do the microstructure, chemical, and electronic properties [12]. In addition, whereas a fresh surface can be exposed by removing a thin layer of graphite on the layer plane, it is not possible on the edge-plane. Variation of the open-circuit potential (OCP) of PG and HOPG electrodes is dependent on the surface preparation technique where typical polishing will lead to cuts across deposition planes, exposing variations in crystal structures, strains, and growth sites. Thus, the most reproducible surfaces for voltammetric studies are achieved by cleaving rather than by polishing [8].

PG is produced by thermal decomposition of low molecular weight hydrocarbons, usually methane, at low pressure in the temperature range of 2100 to 2500 °C [12]. The deposited material is a polycrystalline carbon characterized by a high degree of orientation. The exact structure, however, is highly dependent on the substrate on which it is deposited, the composition and concentration of the hydrocarbon gas, the contact time between the gas and substrate, as well as the geometry of the pyrolysis chamber. HOPG is made by stress-annealing PG in the temperature range of 2200 to 3600 °C to enhance crystalline alignment and growth [8]. Being more ordered forms of graphite, PG and HOPG are also composed of a lamellar arrangement of graphene sheets in a staggered stacking pattern. As well, electrical conductivity depends on the direction of the electron flow through the crystal, but is generally higher than regular graphite.

#### **2.1.5. Graphite Intercalation Compounds (GICs)**

The layered structure of graphitic materials permits ionic and molecular species to diffuse between individual planes and form intercalation compounds. The intercalation of charged species is associated with a change in physical and electrical properties of the graphitic material. There are two general types of compounds [7]:

- Coloured, electrical conductors in which the planarity and delocalization of the  $\pi$ -electrons in the layers are retained, and
- Colourless, non-conductors of electricity in which the carbon layers become buckled owing to saturation of bonding about the carbon atom and loss of the  $\pi$ -

system.

The first class of intercalation compound is a graphite salt with ionically bonded species (either cations or anions). The intercalation of  $K^+$  ions into the lattice, for instance, increases the conductivity of graphite consistent with the addition of electrons to the delocalized  $\pi$ -system. Penetration of  $K^+$  ions between the layers causes a change to the structural framework: interlayer spacing increases and the initially staggered layers become aligned [7]. As well, these intercalated ions behave as charge carriers throughout the graphite lattice between graphene sheets, which lead to a significant increase in the interlayer conductivity in the planar direction.

The second type of compound involves intercalated species covalently bonded in a tetrahedral configuration about certain carbon atoms. For example, it can be represented by polymeric carbon monofluoride,  $CF_n$  ( $n \leq 1$ ). At low degrees of intercalation, fluorine ions are delocalized, and the electronic properties are not unlike the graphite salts previously described, and conductivity increases [7]. However, at a critical concentration, the ions become covalently bonded to the carbon lattice, and the fluorinated carbons adopt a tetrahedral bonding configuration. This bonding causes a loss of the  $\pi$ -electron system and the localization of electrons results in a loss of conductivity in the native graphite. The details of formation and properties of carbon fluorides will be discussed in more detail in section 2.2.9.2.

### 2.1.6. Vitreous Carbon

Vitreous carbon is a hard, solid form of amorphous carbon. It is often referred to as “glassy” carbon due to its glassy appearance, and fracture behaviour which is similar to that of glasses. Unlike graphite, vitreous carbon has no crystalline structure and is characterized by the isotropy of its properties (Fig. 2.1c). It has a density of 1.45 to 1.50  $g/cm^3$  and contains about 30% closed voids, accounting for its low permeability of gases and liquids [12,13]. Vitreous carbon has tensile and compressive strengths which are typically higher than those for graphite, but its electrical and thermal conductivity are lower due to a lack of crystalline graphite. The coefficient of thermal expansion is comparable to that of graphite. Vitreous carbon has many desirable properties for use as electrodes: it is electrically conductive, highly resistant to chemical attack, impermeable

to gases, and available in relatively high purity [8,12]. Due to its hardness, vitreous carbon can be easily polished to renew the electroactive surface without damaging the microstructure, which is not possible with highly crystalline graphite. In addition, glassy carbon electrodes have the widest potential range of the different kinds of carbon electrodes or other solid electrodes, particularly in mineral acids [8].

Vitreous carbon is prepared by the thermal degradation of selected organic polymers, such as polyacrylonitrile (PAN) or furfural alcohol-phenol copolymer [8,13]. Heat treatment of the polymeric precursors is carried out slowly between 1000 and 3000 °C over several days [13] to remove non-carbon atoms and produce a conjugated carbon microstructure. Since the original polymeric backbone remains largely intact, the formation of extended graphitic regions is prevented. The resulting microstructure resembles interwoven graphitic ( $sp^2$ -bonded carbon) ribbons (Fig. 2.1c), giving rise to mechanical hardness [13]. The physical properties are (overall) dependent on the maximum temperature of heat treatment. As well, due to the slow, complex technique of its manufacture, vitreous carbon is typically limited to thin rods or plates.

### 2.1.7. Amorphous Carbons

Amorphous carbon is a non-crystalline form of pure carbon. It is characterized by structural disorder and is normally found as carbon blacks, charcoal, and soot. Although it lacks large-scale order like graphite, there are naturally occurring ribbons of  $sp^2$ -bonded atoms throughout the material providing short- and medium-range order [12]. The properties of most amorphous carbons depend on the ratio of  $sp^2$  to  $sp^3$ -hybridized regions, which is commonly referred to as the degree of graphitization ( $sp^2$  bonding is the bonding type of graphite). Since amorphous carbon is a mix of  $sp^2$  and  $sp^3$  regions, amorphous carbons with high  $sp^2$  regions have electronic, optical, and mechanical properties which approach those of graphite and are quite different from amorphous carbons with high  $sp^3$  content [8]. Intermediate hybridization states exist in amorphous carbons because some atoms in the network are in highly strained configurations. As expected, amorphous carbons have physical and electronic properties that span the range between pure graphite and diamond [15].

The abundance of each type of hybridized region in the material largely depends on the

precursors, as well as the method of preparation of the carbon material. Commercially made amorphous carbons are prepared by moulding (cold isostatic pressing) or extrusion. Cold isostatic pressing uses high pressures, but little-to-no heat in the process, and as a result, the composition of the final product highly reflects the precursors used since there is very little bond transformation occurring. The amorphous carbon is less porous, and thus, denser. The extrusion process is nearly the opposite of isostatic pressing, using higher temperatures and much lower pressures. The resulting material is more porous depending on the initial precursor particle size. The density of amorphous carbon is about  $1.9 \text{ g/cm}^3$  [10].

## 2.2. Fluorine and the Fluorine Evolution Reaction

### 2.2.1. Background

Fluorine is the 9<sup>th</sup> element in the periodic table and belongs to the Group VIIA elements. Elemental fluorine is a pale yellow gas, and chemically, is the most reactive of all the elements. Fluorine is capable of reacting with all of the elements, except for the lighter noble gases. The high reactivity of fluorine is the result of a combination of the low F-F bond energy, and the high bond strength formed between fluorine and other atoms. The small size and high nuclear charge density of the fluorine atom creates a large repulsive force between F atoms and a weak overlap bonding orbitals of the atoms [16]. The high electronegativity of the F atom also accounts for many of the other differences between fluorine and the other halogens.

The synthesis of  $\text{F}_2$  is possible through a chemical process, but it is not considered to be an efficient or practical method [16]. Electrochemical synthesis is, at present, the principle method for the industrial production of elemental fluorine. The electrochemical route of fluorine generation developed by H. Moissan [3] originally used anhydrous hydrofluoric acid (aHF) as the media. The process was not particularly efficient due to the low conductivity of HF. In addition, aHF needed to be made through the thermal decomposition of potassium bifluoride,  $\text{K}^+\text{HF}_2^-$ , which caused heavy corrosion to the platinum or platinum alloy anodes used at the time [5]. The molten salt method was later

established, using molten anhydrous  $\text{KF}\cdot\text{HF}$  as the electrolyte with a graphite anode. It was later found that the addition of small amounts of  $\text{KF}$  made the  $\text{HF}$  electrolyte solution more conducting. Further development of the potassium fluoride/hydrogen fluoride,  $\text{KF}/\text{HF}$ , system first by Lebeau and Damiens [4], and later by Cady [6] yielded an electrolyte with the approximate composition of  $\text{KF}\cdot 2\text{HF}$  (40.8 wt.%  $\text{HF}$ ), with a melting point of  $71.7\text{ }^\circ\text{C}$ .

Elemental fluorine and hydrogen are produced electrochemically at the anode and cathode of the cell, respectively, according to the overall reaction:



The fluorine evolution reaction (FER) is made up of two corresponding half-cell reactions which are believed to involve the  $\text{HF}_2^-$  electrochemical species:



with a standard cell potential of  $2.85\text{ V}$  (at  $72\text{ }^\circ\text{C}$ ) [16] at the anode, and



With a standard potential of  $0\text{ V}$  at the cathode.

The overall process for fluorine generation from  $\text{HF}$  has not changed since the work was done by Moissan.

### 2.2.2. Application of Fluorine in the Nuclear Industry

Fluorine is an essential component in the enrichment of natural uranium for use as fuel in the nuclear industry. The two main isotopic forms of uranium are  $^{238}\text{U}$  and  $^{235}\text{U}$  with a natural abundance of 99.28% and 0.71%, respectively; however,  $^{235}\text{U}$  is a fissile isotope, releasing energy upon fission and is used as fuel in the form of  $\text{UO}_2$  in the majority of nuclear plants. The enrichment process takes advantage of the chemical and physical properties of fluorine and  $\text{UF}_6$ . Fluorine is used in this process because only a single stable isotope of fluorine ( $^{19}\text{F}$ ) exists naturally, and reacts with uranium to form isotopomers of volatile  $\text{UF}_6$  [17]. Isotopomers are molecules which differ in their molecular weight only by the number of neutrons in the isotopes (in this case,  $\text{U}$ ).  $\text{UF}_6$  is particularly useful, being the only volatile compound of uranium which is relatively

chemically stable, and has a low sublimation temperature (56.7 °C) [18]. The physical state of UF<sub>6</sub> makes separation of the two isotopes possible by gaseous diffusion or ultracentrifugation [2]. The content of <sup>235</sup>U in nuclear fuel can be increased to (levels up to) 3-5% after 1000 cycles by either method, from concentrations of natural uranium (0.71%). About 90% of the nuclear reactors currently in operation use this type of enriched uranium [19].

The industrial process to produce UF<sub>6</sub> goes through several steps in the dry hydrofluor method [2]. The mined uranium ore (U<sub>3</sub>O<sub>8</sub>) is first milled into a powder at high temperatures to remove organic material from the ore. Solvent extraction is then used to precipitate uranium from the milled ore. The U<sub>3</sub>O<sub>8</sub> is then purified to remove impurities such as boron, cadmium, and sodium, which may affect reactor performance [20]. The purified U<sub>3</sub>O<sub>8</sub> is then put through a fluidized bed reactor where it is maintained at a temperature of 540 to 650 °C and reduced by hydrogen [2]. The resulting product consists of mainly uranium dioxide (UO<sub>2</sub>). The crude UO<sub>2</sub> is passed on through two successive hydrofluorination fluidized bed reactors, where it is reacted with aHF at a temperature of 480 to 540 °C [2]. The chemical reaction that takes place is:



The uranium tetrafluoride (UF<sub>4</sub>) is a nonvolatile solid with a high melting point (495 to 530 °C) [2]. The UF<sub>4</sub> is treated at high temperatures with fluorine gas to form UF<sub>6</sub>, according to the reaction:



The UF<sub>6</sub> product is then further purified by fractional distillation to remove some volatile impurities. At this point, the uranium can be enriched by a host of techniques (in the form of UF<sub>6</sub> gas). The enriched UF<sub>6</sub> can then be stored in steel cylinders as a solid prior to further processing. In order to form UF<sub>6</sub> into usable pellets for use in a reactor, it is heated from the solid state into a gas which is then bubbled through water, where it reacts to form UO<sub>2</sub>F<sub>2</sub> in the water solution, according to the reaction:



The uranium solution is then mixed with ammonium hydroxide, causing the uranium to precipitate as ammonium diuranate, (NH<sub>4</sub>)<sub>2</sub>U<sub>2</sub>O<sub>7</sub>. The precipitate is dried and calcined to

form  $U_3O_8$ , which is then reduced with hydrogen to form  $UO_2$ . Finally, the  $UO_2$  is ground to form a fine, uniform powder, where it is mixed with an organic binder, pressed into a pellet, and then sintered at  $1650\text{ }^\circ\text{C}$  for 24 hours in a  $H_2$  atmosphere [2].

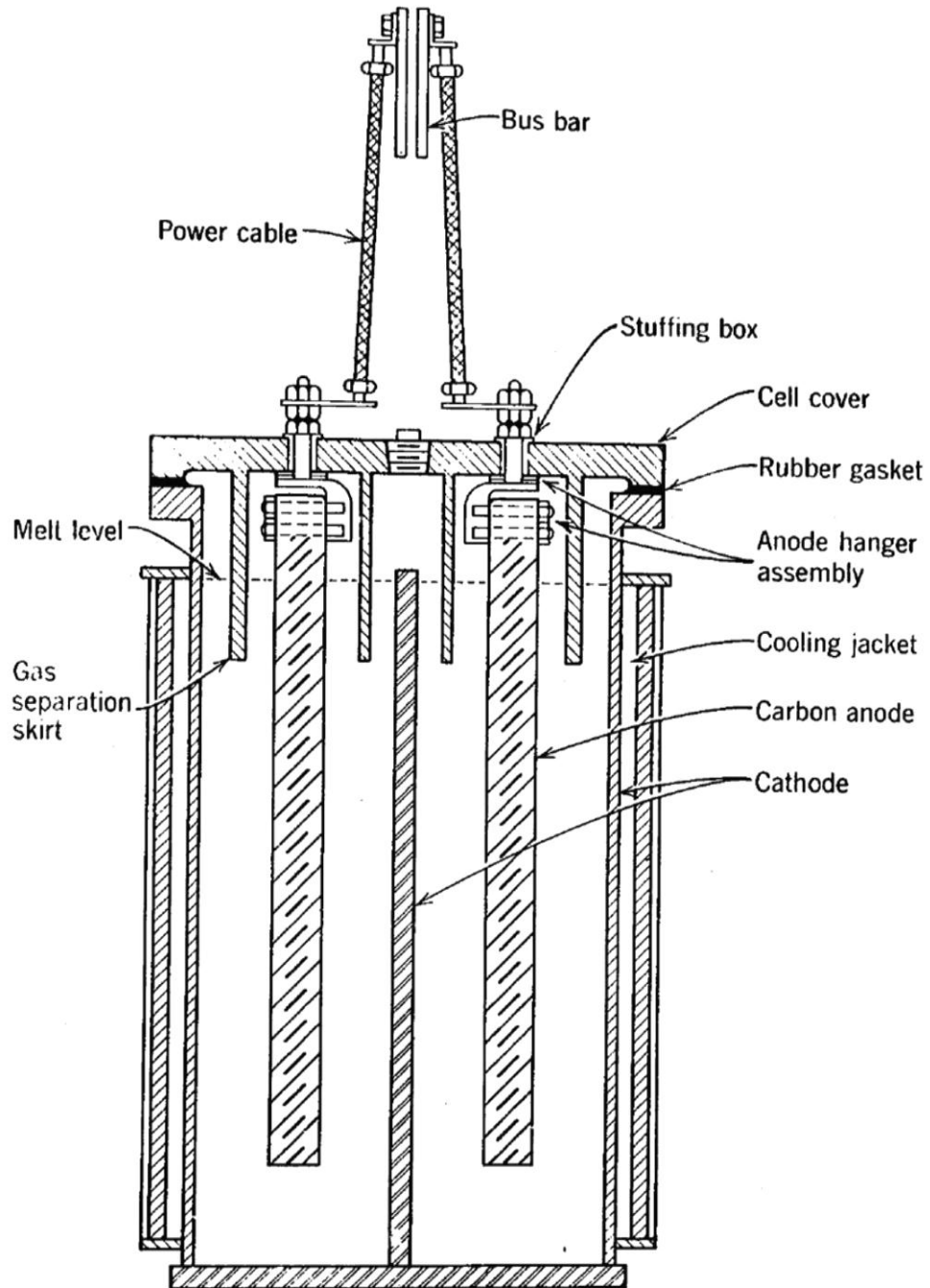
Due to the high reactivity of the fluorine atom, a single (naturally occurring) isotope of fluorine, and a low sublimation temperature for  $UF_6$ , it is clear why elemental fluorine is a critical component in the nuclear industry.

### 2.2.3. Industrial Generation of $F_2$

Modern industrial fluorine electrolysis cells operate at currents between 4 and 6 kA which produce between 2.54 and 3.47 kg of fluorine gas per hour (1500 and 2050 L  $F_2$  per hour) [1,5,19]. Most modern cells use a  $KF \cdot 2HF$  molten salt and operate at roughly  $90\text{ }^\circ\text{C}$ , which are standard conditions for what is referred to as a “medium temperature” cell (Fig. 2.2). Mild steel and Monel are the most commonly used materials for cell construction: mild steel for the cell body and cathode, Monel for the internal parts such as the skirt, diaphragm, and cooling tubes [1,5]. A Monel skirt is used to separate the hydrogen and fluorine gases formed at the cathode and anode, respectively, and prevent their explosive recombination [19]. All industrial cells currently use non-graphitized carbon as anodes. Industrial cells originally used nickel anodes, which produced fluorine without any polarization problems and could operate with electrolyte containing moisture [1]; however, the anode current efficiency was only 70% [1] and severe corrosion led to contamination of the electrolyte with metal salts. These contaminants interfered with electrolysis and prevented the recovery of large quantities of electrolyte [1]. Graphite (which replaced nickel anodes) was originally used due to the high electrical conductivity and relative chemical inertness in the electrolyte; however, exfoliation of graphitic material takes place as a result of co-intercalation of ionic species and fluorine gas between the lamellar sheets that form the graphite structure. This intercalation expands the interlayer spacing and causes graphite to lose structural integrity and degrade into a powder. The non-graphitized carbon material currently in use (made from petroleum coke, a form of amorphous carbon) does not undergo anodic dissolution, and support anode current efficiencies that are higher than 90% [5,17].

An applied voltage of 8.0 - 10.0 V between the anode and cathode is necessary to obtain

**Fig. 2.2: Cross-section of an Industrial Electrochemical Fluorine Generation Cell**



Cross-section of the Allied Chemical Corporation electrochemical industrial fluorine generation cell illustrating the configuration of the carbon anode and steel cathode, anode hanger assembly, as well as the  $F_2$  and  $H_2$  gas separation skirt. Used with permission from [1].

the current densities desired in industrial cells ( $0.12 \text{ A/cm}^2$ ) [17]. The thermodynamic potential of HF decomposition, however, is only 2.85 V (vs. SHE) [16]. The large operating voltages are primarily attributed to the reversible decomposition voltage of HF, ohmic drop in the electrolyte, and the anode overvoltage. One important contributor to the anode overvoltage in industrial configurations is the contact resistance between the carbon plate and electrical connection (the bus-bar). The brittle nature of carbon prevents the plates from being bolted tightly to the steel connections, and deterioration of the anode/bus-bar contact is one of the greatest causes of cell failure. Methods successfully used to minimize the contact resistance have included coating or impregnating the contact points of the carbon blocks with copper [1]. Although anode contact is a significant issue in industrial cells, this is not usually the case in laboratory cells. In industrial cells, the anode/bus-bar contact is usually made within the cell and is subject to attack by fluorine, HF vapour, and electrolyte. In laboratory cells, however, the carbon anode could extend through the cell cover plate and be connected in a non-corrosive atmosphere; or, a covered metal rod extended through the cover plate could be screwed into the top of a block of carbon [1].

Another major cause of anode overvoltage is bubble adhesion on the surface of the electrode, which leads to electrode polarization. This phenomenon is initiated by a  $\text{CF}_x$  passivated layer, and it ultimately limits the charge and mass transfer because the bubble behaves like a physical barrier to the surface. This limits the current to the electrode. One discontinued industrial solution to bubble-induced polarization was the use of porous electrodes, which enhanced bubble transport away from the surface, or impregnation with LiF, which improved electrode activity and conductivity [1], lowering the anode potential. While there are multiple cell configurations available on the laboratory scale, the design of industrial fluorine cells has remained largely unchanged for over half a century: medium temperature cells operating at approximately  $85 \text{ }^\circ\text{C}$  with molten  $\text{KF}\cdot 2\text{HF}$  as the electrolyte and a non-graphitized carbon anode.

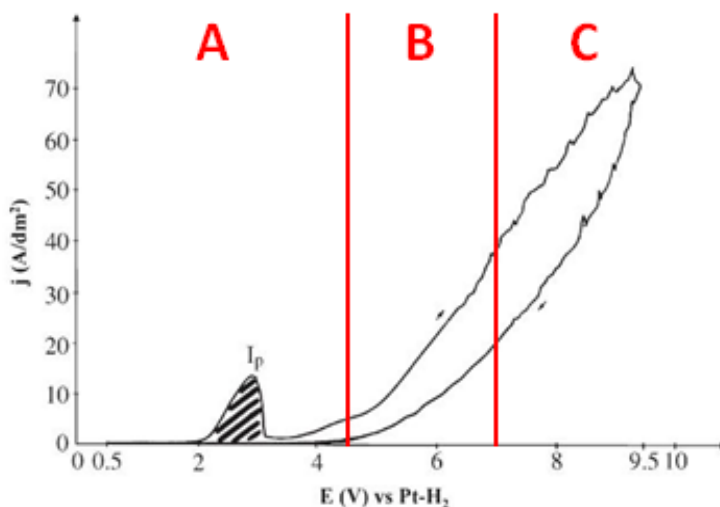
#### **2.2.4. Electrochemical Response in the C/KF·2HF System**

A spectrum of reactions involved at the C/KF·2HF interface are observed during a voltammetric sweep at potentials well above (more positive than) the range of the

fluorine discharge reaction ( $>4.0$  V) (Fig. 2.3). A critical process that occurs on the electrode (other than fluorine evolution itself) is electrode passivation. Electrode passivation and polarization is caused by the formation of a carbon fluoride passivating layer,  $\text{CF}_x$  (also called graphite fluoride). The rise and fall in current correspond to reactions that occur at the carbon/ $\text{KF}\cdot 2\text{HF}$  interface at particular potential ranges. The peak around 2.5 to 3.0 V (vs. SHE) [7] has been associated with passivation via the formation of a solid carbon-fluoride film (C-F) on the anode surface [19]. This peak is also commonly attributed to the hydrolysis of  $\text{H}_2\text{O}$ , because the standard reversible potential for  $\text{H}_2\text{O}$  occurs at 1.6 V (vs. SHE). The formation of graphite oxides during  $\text{H}_2\text{O}$  electrolysis is considered to be major cause of passivation of carbon electrodes with a C-F film, and will be discussed in section 2.2.6.

At potentials more positive than 4.6 V (Fig. 2.3, region B), the fluorine discharge reaction becomes the predominant reaction [19,21]. The evolution of highly reactive  $\text{F}\cdot$  radical and  $\text{F}_2$  at the electrode surface may lead to the formation of various gaseous compounds if they react with  $\text{H}_2\text{O}$  or other species in electrolyte ( $\text{F}_2\text{O}$ ,  $\text{COF}_2$ ,  $\text{CF}_4$ ) [22], or may

**Fig. 2.3: Sample Voltammetric Curve for Graphite in  $\text{KF}\cdot 2\text{HF}$**



Characteristic I-E curve obtained using a fresh graphite electrode in  $\text{KF}\cdot 2\text{HF}$  (sweep rate = 0.4 V/s), showing peaks corresponding to water electrolysis and/or intercalation ( $\sim 2.5$  to 3.0 V), as well as fluorine discharge and bubble evolution ( $>5.0$  V). Used with permission from [19].

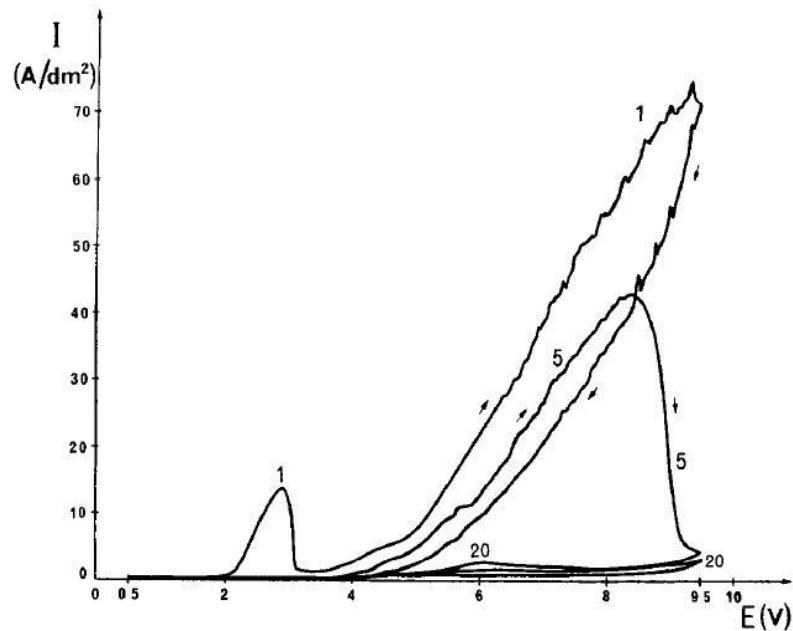
fluorinate functional groups on the carbon surface (C-O-F, C-F, CF<sub>2</sub>, CF<sub>3</sub>) [9,19,21,23-27]. The fluorinated surface is generally considered to be a 'passivating' C-F surface, because it leads to the formation of an insulating CF<sub>x</sub> layer, inhibited bubble detachment, and a host of effects that ultimately causes electrode deactivation. Electrode deactivation is the complete inhibition of reactions on an electrode due to the formation of an insulating layer, as seen by exceedingly low currents even at high potentials. Other than the reactions previously discussed, elemental fluorine is produced at this point, mixing with other gaseous fluorinated species as it leaves the cell.

At higher potentials (>7.0 V) (Fig. 2.3, region C), fluorine bubble generation becomes the predominant reaction, as seen by the jagged peaks on the voltammogram in this region [19]. The sudden rise and fall of current at elevated potentials correspond to: a) bubble nucleation (at a localized current peak), b) bubble growth (causing a gradual drop in current), and c) bubble detachment (a sharp increase in current, caused by a sudden uncovering of the surface). At high potentials or high current densities, fluorine-graphite intercalation compounds (F-GIC), C<sub>x</sub>F, undergo a transformation into graphite fluorides, CF<sub>x</sub>. Interior CF<sub>x</sub> compounds are formed when a higher concentration of fluorine intercalates cause C-F bond character to undergo an ionic-to-covalent transformation. In addition, the passivating surface C-F film grows progressively thicker and more insulating as more fluorine is discharged. The main result of electrode passivation is that there is a drop in the peak current density for subsequent scans as seen in Figure 2.4. When a certain thickness of the CF<sub>x</sub> layer is achieved, the carbon electrode is completely deactivated (e.g., sudden drop in current, Fig. 2.4), and the reaction cannot proceed unless higher potentials (or currents) are applied. Whereas previously, the decrease in current was attributed to the presence of a fluorine bubble on the surface of the electrode, electrode deactivation is caused by a sufficiently thick, insulative CF<sub>x</sub> layer which blocks further electrochemical processes from occurring.

### 2.2.5. Passivation

Passivation is a series of processes caused by the formation of a protective, insulating layer on an electroactive surface under electrochemically favorable conditions [28]. A passivating layer slows down electronic processes at the surface of electrodes, limiting

**Fig. 2.4: Effect of Passivation of Graphite on Subsequent Potential Sweeps in KF·2HF**

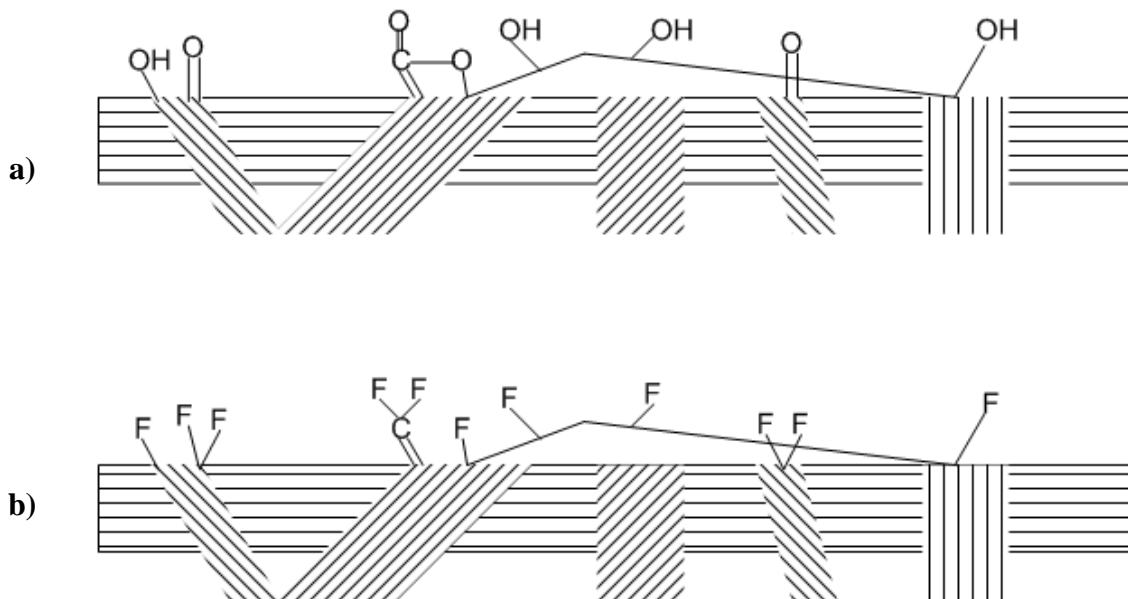


First, 5<sup>th</sup>, and 20<sup>th</sup> sweep of a cyclic voltammogram of a graphite sample polarized in KF·2HF, illustrating the effects of bubble adhesion and progressive electrode passivation on current (sweep rate = 0.4 V/s). Used with permission from [21].

the current that can be attained at any potential. In the case of carbon in a fluoride environment, a series of irreversible carbon/graphite fluoride,  $\text{CF}_x$  (where  $x < 4$ ) passivating layers are formed at potentials more positive than 3.6 V [19]. A passive layer is formed by the reaction between  $\text{F}^-$  ions and functional groups on the surface of carbon electrodes during the fluorine discharge reaction, yielding C-F and C-O-F groups (Fig. 2.5) [9]. Coverage of the electrode surface by this low surface energy  $\text{CF}_x$  film inhibits bubble detachment and lowers the wettability of the carbon anode by the KF·2HF melt. In effect, the electrode becomes both charge and mass transfer limited, leading to electrode deactivation: a condition of severely limited currents even at high potentials.

As previously mentioned, the anodic overvoltage is caused primarily by the formation of a passivating film on the surface of the carbon electrode. Most of the industrial research in this field is directed towards minimizing the anodic overvoltage to attain a more efficient and cost-effective process. Various methods have been tested at both the

**Fig. 2.5: Representation of Fresh and Fluorinated Electrode Surfaces**



Representation of functional groups on carbon electrode surface prior to exposure to fluorine-rich environment (a), and a fluorinated carbon surface (b). Adapted from [19].

industrial and the laboratory level, including the addition of additives to the electrolyte (to lower water content and intercalate metal species into the surface) [21,26,29-31], impregnation of metals into the electrode (improves conductivity and modifies surface uniformity) [25,29,31-33], and modified electrode designs (to promote bubble detachment) [34]. These methods attempted to overcome charge or mass transfer issues which limit the overall current that may be passed at a particular potential. Thus, by minimizing the formation of a passivating layer, the effects of electrode polarization by an adherent bubble or film can be avoided, making the evolution of fluorine gas occur efficiently.

### 2.2.6. Influence of Water in the C/KF·2HF System

Contamination of the electrolyte by water is a major contributor to the degree and onset of electrode passivation in the C/KF·2HF system [21,22,24,26,27,31,35-37]. In a typical fluorine generation system, water exists in low concentrations as a contaminant in the very hygroscopic KF·2HF electrolyte, but has a very large impact on the long term

operation of the cell. Minimizing water content is crucial for the prevention of electrode passivation and polarization.

During a positive going potential sweep, the peak observed around 1.6 to 2.1 V is associated with water electrolysis and passivation of the carbon electrode, i.e., the formation of a solid C-F and C-O-F film at the surface of the electrode [9,22]. The electrolysis of water occurs through the half cell reactions:

at the anode:



at the cathode:



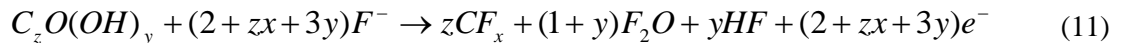
The overall reaction being:



Decomposition of water occurs at a potential of 1.6 V (vs. SHE). Water electrolysis occurring in a C/KF·2HF system will evolve O<sub>2</sub>, CO, CO<sub>2</sub>, COF<sub>2</sub>, and F<sub>2</sub>O gases [9,22] through the reaction of adsorbed O· radical intermediates with the carbon anode or fluorine ions. Passive film formation is partially caused by the fluorination of different kinds of graphite oxides (C-O, C=O), C-H, and other function groups at the surface of the electrode. Graphite oxides exist naturally on the carbon surface, or may form during water electrolysis. Graphite oxide is produced during electrolysis of adsorbed H<sub>2</sub>O molecules on carbon surfaces at low potentials (<3.0 V) according to the following reaction scheme [22,25,36-39]:



At higher potentials, intercalated oxygen in graphite oxide, C<sub>z</sub>O(OH)<sub>y</sub>, is believed to be easily exchanged with fluorine to form insulating graphite fluorides, CF<sub>x</sub> [22,25,36,37,39]:



A relationship between water concentration and the formation of passivating CF<sub>x</sub> films was identified by the onset of electrode polarization in many studies [21,22,24,26,27,31,35-37]. Nakajima et al. [26] found that approximately 20 times more

charge could be passed in a well dehydrated melt than that in a non-dehydrated melt (0.02 vs. 0.05 vol.% H<sub>2</sub>O) before the onset of polarization. Similarly, when the water content was increased from 0.01 to 0.05 vol.%, the anode potential for graphite oxide and graphite fluoride film formation on carbon electrodes were shifted to lower potentials [27]. This is indicative of an increase in the reaction of evolved O· radical with graphite during H<sub>2</sub>O electrolysis, as well as decomposition of the graphite oxide film by attack from discharged fluorine ions. The presence of water in the electrolyte ultimately leads to the generation of the CF<sub>x</sub> film on a graphite electrode.

There is evidence that the CF<sub>x</sub> surface layer itself has very little effect on the electronic properties of the passivated electrode, but has a great influence on the kinetics of the FER [37]. The FER may be completely blocked on the electrode depending on the degree of bubble adhesion on the CF<sub>x</sub> layer, especially for surface films prepared in KF·2HF containing a large amount of water. From an electronic standpoint, water has been found to disrupt the uniform crystal lattice of highly oriented pyrolytic graphite (HOPG) during electrochemical fluorination. Scanning tunneling microscopy (STM) investigations found that the hexagonal symmetry of HOPG appear to be destroyed in well hydrated (C<sub>H<sub>2</sub>O</sub> ≈ 0.06%) melt [37]. Thus, there is a loss in the physical structure which gives rise to the high electrical conductivity in graphite to begin with. This was not observed in experiments conducted in dehydrated KF·2HF melt. The overall effect of the structural disruption on conductivity of the graphitic material is dependent on the depth to which the lattice disruption occurs. Since amorphous carbon is also highly conductive but lacks the long-range graphitic order, there may not be an appreciable difference in its efficiency for the fluorine evolution reaction compared to polycrystalline graphite.

Limiting the exposure of hygroscopic KF·2HF melt to moisture is likely the most important practice in delaying the onset of water-induced, carbon anode passivation. This may be achieved by passing ‘dry’ gases through a cell to prevent the ingress of air, maintaining good seals throughout openings of the cell (also limiting HF release), and minimizing humidity in the room containing the cells. Pre-electrolysis of the melt with a sacrificial anode is a common method to remove H<sub>2</sub>O from the melt prior to fluorine generation [21,25-27,31,32,35,36,40-43]. This technique limits the degree of H<sub>2</sub>O-induced passivation on the fluorine generating working electrode. Another method

involves the addition of metal fluorides to the molten  $\text{KF}\cdot 2\text{HF}$ . Nakajima et al. [26,27] found that the addition of 3-6 wt.% LiF in conjunction with pre-electrolysis ( $C_{\text{H}_2\text{O}} \leq 0.01\text{-}0.02\%$ ) completely prevented electrode deactivation. Not only does LiF enhance charge transfer in the melt, catalyze the intercalation of  $\text{HF}_2^-$  to form a lower stage graphite intercalation compound (as well as  $\text{C}_x(\text{LiF})\text{F}$ ), and promote bubble detachment, it is also believed that water adsorption from the bulk electrolyte onto suspended LiF particles effectively removes the precursors for graphite oxide formation. It was found that  $\text{C}_x\text{F}$  compounds formed in the presence of LiF had a higher conductivity than the native HOPG, which ensures that the anode has sufficient wettability by the  $\text{KF}\cdot 2\text{HF}$  melt [26,27].

### 2.2.7. Graphite Fluorides, $\text{CF}_x$

The electrode deactivating properties of a surface graphite fluoride film are largely attributed to the chemical (rather than electrical) properties of the film [33,34,36,38]. Graphite fluorides are fluorocarbons, which refer to covalently-bonded fluorine ions in a graphitic lattice, with a composition between  $\text{CF}_{0.5}$  to  $\text{CF}$  (simplified as  $\text{CF}_x$ ). Structurally, graphite fluorides have lost the planar layers associated with graphite [36,37,39,41], and the carbons are assembled in a puckered, chair-like conformation. C-F bonds are oriented in the axial direction relative to the carbon lattice.

There are two generalized kinds of C-F surface layers that can be prepared by different methods. The first involves the *in situ* electrochemical fluorination of carbon anodes which yield conducting graphite intercalation compounds (GIC). The second involves chemical fluorination (by  $\text{F}_2$  gas) at low temperatures (275 °C) with a catalyst, which yields both conducting GICs as well as insulating  $\text{CF}_x$  compounds with a higher proportion of covalent C-F bonds [9]. These compounds limit further  $\text{HF}_2^-$  intercalation into the host structure, partially inhibiting the FER in  $\text{KF}\cdot 2\text{HF}$ , and causing the high anodic overvoltages. The  $\text{CF}_x$  layer is non-wetting to the  $\text{KF}\cdot 2\text{HF}$  electrolyte and the low surface energy inhibits fluorine bubble detachment, resulting in a smaller electroactive area [5,9,34-36,31,44,45] by the presence of a physical barrier to charge and mass transfer. The attractive forces between the carbon anode and the  $\text{F}_2$  bubble increase significantly with the formation of  $\text{CF}_x$ , since they are chemically similar. In addition,

the fluorinated surface of C-F and C-O-F groups (Fig. 2.5b) leads to the development of the F<sub>2</sub> gas film [35], which is the primary barrier for electrolyte contact with the electrode surface, even prior to bubble formation.

In one study, the thickness of the CF<sub>x</sub> film was analyzed by X-ray photoelectron spectroscopy (XPS) and was found to be as thin as ~1.7 nm, and interfacial capacitance measurements at low potentials (<4.0 V) suggests that the thickness of the CF<sub>x</sub> film was independent of the formation potential [46]. Another study, however, found that the probability of an electron passing through the CF<sub>x</sub> film decreased with increasing potential and increasing CF<sub>x</sub> film thickness [45]. These outer fluorinated layers constitute a thin insulating film whereas deeper layers of non-fluorinated carbon were characterized by good electrical conductivity [17]. Chemla and Devilliers [38] found that electron transport through the CF<sub>x</sub> layer was impeded because the probability of electron tunneling through the insulating film decreases with increasing of the film thickness (depending on the type of carbon material).

Although passive film formation may be associated with high current densities, investigations by Crassous et al. [22] found that formation of the CF<sub>x</sub> film is active even in the case of non-polarized carbon samples immersed in molten KF·2HF. Covalent and semi-ionic C-F bonds were formed and detected by both XPS and nuclear magnetic resonance spectroscopy (NMR) following immersion [22], which Crassous et al. attributed to the high reactivity of HF. Chemla and Devilliers suggested that two kinds of non-homogeneous CF<sub>x</sub> film arise, depending on the potential of the working electrode [38]. Experiments indicated the presence of a reducible C-F compound at low potentials (<4.0 V) [38,43,47], which may also indicate the reduction of intercalated C<sub>x</sub><sup>+</sup>HF<sub>2</sub><sup>-</sup> in graphite. At higher potentials, a non-reducible layer of CF<sub>x</sub> is formed [38], and the higher the potential applied to the electrode in KF·2HF, the higher the degree of fluorination (x is larger) [21]. The lack of uniformity in the composition and distribution of CF<sub>x</sub> species of the film was identified by Groult et al. using STM [36,37,41]. The group suggested that the passivated C-F films formed on carbon anodes in KF·2HF behave as electronic conductors, based on kinetic studies of the electron transfer Fe<sup>2+</sup>/Fe<sup>3+</sup> redox couple in aqueous solutions, and impedance measurements performed in Hg, using a C/C-F electrode [36,37,39,41]. However, Groult also pointed out that

multiple sites on fluorinated HOPG could not be detected since no current could be measured by the STM tip at these points, even for high bias values [36,37,39,41].

Graphite fluoride ( $\text{CF}_x$ ) films formed at high current densities ( $0.1 \text{ A/cm}^2$  or higher) are the cause of a process that is known as electrode deactivation [12]. Not only is the  $\text{CF}_x$  film itself a non-ohmic charge transfer layer, it is responsible for inhibiting  $\text{F}_2$  bubble detachment, and forming the  $\text{F}_2$  gas film, which acts as charge and mass transfer barriers from the electrolyte to the carbon anode [35,44].

### 2.2.8. Polarization

Electrode deactivation (or, polarization) on a polarization scan is visualized as a marked decrease in the limiting current (Fig. 2.4, scan 5) compared to the previous potential sweep. It is caused by the formation of a  $\text{F}_2$  gas film and lyophilic gas bubble that envelops the electroactive surface area of a passivated carbon anode [19,44]. The coverage of the solid/solution interface by a bubble results in a physical barrier for the bifluoride ion to reach the electrode surface. This type of polarization is referred to as bubble overvoltage: the additional voltage that must be applied to a system in order to maintain a particular current density or reaction rate due to the presence of the bubble. The non-wetting  $\text{CF}_x$  film causes a repulsion between the electrode and the molten  $\text{KF}\cdot 2\text{HF}$  electrolyte, further limiting the transfer of electroactive species to the surface [5,34,35,45]. These multiple processes affect charge and mass transfer, and depress the overall limiting current even with high, increasing potentials.

$\text{F}_2$  gas films are a significant contributor to the overvoltage in carbon- $\text{KF}\cdot 2\text{HF}$  systems and are electrochemically reducible [43,45,47]. Capacitance measurements of various  $\text{CF}_x$  films formed at potentials well below the reversible fluorine potential (2.85 V vs. SHE) [16] have similar electric properties and show a measure of recovery (reducibility) following polarization [45]. At high electrode potentials ( $>6.0 \text{ V}$ ), however, films exhibited lower capacitances, higher series resistances, and increased inhibition of charge transfer processes associated with the formation of highly fluorinated carbon and thicker films [45]. Various methods have been used to minimize passivation of the carbon anode [9,21,25,29,31-33,48]. One method involves the addition of specific metal compounds (e.g.,  $\text{LiF}$ ,  $\text{AlF}_3$ ,  $\text{NaF}$ ,  $\text{MgF}_2$ , or  $\text{Al}(\text{NO}_3)_3$ ) as colloidal suspensions into the molten

KF·2HF [21,26,29-31]. It is believed that a conducting ternary compound,  $CF_xM_y$ , is formed at the C/KF·2HF interface, which improves the wettability of the electrode by the melt [9,21,25,32,33,48]. “Modified” carbon electrodes were also prepared by the direct impregnation of metal fluorides into the electrodes (e.g.,  $MgF_2$ ,  $CuF_2$ , LiF, NaF,  $AlF_3$ ) [29,31] by polishing the crude carbon with a suitable polishing agent which acted as a “doping agent” [25], or by electrodeposition (e.g.,  $Ni(NO_3)_2$ ) [32]. The modified surface enhances the kinetics of the fluorine evolution reaction and the conductivity of the electrode itself [29,31,33]. Using impedance measurements, Groult et al. found low values for the electron transfer coefficient, on modified electrodes ( $\beta \approx 0.07$ ) compared to those for crude electrodes ( $\beta \approx 0.18$ ) [25]. This was attributed to formation of metal fluoride-GIC,  $C_x(MF_2)_yF$ , instead of  $CF_x$ . Higher electron transfer characteristics indicated increased wettability of the electrodes by the melt [25]. The presence of metal fluoride phases in the surface layers of the anode ( $C_xF-MF_y$ , where M = Li, Al, Ni, Mg, etc.) enhances electron transfer, whether directly from the electrolyte to the substrate or by tunneling through intermediate states of carbon orbitals, and enhances fluorine bubble detachment from the surface. Metal particles were found to catalyze the formation of conducting  $C_xF$  with ionic and/or semi-ionic C-F bonds [32], rather than insulating  $CF_x$ s. As a result, the anodic overvoltage was significantly decreased by the presence of metal fluorides [9,25]. Finally, the effects of polarization caused by an  $F_2$  gas film were also found to be minimized if a small reduction current was applied at low potentials during a voltammetric sweep. If a reducing current was applied at low potentials during a sinusoidal AC pulse, the temporary  $F_2$  gas film could be reduced and the surface was partially de-polarized for the next polarization cycle [43,47]. The overvoltage effects were found to be minimized on subsequent sweeps, suggesting that the fluorine discharge reaction could still occur efficiently on an electrode that had been passivated during a previous polarization cycle.

Activation of carbon anodes at 40 V in molten KF·2HF is a common method of electropolishing a carbon surface removing  $CF_x$  compounds [9,19,22,36,37,40,42,44,46,49]. The high potential effectively burns-off the previously formed C-F surface groups which enhances the electrochemical performance of the electrode for fluorine evolution.  $CF_x$  films formed on the activated electrodes tend to be

thinner, but have higher fluorine content. Due to the high potentials, sparking usually occurs on the surface of the electrode, which causes damage to the carbon surface. Although electrode activation has been tested industrially, it is primarily used on the laboratory scale for electropolishing electrode surfaces to reveal a reproducible surface. In addition, compared to industrial set-ups, electrode activation can only be used safely in the laboratory scale [16,40].

## **2.2.9. Intercalation**

### **2.2.9.1. General**

Intercalation is a process that involves the movement of small ions into the crystal lattice of a material, in this system, fluorine into a graphitic carbon material. Intercalates are the small ions which are inserted between the lamellar sheets of graphite and take up positions in the lattice in a manner that generates uniform spacing between adjacent ions. Graphite intercalation compounds are typically comprised of ionically bonded, positively charged species (e.g.  $K^+$ ,  $Li^+$ , etc.) as charge carriers, but may also include negatively charged ions, such as  $F^-$ . This process induces a change in the physical and electrical properties of graphite. The physical change is an increase in the interlayer spacing for instance, from  $d_{001} = 0.335$  nm in natural graphite [50] to  $d_{001} = 0.630$  nm in  $C_{1.3}F$  [51], as determined by x-ray diffraction (XRD). There is an increase in the conductivity of graphite in both the axial and planar directions due to the intercalation, because the intercalated ions behave like charge carriers between layers of graphene. The reactivity of the fluorine ion, however, results in a much different material compared with the positively charged graphite intercalation compounds, especially at high concentrations.

### **2.2.9.2. Fluorine-Graphite Intercalation Compounds**

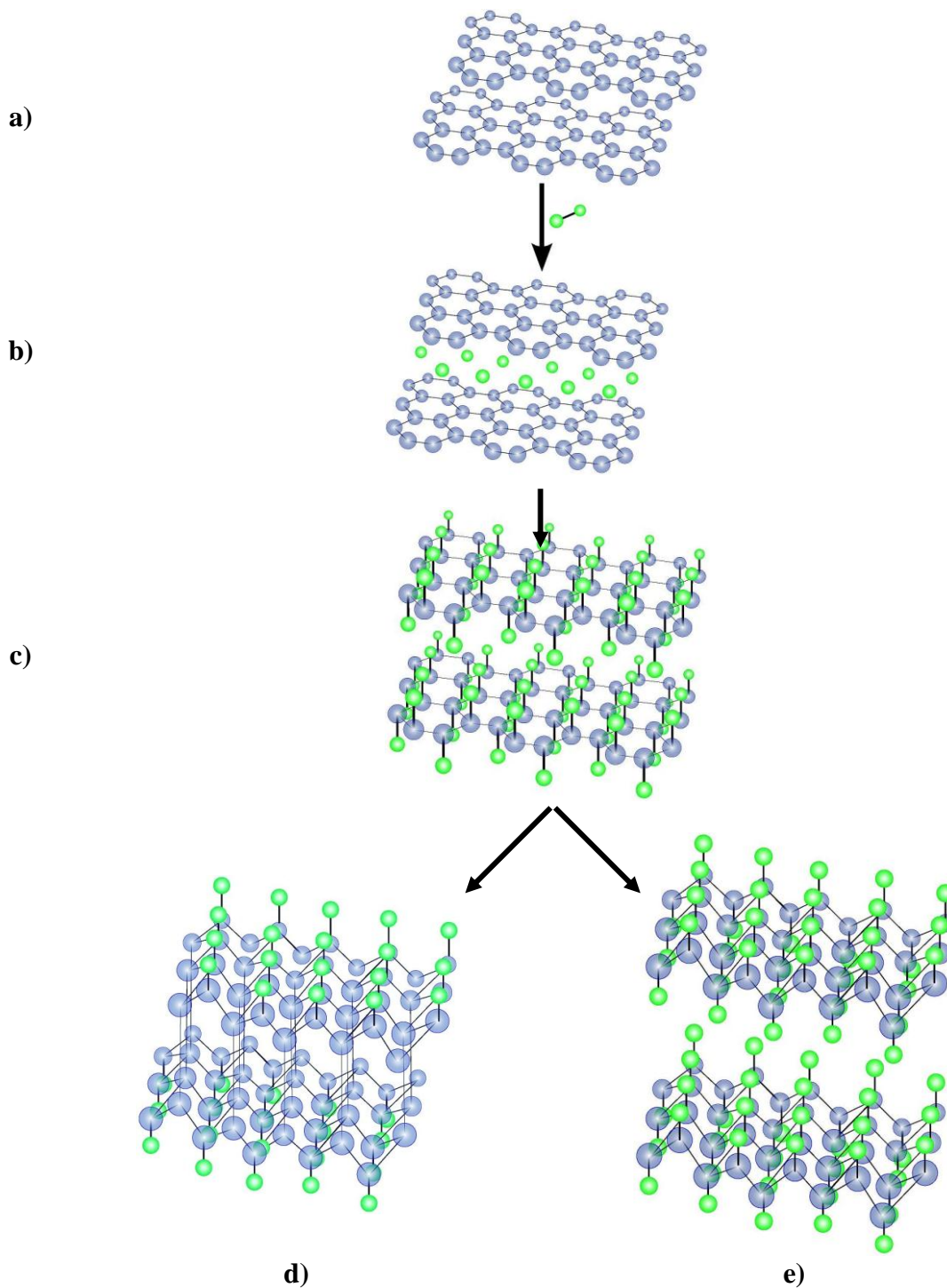
The physical and electrical properties of a fluorine-graphite intercalation compound (F-GIC) are dependent on the fluorine concentration due to the effect of fluorine bonding on the graphitic crystal lattice. The charged intercalates in F-GICs are fluorides ( $F^-$  or  $HF_2^-$ ) from the  $KF \cdot 2HF$  electrolyte. At low concentrations, fluorine intercalates remain ionically bonded within the planar, graphitic lattice and induce a positive effect on the electrical conductivity. There is a slight increase in the interlayer spacing and the

graphitic crystal lattice remains intact. At higher concentrations, the lattice becomes saturated in F<sup>-</sup> ions and a conversion in the bond character of the fluoride ion occurs. The C-F groups undergo an ionic-to-covalent change in their bonding character and the planar sheets of graphite become puckered as the F<sup>-</sup> becomes covalently bonded F (Fig. 2.6). The loss of the delocalized  $\pi$ -electron system in the graphite lattice results in a decrease in the conductivity of the graphitic material.

The amount of fluorine intercalation in graphite is roughly divided into 4 stages. Customarily, the stage of a compound is defined as the ratio of the number of host layers to the number of guest layers [52]. The ‘stage’ index determination used to classify GICs was based on XRD work by Hoffmann and Frenzel [53], and shortly later by Schleede and Wellmann [54]. For instance, a stage 1 GIC would have a layer of intercalates on alternating layers of graphite, whereas a stage 4 GIC would have a layer of intercalates between every 4 layers of graphene (the individual sp<sup>2</sup>-bonded carbon layer of which graphite is made up of, when stacked). Simply put, a stage 1 GIC would have a high concentration of intercalates, whereas a stage 4 GIC would have a low concentration of intercalates.

A stage 4 C<sub>x</sub>F has a low concentration of fluorine (C<sub>>20</sub>F) and an ionic C-F bond. The intercalation of fluorine induces an 8-fold increase in the in-plane conductivity of HOPG [55]. A stage 2-3 C<sub>x</sub>F, when 4 < x < 10, is characterized by more localized electrons indicating stronger C-F bond formation, but the interaction between C and F is essentially still ionic. The electrical conductivity of stage 2 or greater C<sub>x</sub>F’s is much higher than that of pristine pyrolytic graphite [24]. Finally, for a stage 1 C<sub>x</sub>F (2 < x < 4), the C-F bond nature shifts from almost ionic to semi-ionic [55], accompanied by a decrease in the conductivities than pristine HOPG and have a large surface free energy compared to that of covalent CF<sub>x</sub> [56]. This indicates that ionic C<sub>x</sub>F will be more easily wetted than the other graphite compounds [56], which will improve the continuous electrolysis of KF·2HF melt at a high current density without the occurrence of the anode effect [56]. From a stage 4 to a stage 1 F-GIC, the C-F bond character shifts from being ionic to more conductivity by up to a factor of 1000 [57]. Ionic stage 1 F-GICs have higher covalent (semi-ionic) with increased fluorine content. The increase in the covalent character of the

**Fig. 2.6: Graphite and Different Stages of Fluorine-Intercalated Compounds**



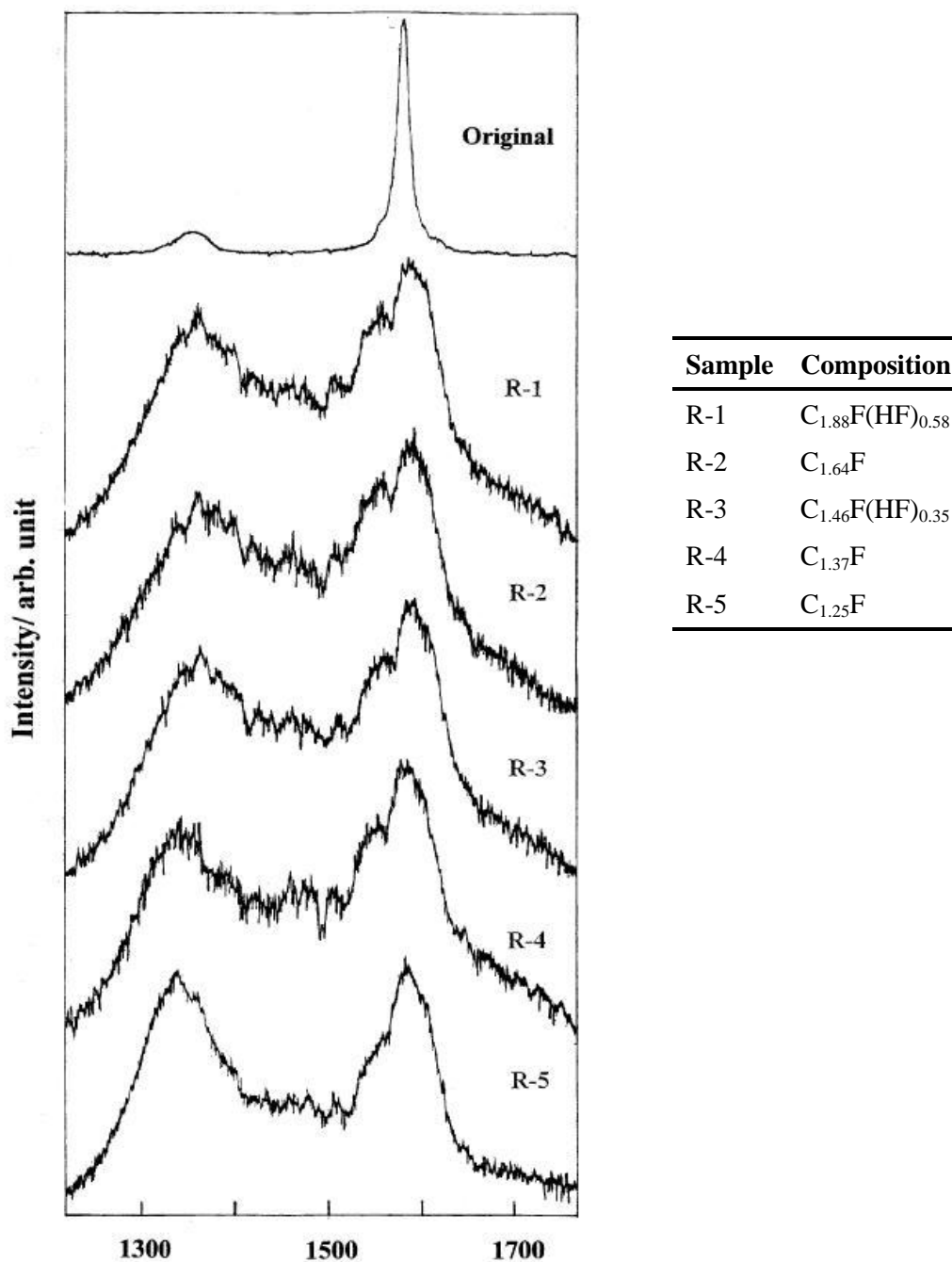
Representation of different graphitic compounds at various degrees of fluorination: (a) fresh graphite, (b)  $C_xF$ , F-GIC with ionically bonded fluorine, (c)  $CF_x$  with semi-ionically bonded fluorine, (d)  $(CF)_n$ , carbon monofluoride, (e)  $C_2F$ . Adapted from [52].

C-F bond suggests a localization of  $F^-$  ions and electrons in the lattice, which reduces the charge carrier density and causes a rapid decrease in conductivity. Based on  $^{19}F$  NMR results, there is little change in the C-F bond length [57,58]. The decrease in conductivity with increasing localization suggests that electron transport through the lattice occurs by a percolation mechanism [58], rather than a change in bond length. Thus, at higher degrees of fluorination, the ionic  $C_xF_s$  are effectively transformed into covalently bonded graphite fluorides,  $CF_x$ .

### *2.2.9.3. Spectroscopic Methods for Fluorine-Graphite Intercalation Compounds*

Raman spectroscopy is a useful tool for studying the intercalation process in graphitic materials for intercalated species of both donor and acceptor-type. In particular, there is a distinguishable difference in the charge density of graphitic layers that are in contact with an intercalated species and those that are not in contact. This suggests that Raman-active vibrational mode frequencies should show a measure of stage dependence because relative Raman vibrational intensity varies with the ratio of bounding layers (intercalate contacting) to interior layers (without contact to intercalates). In chemical fluorination experiments Gupta et al. [59] found that the Raman peaks shifted to lower frequencies with increasing fluorine concentration in  $C_xF$  (Fig. 2.7). This trend was proposed to be caused by the weakening of the C-C bonds of the graphene layers by the formation of a C-F bond [59]. The highly polarity of the C-F bond causes a decrease in the bond order between adjacent C atoms in the graphene layer, leading to a weakened (and longer) C-C bond length. As well, a splitting of the initial C-C vibrational mode ( $1555-1542\text{ cm}^{-1}$ ) of the 'ordered' graphene layer suggests the formation of two different  $C_xF$  phases,  $C_1F$  and  $C_2F$ . During the initial stages of fluorination of graphite by elemental fluorine, the fluorine is intercalated into the surface region of the graphite to form a  $C_xF$  phase with planar graphene layers. This  $C_xF$  phase changes to graphite fluoride ( $CF_x$ ) with puckered graphene layers when the fluorination is performed at higher temperatures and for longer times [59]. The XRD data indicates that interlayer spacing increases with lower GIC stage numbers because of the higher degree of intercalation and fluorination, as well as the loss of tight packing due to the formation of puckered (rather than planar) graphene layers [60].

**Fig. 2.7: Raman Spectra of Fluorinated Graphite**



Raman spectrum of graphite at various degrees of intercalation, showing depression and broadening of “ordered” graphite peak ( $\sim 1580 \text{ cm}^{-1}$ ) and growth of “disordered” graphite peak ( $\sim 1350 \text{ cm}^{-1}$ ) at higher levels of fluorination. Used with permission from [52].

The  $^{19}\text{F}$  NMR resonance pattern observed in the spectra of  $\text{C}_x\text{F}$  (where  $x > 8$ ) is believed to be attributable to the mobile fluorine acceptor species that are responsible for the increase in conductivity observed with increasing fluorine content in the dilute  $\text{C}_x\text{F}$ . The injection of carriers from the intercalated species to the graphite layers causes a transformation in the electrical characteristics from semi-metallic graphite into a metal [61]. After the conductivity of F-GIC reaches a maximum ( $x \sim 8$ ), the formation of covalent C-F bonds starts, and a gradual decrease in conductivity follows.

## 2.2.10. Bubble Formation

### 2.2.10.1. Shape/Morphology

One of the principle causes of limiting currents at high potentials in the carbon-KF·2HF system is inhibition of bubble detachment from the surface of the electrode. Under normal operating conditions, the FER is hindered by a passivating  $\text{CF}_x$  layer, in that either bubble detachment is inhibited or a surface  $\text{F}_2$  gas film covers the electrode. Blockage of the surface by the physical barrier limits the transfer of electroactive species to the surface of the carbon anode [35,40,44]. In severe cases, the  $\text{CF}_x$  passive film may become sufficiently thick that it becomes electrically insulating and, in conjunction with a surface gas film, causes electrode deactivation, completely inhibiting the fluorine discharge reaction from occurring. Bubble morphology studies have found that generated fluorinated gas species are attracted to the passivating  $\text{CF}_x$  film, yielding bubbles which are lenticular in shape (Fig. 2.8) [9,22,32,34-38,40,44,49]. That is, the bubble is flattened out over the entire surface of the electrode, with a large contact angle between the edge of the bubble and the electrode ( $\theta = 120\text{-}150^\circ$ ) [44]. This, indicates a positive attraction between the evolved fluorine gas bubble and the fluorinated carbon surface, and a negative effect on the contact of molten KF·2HF electrolyte with the carbon.

As the fluorine discharge reaction occurs, adsorbed  $\text{F}^-$  ions combine to form  $\text{F}_2$  gas at regions all over the anode (Fig. 2.9a and b) [45,62]. At a critical point of surface coverage, small bubbles that were formed and uniformly nucleated over the surface now coalesce to form a contiguous gaseous surface film on the electrode (Fig. 2.9c). This surface  $\text{F}_2$  gas film is mirror-like in appearance suggesting a thin film, and generally covers the entire active surface in a layer with uniform thickness. As bubble growth

**Fig. 2.8: Fluorine Bubble Evolved on Carbon Electrode**

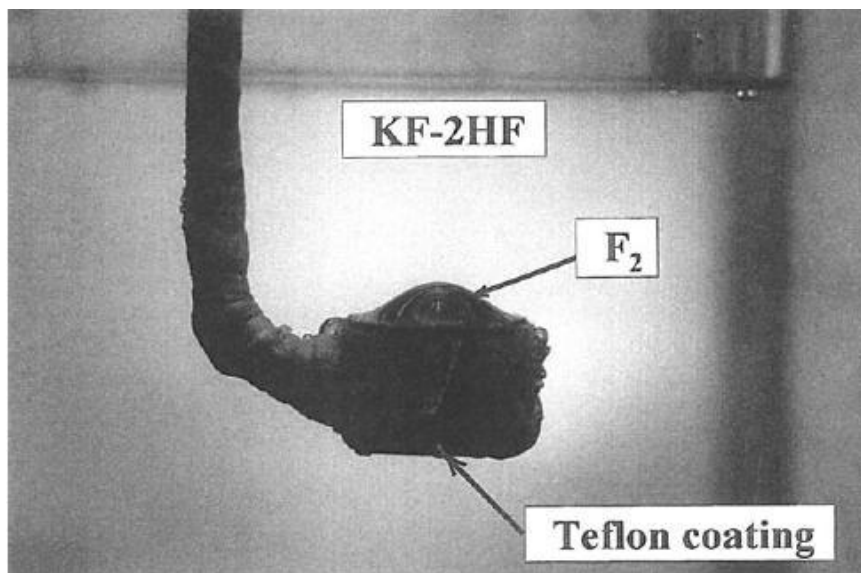


Image of a fluorine bubble evolved on a carbon electrode. Image shows the lenticular shape of the bubble on the electrode due to low surface energy  $CF_x$  passive film. Used with permission from [44].

**Fig. 2.9: Process of Fluorine Bubble Evolution and Detachment**

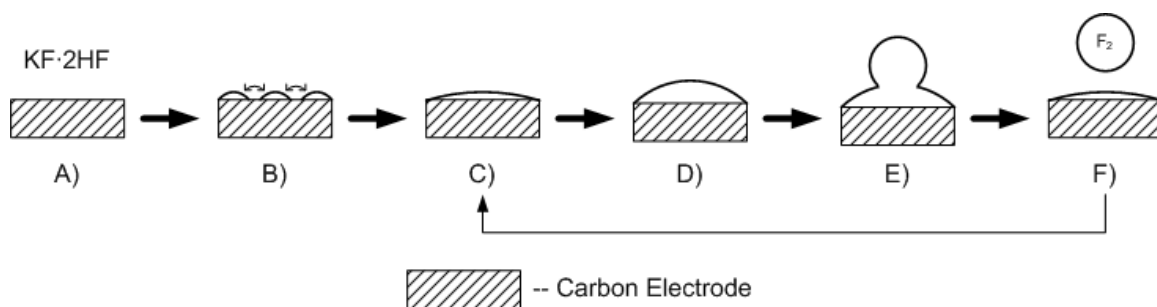


Illustration showing the various stages of bubble evolution and detachment: (a) fresh carbon electrode, (b) nucleation and coalescing of fluorine bubble, (c) fluorine gas film covering electrode, (d) early step of bubble detachment, (e) fluorine bubble detachment from surface, (f) reformation of fluorine gas film. Adapted from [44].

progresses on the electrode, the surface film begins to bow out from the middle (Fig. 2.9d), growing to a critical size (dependent on the electroactive area) and then detaches (Fig. 2.9e) [44,49]. Following bubble detachment, a thin  $F_2$  gas film remains, as smaller fluorine bubbles remaining on the surface serve as collection sites for more bubbles (Fig. 2.9f). The exact mechanism of electrolyte transport for continuous  $F_2$

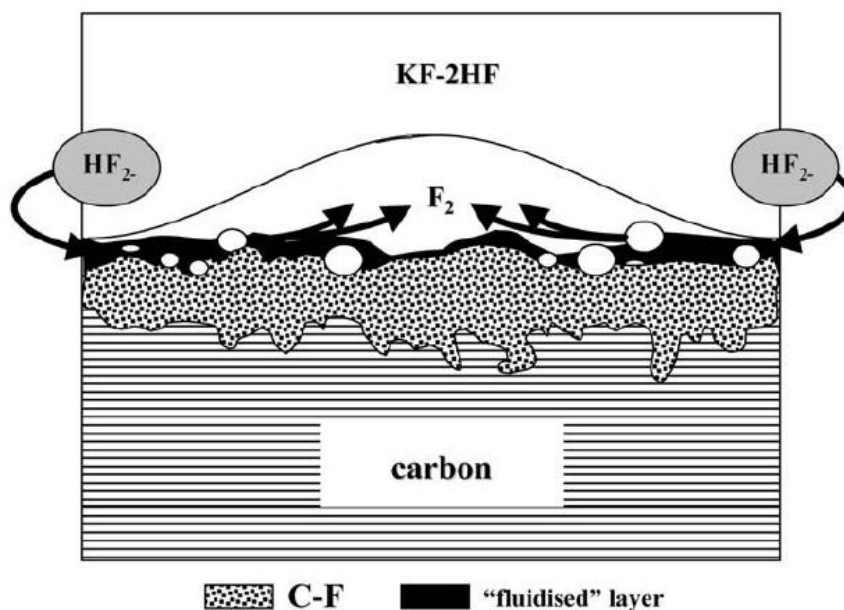
bubble formation following gas film formation is still unknown, although a “fluidized layer” model has been proposed.

Thus, the overall effect of bubble attachment on limiting the FER is twofold: first, the presence of the bubble acts as a physical barrier to the active species ( $\text{HF}_2^-$ ) reaching the surface; and second, as an insulating layer for electron transfer to the electrode [17]. Bai and Conway [35] found that higher current densities produced higher Tafel slopes which, in accordance with a C-F barrier film model, corresponded to an increase in film thickness. It was proposed that a thin gas film behaves as the initial barrier layer to charge transport via electron tunneling, leading to a type of passivation of the electrode [35]. This gas film barrier effect would be intensified by the presence of larger bubbles formed at higher current densities. This ultimately leads to the limiting currents that are commonly observed [35].

#### *2.2.10.2. Fluid Model*

A theoretical model known as the “fluidized layer” model put forth by Groult et al. (Fig. 2.10) [44] has been used to explain the transport of charge and mass to the anode surface despite complete coverage of the electrode by a gas film or bubble. This model suggests that a thin mixed phased layer comprised of liquid  $\text{KF}\cdot 2\text{HF}$  and fluorine gas exists between the passivated carbon electrode and the  $\text{F}_2$  bubble. The gas bubble sits on top of this fluidized layer, rather than directly on the electrode. When the active species (bifluoride, metal fluorides, etc.) and electrons approach the anode, they penetrate the fluid barrier to the active surface, along the edges of the bubble where it is the thinnest [44]. As well, the bubble may display a slight mushrooming effect due to the repulsion between the negatively charged bubble and the edges of the electrode holder. Once the bifluoride is incorporated into the fluidized layer, it can react with the surface of the electrode evolving fluorinated gas products, causing the bubble to grow. This model provides one possible explanation as to how the FER continues despite complete coverage of the surface by a bubble.

**Fig. 2.10: “Fluidized Layer” Model of Carbon/Fluorine Interface**



“Fluidized layer” model of the carbon-fluorine interface showing how  $\text{HF}_2^-$  can reach the electrode surface despite complete coverage by a fluorine bubble. The proposed layer consists of an electrolyte/ $\text{F}_2$  gas mixture. Used with permission from [19].

### **2.2.10.3. Detachment Studies**

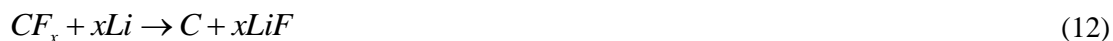
Several methods involving modified cell and electrode designs to promote bubble detachment from the surface of working electrodes were tested with varying success. Bai and Conway [35] used a rotating cone electrode to spin off evolved gases in order to distinguish whether the causes of high polarization generated by the charge transfer barrier layer is due to the  $\text{CF}_x$  film formation, inhibited  $\text{F}_2$  bubble detachment, or  $\text{F}_2$  gas film formation. The inhibition of  $\text{F}_2$  bubble detachment was found to be the principle cause of the high polarization. Another method used a vertical channel design on the anode to provide a preferential pathway for evolved gases to escape to the surface [34]. This industrial amorphous carbon anode operated for upwards of 2000 hours without polarization occurring [34]. A third method involved the impregnation of a metal fluoride into a semi-porous carbon electrode through a vacuum process [9] or with molten metal fluorides (e.g.,  $\text{AlF}_3$ ,  $\text{NaF}$ , and  $\text{LiF}$ ) [31,63]. The metallic particles

increased the conductivity of the electrode, and disrupted the uniformity of the carbon surface. This limited the critical size of the fluorine bubble before buoyant forces caused detachment of the bubble. Researchers in this case were able to run long term experiments with high current densities without the onset of the anode effect [9,63]. Finally, carbon anode activation is an effective method for electropolishing and removing the passivated  $CF_x$  layer of an electrode. Activated electrodes have smoother surfaces, and bubbles have much smaller  $C/F_2/KF \cdot 2HF$  contact angle, which show improved bubble detachment [40].

## 2.3. Galvanostatic Discharge Studies

### 2.3.1. Background

Galvanostatic experiments are constant current experiments used to determine the electrochemical response of a system forced to occur at a fixed reaction rate. One of the applications of galvanostatic studies is evaluation of the discharge properties of cathode materials used in lithium battery systems. In these primary lithium battery systems, the cathodic working electrode is a graphite fluoride, the anodic counter electrode is metallic lithium, and the electrolyte is a conducting organic solution. The lithium/graphite fluoride ( $Li/CF_x$ ) system has attracted much attention in battery technology because it displays high discharge potentials and capacities, resists self-discharge, and is electrochemically stable up to 400 °C [23,64,65]. The  $Li/CF_x$  system has an open-circuit voltage of 3.2 V with an operating voltage of 2.5 to 2.9 V, as well as a theoretical specific energy of about 2180 Wh/kg, which are among the highest voltages and capacities for the solid cathode systems [65]. The discharge potential of a  $Li/CF_x$  system is dependent on the activity of the fluorine ion in the C-F bond, and diffusivity of the supporting electrolyte in the carbon electrode [66]. The discharge capacity is dependent on the amount of fluorine present in the cathode material, either in the form of a C-F bond or an intercalated compound. Galvanostatic studies of the  $Li/CF_x$  system examine the reduction of the  $CF_x$  species, according to the overall reaction [67]:



The half-cell reactions include [65]:



at the cathode, and



at the anode.

The properties and performance of the  $CF_x$  cathode material is dependent on the temperature and mixture of fluorinated gases used to prepare the sample. The fluorination temperature of carbon precursors is loosely divided into three temperature ranges that determine the type of  $CF_x$  that is produced and its fluorine content. High temperature fluorinations are carried out at 500 to 600 °C at elevated pressures using a mixture of elemental fluorine and HF. Carbon monofluorides,  $(C_xF)_n$  ( $0.9 < x < 1.1$ ), are characterized by stage 1 fluorine intercalates [23,68] with covalently-bonded fluorine atoms. Mid-temperature fluorinations of highly crystalline graphite at 350 to 400 °C produce  $(C_2F)_n$  graphite fluorides.  $(C_2F)_n$  are mostly composed of stage 2 to stage 3 fluorine-graphite intercalation compounds [68], F-GICs, with minor stage 4 compounds. GICs are graphitic compounds with ionic or semi-ionic species intercalated between individual layers, giving the material conductivities higher than natural graphite. F-GICs contain semi-ionically bonded fluorine atoms which are still highly conductive, in contrast to insulating  $CF_x$  compounds. Low temperature fluorinations are carried out at room temperature (or less than 100 °C) producing F-GICs,  $C_xF$  [23,68], containing predominantly stage 3 and 4 fluorine intercalated regions. Low temperature fluorination of graphite is carried out in a fluorine atmosphere in the presence of a Lewis acid, usually HF [68], and occasionally in the presence of a metal fluoride catalyst. A volatile metal fluoride, such as,  $WF_6$ ,  $IF_5$ ,  $BF_3$ , and so on [66], catalyzes the fluorine intercalation reaction to produce highly fluorinated  $C_xF$  compounds at low temperatures. The presence of a metal catalyst in the mixture of gases leads to its incorporation into the lattice of the graphitic material, yielding a material with the formula  $CF_xM_y$  ( $0.5 < x < 0.9$  and  $0.02 < y < 0.06$ ) [66]. The use of metal fluoride catalysts was found to have multiple effects on the characteristics of the resultant product. Nakajima et al. [69] for instance, found that the M-F catalysts influence the number of covalent C-F bonds formed, due to the oxidative properties of the Lewis acid on graphite. The overall discharge capacity (and energy density) of the Li/ $CF_x$  battery system was also found to increase, because the

metal fluoride is reduced in the process [70,71]. The discharge mechanism itself, however, was not found to be affected by the presence or reduction of metal fluoride intercalates [65].

Lithium cells containing  $\text{CF}_x$  compounds produced at high temperatures,  $\text{CF}_x(\text{HT})$ , were found to have a working voltage of 2.42 V (vs.  $\text{Li}/\text{Li}^+$ ) and a practical energy density of 1458 Wh/kg. In comparison,  $\text{CF}_x$  produced at room temperature,  $\text{CF}_x(\text{RT})$ , exhibit a working voltage of 3.1 V (vs.  $\text{Li}/\text{Li}^+$ ) and have an energy density of about 2000 Wh/kg [23].  $\text{C}_x\text{F}$  synthesized using  $\text{F}_2$  gas under pressure at room temperature in the presence of high oxidation state complex fluorides,  $\text{K}_2\text{NiF}_6$  or  $\text{KAgF}_4$ , produced material with high discharge potentials of 3.2 V (vs.  $\text{Li}/\text{Li}^+$ ), and with discharge capacities of  $\sim 500$  mAh/g [69]. In general, the discharge potential of a  $\text{Li}/\text{CF}_x$  system is the highest when the fluorination temperature of the highly-fluorinated graphite decreases: while the C-F bond of  $(\text{CF})_n$  formed at high temperatures is entirely covalent in character, ionic C-F bond content increases with a decrease in preparation temperature [66]. As previously stated, the discharge capacity and potential of a  $\text{Li}/\text{CF}_x$  system depends on how easily lithium can diffuse through the graphitic lattice, and the reaction affinity of the C-F bond [66]. The covalent C-F present in  $\text{CF}_x$  indicates a high bond energy and a polar C-F bond, which suggests a lower discharge potential that can be achieved compared with C-F compounds formed at room temperature [68]. Semi-ionic fluoride ions in  $\text{C}_x\text{F}$  have a higher activity than covalently bonded fluorine atoms and display greater ability to diffuse in graphene layers, resulting in higher discharge potentials for  $\text{C}_x\text{F}$  (compared to  $\text{CF}_x$ ) [69]. In general,  $(\text{CF})_n$  would have a higher discharge capacity than  $(\text{CF}_{0.5})_n$  due to a higher fluorine content; however,  $(\text{CF}_{0.5})_n$  has a higher discharge potential because the bonds are more ionic in character than covalent  $(\text{CF})_n$  [66].

### 2.3.2. Deintercalation Process/Mechanism

Galvanostatic experiments used to study the de-intercalation of  $\text{CF}_x$  for the evaluation of the  $\text{Li}/\text{CF}_x$  battery systems are commonly carried out in propylene carbonate (PC) containing a supporting electrolyte, such as a  $\text{LiClO}_4$  or  $n\text{Bu}_4\text{NClO}_4$ . The reduction of  $\text{CF}_x$  is believed to occur through the formation of an intermediate intercalation-type compound ( $\text{M}_x\text{CF}_x$ ), followed by its decomposition and precipitation of an M-F

compound into the carbon material [68]:



And,



\*Li<sup>+</sup> may be replaced with other monovalent cations (such as, nBu<sub>4</sub>N<sup>+</sup> or K<sup>+</sup>)

As previously mentioned, the initial discharge potential is dictated by the most reactive C-F species present in the graphite fluoride, as well as the diffusivity of the cations in the electrolyte. A typical example of a discharge curve is given in Figure 2.11. The discharge potential remains stable (region A) as long as the reducible C-F compound or intercalate is present (and abundant) in the electrode. As the primary species becomes depleted, the potential decreases (region B) to the potential at which the second most reactive species is reduced (region C). In Li/CF<sub>x</sub> systems, experiments are generally stopped when the potential reaches 1.5 V (vs. Li/Li<sup>+</sup>), which corresponds to reduction of the PC electrolyte. The discharge potential is the initial potential at the start of the experiment, and the discharge capacity is measured as the time (or charge) passed, until the potential reaches 1.5 V. The total discharge capacity is dependent on the current density applied to the system, which determines the rate of the reduction reaction.

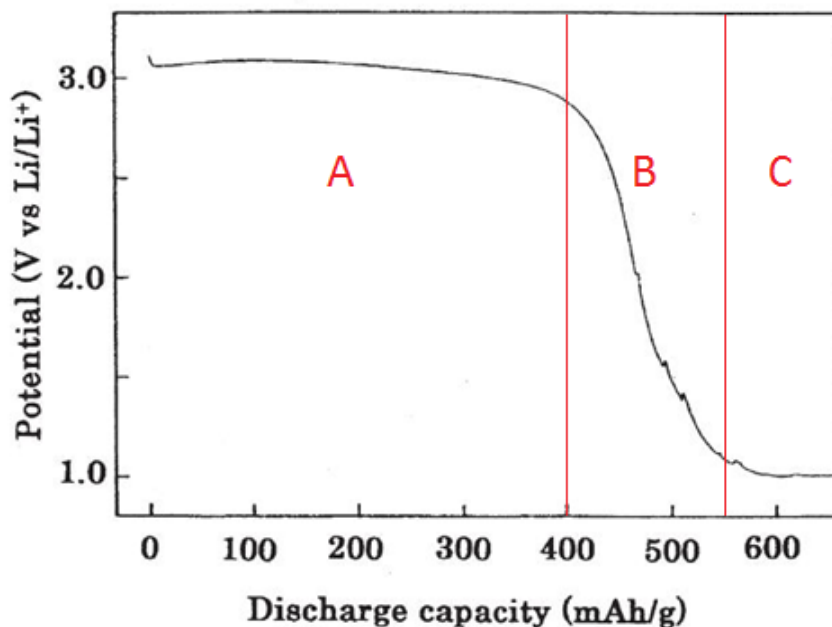
In the mechanism above, discharge of CF<sub>x</sub> proceeds by the insertion of Li<sup>+</sup> into the layers of the graphite fluoride [69]. The lithium ion is oxidized, and the puckered (sp<sup>3</sup>) C-F layers are destroyed by the reduction and discharge of fluorine ions, resulting in the precipitation of LiF into the remaining CF<sub>x</sub> structure [65]. The CF<sub>x</sub> is converted back to pure amorphous (or, graphitic) carbon having sp<sup>2</sup> bonds [69]. Since pure carbon is more conductive than CF<sub>x</sub>, there is an increase in the electrical conductivity of the cathode material, which lowers the cell's internal resistance, which improves the voltage regulation and cell efficiency of the Li/CF<sub>x</sub> system [65]. As the cell is progressively discharged, the reaction interface moves from the surface of the CF<sub>x</sub> into the interior crystallite and the destruction of the puckered C-F layers by discharge enables the migration of lithium ions into the new reaction interface and, thereby, maintaining the

---

<sup>1</sup> nBu<sub>4</sub>N<sup>+</sup> is tetra-n-butyl ammonium ion

continuous discharge of graphite fluoride [69]. The discharge of F-GICs ( $\text{CF}_x$ ), however, is believed to involve the diffusion of lithium ions into the graphitic lattice towards  $\text{F}^-$  ions in the interior crystallites. The diffusion is facilitated by the planar graphene sheets, which are maintained during the fluorination process. The exact structure of the graphite fluoride cathode during and after discharge, the mechanism of the deintercalation process, and the location and form of the expelled  $\text{LiF}$  are largely unknown [65]. In one case, a form of  $\text{CF}_2$  was found to be protected from reduction, which suggested that certain regions may be electrochemically isolated, or the configuration of the C-F bond made it electrochemically inactive [65]. Thus, it would seem that not all of the  $\text{F}^-$  intercalated into the graphite fluoride is electrochemically reversible, and may be a limiting factor in  $\text{Li}/\text{CF}_x$  battery technology.

**Fig. 2.11: Galvanostatic Discharge Curve for  $\text{C}_{1.4}\text{F}$**



Galvanostatic discharge curve for  $\text{C}_{1.4}\text{F}$ , obtained at 40 mA/g in 1 mol/dm<sup>3</sup>  $\text{LiClO}_4\text{-PC}$  at 25 °C. The sample was chemically fluorinated using  $\text{F}_2$  and  $\text{HF}$ , with a  $\text{KAgF}_4$  catalyst. Region A shows discharge potential of the most reducible specie; region B shows depletion of primary reducible species; region C shows reduction potential of secondary species. Used with permission from [70].

The discharge mechanism proposed by Devilliers et al. [67] involving the formation of an intercalation-type compound was put forth following a study comparing the reduction reaction of the  $\text{Li}^+$  cation with the bulkier  $\text{nBu}_4\text{N}^+$  cation in PC. In this particular study, the reduction peak in the  $\text{Li}^+$  system was at a more negative potential compared to the  $\text{nBu}_4\text{N}^+$  system, indicating that the reaction of the  $\text{Li}^+$  occurs more readily than the  $\text{nBu}_4\text{N}^+$  ion. This result is consistent with an effect of the cation size on the overall reaction mechanism [67,71]. The conductivities of the two solutions were similar ( $7.13 \times 10^{-3}$  and  $7.05 \times 10^{-3}$  S/cm for  $\text{LiClO}_4$  and  $\text{nBu}_4\text{NClO}_4$ , respectively), indicating that ohmic drop was not a contributing factor [67,71]. The reaction intermediate is not a true intercalation compound since  $\text{Li}_x\text{CF}_x$  was not detected by XRD, in contrast to other solid electrode systems, such as  $\text{V}_2\text{O}_5$ ,  $\text{Nb}_2\text{O}_5$ , and  $\text{MoO}_2$  [67].

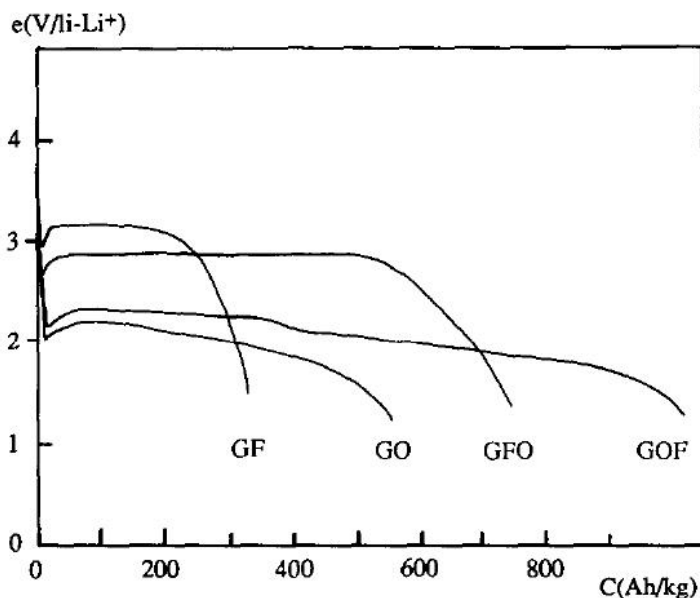
### 2.3.3. Carbon Cathode Materials

Graphite powders are the most common carbon precursor material in  $\text{Li}/\text{CF}_x$  systems due to the effect of fluorine intercalation, which is not possible in amorphous petroleum cokes. Powdered graphite (and carbons), however, have a very high surface area that is not available in HOPG. Amorphous petroleum cokes and carbon fibres have been used to study the effects of surface fluorination and surface structure factors that may affect electrochemical performance [65]. The rate at which different  $\text{CF}_x$  species are reduced and discharged is dependent on the type and structure of carbon involved. For petroleum coke and carbon fibre the covalently bonded fluorine was reduced before the semi-ionic C-F, but in the graphite sample the ionic interactions were reduced first [65]. In a different study, surface fluorination and radiofrequency plasma fluorination were used to effectively increase the surface area of electrodes, increasing the discharge capacity of the cathode material by introducing fluorinated mesopores into the surface [72]. The discharge capacity was also found to be dependent on the quantity of co-intercalated  $\text{HF}$  and  $\text{HF}_2^-$  [70].  $\text{C}_x\text{F}$  samples with lower quantities of these co-intercalated species had relatively stable discharge potentials and large discharge capacities [70]. In particular,  $\text{HF}_2^-$  was found to co-exist with  $\text{F}^-$  in stage 2 phases of F-GICs (and to a certain extent, stage 1 F-GICs). This may be explained by the fact that the stage 2 and higher  $\text{C}_x\text{F}$  compounds have nearly ionic C-F bonds [70], so co-intercalated

$\text{HF}_2^-$  ions can persist, as indicated by their IR spectra.

Other graphite compounds have been tested for their electrochemical properties, including graphite oxide (GO) and graphite oxyfluoride (GOF and GFO) compounds (Fig. 2.12). Li/GO compounds have a theoretical energy density of 3000 Wh/kg based on an open-cell voltage of 3.0 V; however, GO compounds were found to have a lower discharge potential compared to GF (which has both semi-ionic and covalently bonded F). The practical faradaic capacity of GO was only 50 to 60% of the theoretical densities. In comparison, both graphite oxyfluorides, GOF and GFO, displayed higher energy capacities due to the higher degree of saturation compared to GF or GO compounds in which the C=C bonds are not fully oxidized [23].

**Fig. 2.12: Galvanostatic Discharge Curves for Various Graphite Fluorides and Oxyfluorides**



Galvanostatic discharge curve for graphite fluoride (GF,  $\text{C}_4\text{F}_{1.48}\text{H}_{0.44}$ ), graphite oxide (GO,  $\text{C}_4\text{O}_{1.89}\text{H}_{1.04}$ ), and graphite oxyfluoride (GFO and GOF,  $\text{C}_4\text{F}_{1.44}\text{O}_{0.60}\text{H}_{0.44}$  and  $\text{C}_4\text{O}_{1.48}\text{F}_{1.32}\text{H}_{0.56}$ , respectively) samples obtained at a current density of  $0.025 \text{ mA/cm}^2$  in 1 M  $\text{LiClO}_4\text{-PC}$  at  $25^\circ\text{C}$ . Used with permission from [23].

## 3. Theory

### 3.1 Raman Spectroscopy

Raman spectroscopy (RS) is a vibrational spectroscopy method that qualitatively measures the intensity of vibrational modes of particular bonds based on the inelastic scattering effect of incident photons on atoms in the material. During the scattering process, the electron cloud around the atom becomes polarized, and the change in energy of the scattered photon provides information on the types of bonds present. A depth resolution of 1 – 5  $\mu\text{m}$  is achievable with Raman spectroscopy. RS can be used to detect a change in the localized bonding of a material caused by the addition of a foreign species into the lattice. In the  $\text{CF}_x\text{-Li}$  battery field, it is used to study the effect of fluorine intercalation on the bonding structure of carbon atoms in highly crystalline graphite [52]. There are two primary vibrational modes observed in the Raman spectrum of graphite, the  $E_{2g}$  (the “G-band”) and D, which corresponds to the trigonal C-C bonds in the uniform hexagonal lattice of planar graphene layer (the “ordered” carbons), and the C-C bonds at the edges of graphene layers (the “disordered” carbons), respectively [52]. These two characteristic vibrational modes are observed in the region of  $1580\text{ cm}^{-1}$  and  $1350\text{ cm}^{-1}$ , respectively. Another commonly observed peak at  $\sim 2700\text{ cm}^{-1}$  is an overtone of the “disordered” peak (at  $\sim 1350\text{ cm}^{-1}$ ). This overtone peak may exist whether or not a “disordered” peak is present. The overtone peak is attributed to the polarization of electrons to an excited energy level, above that which is considered the “normal” excited state. Since the intensity of this peak is closely related to the current energy state of the atoms within the material when the experiment is run, its intensity is not predictable. Thus, it is not used for the examination of fluorine intercalation for this reason. An example of a Raman spectrum of polycrystalline graphite is provided in Figure 3.1.

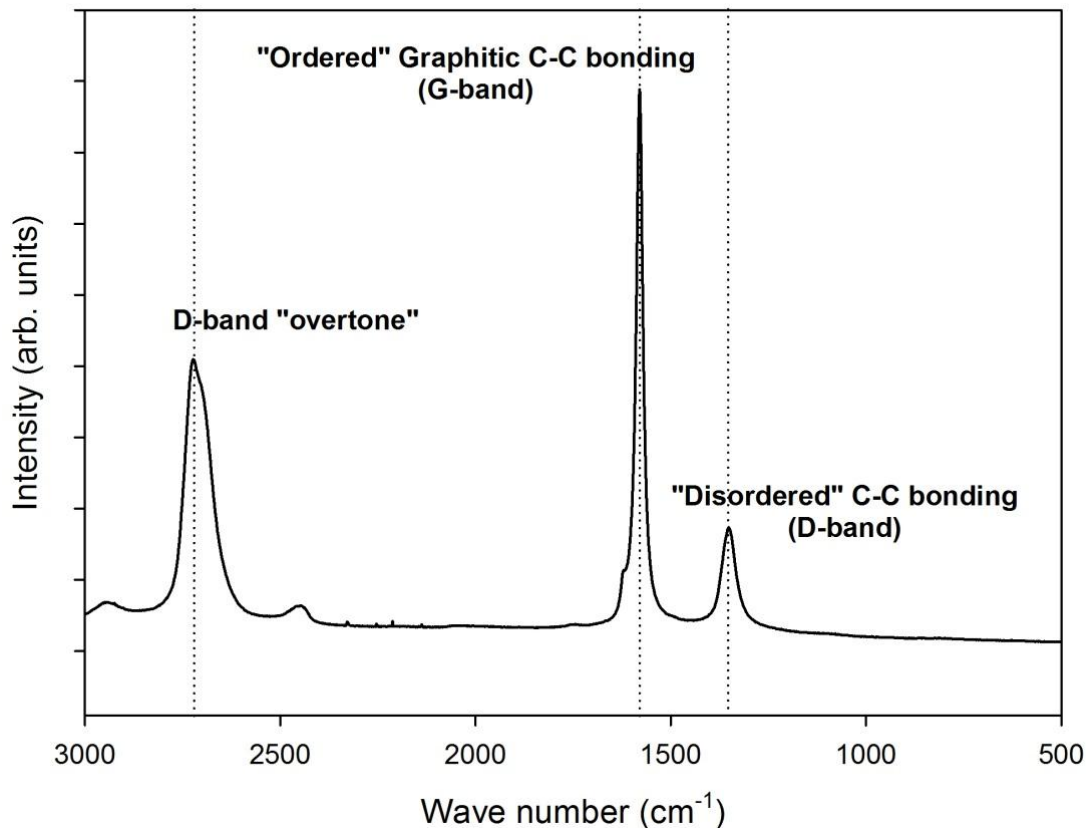
### 3.2 EIS

#### 3.2.1. Electrochemical Impedance Spectroscopy Theory and Model

Electrochemical Impedance Spectroscopy (EIS) is a technique that uses a sinusoidal alternating potential signal to study the electrical properties of a solid/solution interface.

The electrical double-layer and surface properties (such as, passive films, uniformity,

**Figure 3.1: Raman spectrum of graphite**



Typical Raman spectrum of polycrystalline graphite with characteristic vibrational peak positions

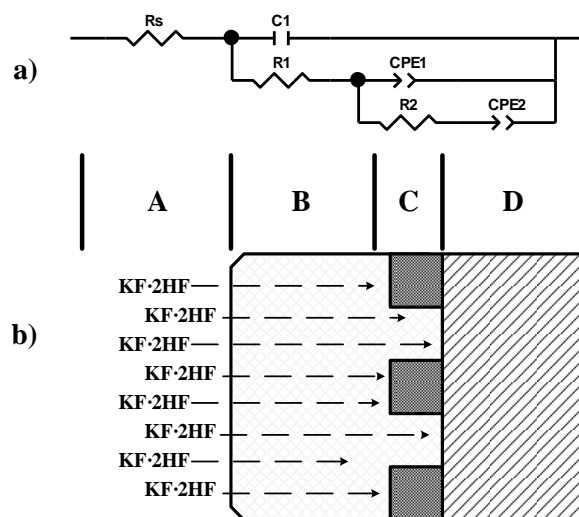
porosity, etc.) of the electrode give rise to the capacitive or resistive properties observed when the AC signal is applied. The interface can be modelled as an electric circuit to explain the surface chemistry occurring as a constant (DC bias) potential and AC signal are applied. This is especially important when very specific properties of the C/KF·2HF interface need to be studied, such as development of the passivating layer, or the perturbation of the electrical double-layer by an applied potential. This can be used to assess the solution resistance on a particular electrode, since ohmic (solution) resistance has a significant effect on the kinetics of the industrial fluorine system.

### 3.2.2. Description of Circuit Diagram

Using the electrical response to a potential perturbation, the interface can be modeled as

an electric circuit to explain the chemical and physical processes at the surface of an electrode. The circuit model that corresponds to the interface is represented by components such as resistors and capacitors, due to the electric properties of the physical and chemical phases present near the electrode surface. While the resistances yield information regarding the kinetics of the reaction, capacitance values provide mechanistic data about the reaction. The thickness of the double-layer capacitor is a measure of the difficulty in separating opposing charges through the material to prevent discharge. Whereas high frequencies are useful in studying the resistive layer on the surface, lower frequencies are useful for studying the slower chemical processes. The complexity of the carbon/KF·2HF molten salt interface stems from the constantly changing chemistry in the region surrounding the surface, C-F bond formation, as well as the effects caused by surface roughness and microstructure of the carbon electrode. Existing circuit models have represented the interface as being composed of strictly resistive and capacitive components, assuming that the electrode surface is uniform [44,45]. A novel representation of the C/KF·2HF interface following polarization and passivation as an electrical circuit is shown in Figure 3.2. Region A represents the bulk KF·2HF electrolyte and is represented by a solution resistance ( $R_s$ ). The  $R_s$  is dependent on the conductivity (and composition) of the electrolyte, and can change with concentration or temperature of the bulk solution. Region B represents the electrochemical double-layer present at the surface (represented by a capacitive component,  $C_1$ ), and the resistance of that interface layer ( $R_1$ ). Region C represents the physical surface of the electrode which is made up of a  $CF_x$  passive film, regions of non-passivated carbon, and takes into consideration surface roughness. Region C is represented by a constant-phase element (CPE1) and a resistor ( $R_2$ ). A CPE is used for a time-constant distribution, when a single component (i.e., capacitor, resistor, or inductor) cannot accurately show the ideal response expected for single electrochemical reactions. Rather, it reflects a distribution of reactivity rather than a uniform one. This is particularly important on an electrode with high surface roughness or when the surface is partially passivated. Region D represents the microstructure of the carbon electrode. Composed of a constant-phase element (CPE2), this component takes into consideration the graphitic or amorphous microstructure, the diffusion of intercalated ions ( $F^-$  or  $HF_2^-$ , in particular), and porosity.

**Fig. 3.2: Circuit Model and Representation of C/KF·2HF Interface for Non-Uniform Microstructure**



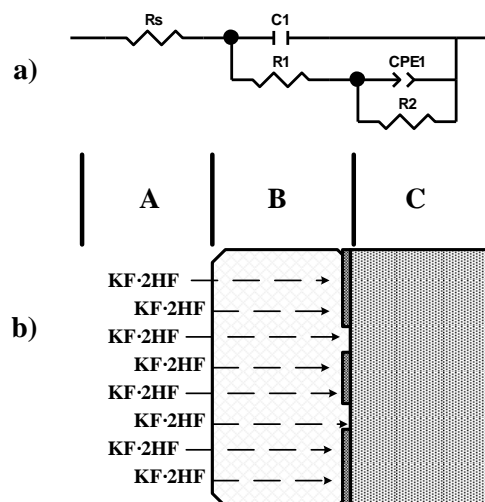
a) Equivalent circuit model of C/KF·2HF interface, and b) schematic of system having regions corresponding to the electrode surface containing a passivated  $CF_x$  layer, with non-uniform microstructure, such as graphite crystallinity or porosity. Region A: resistance of electrolyte solution; region B: Helmholtz layer/electrochemical double-layer; region C: electrode surface comprising surface roughness and  $CF_x$  layer; and region D: diffusion of intercalated ions through lattice and/or porosity.

A vitreous carbon/KF·2HF system may be better represented by Figure 3.3, since vitreous carbon is non-porous, lacks crystallinity, and therefore, cannot be easily intercalated by fluorine ions.

### 3.2.3. Simplifying a Circuit Diagram

The circuit diagram for a solid/solution interface can be simplified if the double-layer region is the primary focus. The high frequency range is the most useful for the examination of the solution double-layer, because the low frequency range is dominated by the resistance and capacitive properties of the electrode material itself. Thus, fitting of the high frequency data to a simple model can be achieved without an appreciable effect on the capacitance or resistance values of a more intricate model of the entire system. Table 3.1 shows the difference in the fitted capacitance and resistance values ( $C_1$  and  $R_1$ ) of the solution double-layer for a graphite rod using a simple model ( $10^5 - 10^4$  Hz range) and that of a complex model ( $10^5 - 10^0$  Hz range). It should be noted that the  $C_1$  capacitance values for the two different models are similar even for different circuit

**Fig. 3.3: Circuit Model and Representation of C/KF·2HF Interface for Uniform Microstructure**



a) Equivalent circuit model of C/KF·2HF interface, and b) schematic of system having regions corresponding to the electrode surface containing a passivated  $CF_x$  layer, with uniform microstructure. Region A: resistance of electrolyte solution; region B: Helmholtz layer/electrochemical double-layer; region C: physical surface comprising  $CF_x$  layer.

**Table 3.1: Fitted Values for Simple and Complex Circuit Models of Graphite**

	Simple	Complex
Model		
Frequency Range of Fitted Data	$10^5 - 10^4$	$10^5 - 10^0$
Solution Resistance (Rs)	3.13	3.19
D-L Capacitance (C1)	<b><math>1.33 \times 10^{-5}</math></b>	<b><math>1.22 \times 10^{-5}</math></b>
D-L Resistance (R1)	<b>1.6</b>	<b>1.0</b>
CPE1-T		$3.25 \times 10^{-4}$
CPE1-P		0.713
R2		1730
$\chi^2$	0.0017	0.0018

Fitted values for different circuit models (at different frequency ranges) of a graphite rod polarized potentiostatically at 4.0 V for 40 minutes. Values in table show that a circuit model can be simplified without a large impact on double-layer (D-L) capacitance and resistance values of the high frequency range of data. The double-layer capacitance and resistance values are bolded.

diagrams fitted over different frequency ranges. The R1 value was noticeably different, and was accompanied by a larger degree of error in the calculated value. A more detailed fitting scheme would be required to bring the resistances to a similar value. However, a simplified circuit model can be used to represent the double-layer region of the C/KF·2HF interface, and may be a reasonable approximation of the entire system.

### 3.2.4. Calculation of Double-Layer Thickness

The thickness of the solution double-layer, represented as a parallel-plate capacitor, can be estimated based on the equation [13]:

$$C = \epsilon_r \epsilon_o \frac{S}{d} \quad (17)$$

Where C is the capacitance,  $\epsilon_r$  is the dielectric constant of the material,  $\epsilon_o$  is the electric permittivity constant, S is the surface area, and d is the thickness of the double-layer. The value of capacitance can be obtained as C1 from the simplified fit to the circuit.

### 3.3. Galvanostatic Discharge Studies

Galvanostatic discharge experiments are normally used to measure the discharge capacity and potential for chemically fluorinated graphite for use in Li/CF<sub>x</sub> batteries. In order to obtain the necessary discharge capacities (fluorine content) for battery systems, the graphite fluoride, CF<sub>x</sub>, material is produced by the chemical fluorination of graphite powders. This technique has not been applied for the evaluation of electrochemically intercalated fluorine in graphite, possibly due to the lower concentration of fluorine atoms that can be inserted into the material. The discharge characteristics would be used to compare electrochemically- and chemically-fluorinated carbon materials.

As it was previously stated, two critical measurements that are used to compare these intercalated samples are the discharge potential and discharge capacity. The discharge potential represents the stable output voltage generated from a stable reduction reaction occurring at an electrode surface during the application of a steady-state current. The discharge capacity relates to the amount of reducible species available, in this case, intercalated or surface fluorine ions that can be extracted from the material. By

examining these two values, one can draw comparisons about the strength (or, type) of the C-F bonds present in the material (i.e., ionic or covalent), as well as the quantity of fluorine that was intercalated into the material.

## 4. Experimental

### 4.1. Materials, Supplies, Chemicals

#### 4.1.1. Carbon Anode Materials

The type of carbon anode material and their supplier are given in Table 4.1, and were used as received:

**Table 4.1: Selected Carbon Anode Materials and the Commercial Source**

Carbon Type	Shape	Source
Carbon (graphitized)	Rod	NAC Carbon Products, Inc.
Graphite	Rod	NAC Carbon Products, Inc.
Highly Oriented Pyrolytic Graphite (ZYH Grade)	Plate	Momentive Performance Materials, Inc.
Vitreous Carbon (Glas 22 Grade)	Plate	SPI Supplies
Amorphous Carbon	Block	Toyo Tanso Japan
Amorphous Carbon	Block	Cameco
Graphite Fluoride, CF <sub>x</sub> (62 - 64 wt.% F, stage 1 CF <sub>x</sub> )	Powder	Central Glass Company, Japan
Coal-Tar Pitch	Rod	NAC Carbon Products, Inc.

Vulcan-PTFE and graphite-PTFE carbon anode materials synthesized by Santhanam [73] in the lab by a Sol-Gel method (Appendix 2) are given in Table 4.2:

**Table 4.2: Carbon-PTFE Electrode Samples**

Carbon Type	Source
Vulcan Carbon (20% PTFE)	Dr. R. Santhanam
Vulcan Carbon (35% PTFE)	Dr. R. Santhanam
Graphite (20% PTFE)	Dr. R. Santhanam
Graphite (35% PTFE)	Dr. R. Santhanam

#### 4.1.2. Chemicals and Materials

Solid KF·2HF electrolyte from Cameco RC was used for the fluorination experiments, in the as received condition. There was no active control on the storage conditions of the electrolyte, and the laboratory was not configured for the regeneration of fresh electrolyte. As a result, the electrolyte was stored in the walk-in fume hood for safety precautions. Aqueous HF (50%, Sigma-Aldrich Co.) was used to prepare the CuF<sub>2</sub>

reference electrode from standard 18 gauge household wire. The Ag/AgI reference electrode was constructed out of an Ag wire purchased from CH Instruments. Reagent grade KI (99.99+% metals basis, Sigma-Aldrich Co.) was used and dissolved in demineralized water to ensure that the AgI layer coated on the Ag wire would be of high purity. Finally, a high grade of NaI (ACS reagent,  $\geq 99.5\%$ , Sigma-Aldrich Co.) was purchased for use as the filling solution of the reference electrode. The high purity was necessary because the filling solution must be as free of contaminants as possible, otherwise the equilibrium potential could change and reduce the accuracy of galvanostatic experiments.

The specifications of the chemicals were selected on the basis that a high purity will minimize the effects of contaminants on the measurements, if the contaminants cannot be controlled, such as moisture. Propylene carbonate (PC) (anhydrous, 99.7%, Sigma-Aldrich Co.) is a commonly used electrolyte media for fluorine discharge experiments and so it was selected. Lithium perchlorate,  $\text{LiClO}_4$  (anhydrous, 99%, Alfa Aesar), is a commonly used supporting electrolyte for PC in this type of experiment, and is known to have poor solubility in PC if the perchlorate ion becomes hydrated. Thus, pure grades of  $\text{LiClO}_4$  and anhydrous PC were selected to minimize the experimental complications of low conductivity or high concentration of impurity in the electrolyte. 4 Å molecular sieve (1-2 mm diameter, Alfa Aesar) was selected to minimize the moisture in the PC, since the stock solution would be used slowly over the course of experiments.

Virgin grade polytetrafluoroethylene (PTFE) (Professional Plastics) was selected as the stock material for the cell components. This would avoid concerns of contamination of the molten salt by impurities present in the PTFE, particularly in the case of the gas shrouds, which would be in direct contact with the electrolyte. Fluorinated ethylene propylene (FEP) (Fisher Scientific) tubing was selected in place of PTFE tubing, because it has comparable chemical resistance to a HF-rich environment, but is transparent and more flexible than PTFE. A polymethylpentene (PMP) (Nalgene) beaker was selected as the body of the electrochemical cell for its chemical resistance to the HF media, and for the (relatively) higher melting point, since the cell required a constant use temperature of greater than 100 °C for safety reasons, if the heater operated out of the designed specifications.

## 4.2. Experimental Apparatus

To carry out the electrochemical experiments laid out in this work, a specialized heater and electrochemical cell was required. A heater had to be constructed based on specific experimental requirements such as the ability to maintain the electrochemical cell at an operating temperature of approximately 90 °C. Next, an electrochemical cell was required that could operate at elevated temperatures, as well as resist the extremely corrosive effects of HF and evolved F<sub>2</sub> gas. This section outlines the design features and construction of the experimental apparatus to meet the goal of the ability to carry out electrochemical fluorination experiments for (relatively) long periods.

### 4.2.1. Cell Heater Design Features and Construction

The cell electrolyte heater was designed and constructed with the goal of melting the KF·2HF electrolyte and maintaining a constant cell temperature between 85 – 100 °C for the duration of the experiments. Design requirements were: the ability to safely maintain the operating temperature of the cell; a simple, modular design that could accommodate electrochemical cells of different shapes and sizes; simple construction, allowing components to be easily replaced; and the ability to see into the heater compartment and cell during experiments.

The heater designed was a simple convection heater composed of a fan, air heater, and cell enclosure. The filter fan (#FF01801800001) and tubular air heater (#AHF-06120) were purchased from Omega Engineering, Inc., the steel cell enclosure was purchased from Electro Sonic, Inc. The adaptors and connection between each component were machined by Torode Precision Components, Inc. The heater was controlled by a 1/16 DIN temperature controller (#CN742) via a K-type thermocouple (#BLMI-INC-K-116U-12) which extended into the electrochemical cell for active monitoring. The temperature controller was reported to be accurate within  $\pm 0.25\%$  span,  $\pm 1$  of the least significant digit. The temperature controller and thermocouple were calibrated against a digital thermometer (#TPD33 from Omega Engineering, Inc.) that was accurate within  $\pm 1$  °C. The over-temperature safety system was a thermal fuse (#317-1136-ND) manufactured by Cantherm. The fully assembled electrolyte heater is shown in Figure 4.1.

**Fig. 4.1: Image of Assembled Cell Electrolyte Heater**

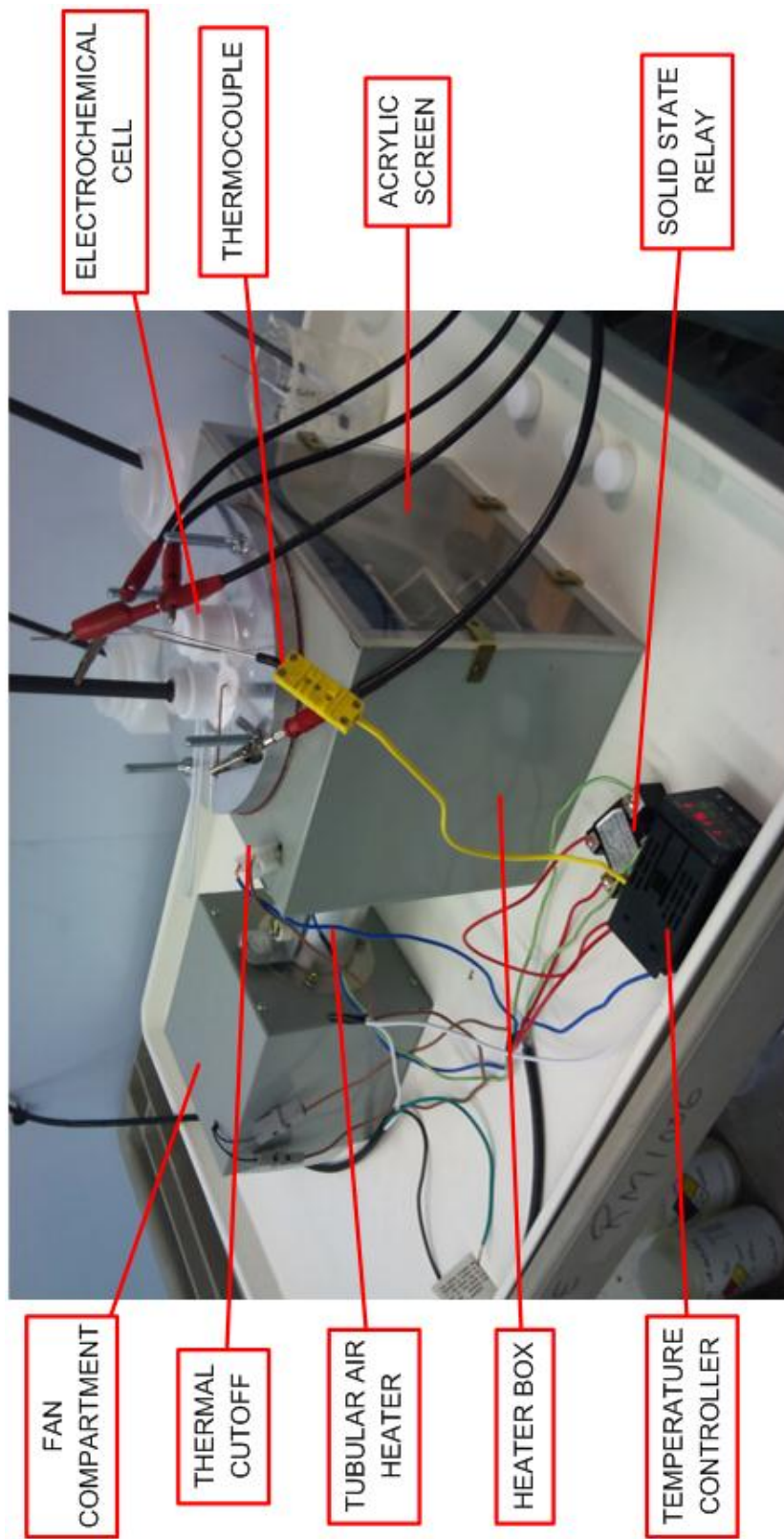
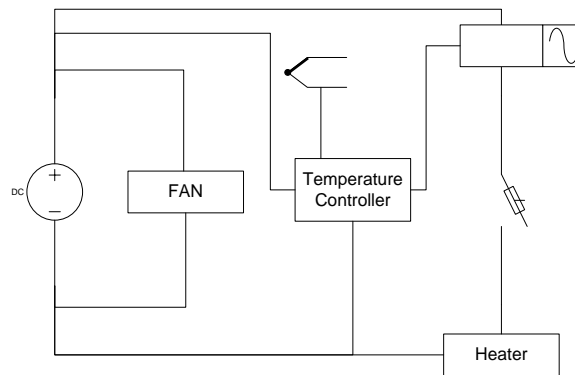


Image of fully assembled cell electrolyte heater in operation

The filter fan takes in air at ambient temperature and pushes it through the tubular air heater. The heated air then enters the cell enclosure compartment and heats the electrolyte in the cell. The fan and heater are electrically connected in parallel so that a constant flow of air through the heater would be maintained between heating cycles of the air heater. If the heater fails during normal operation, the fan could quickly cool the heater, causing the electrolyte to freeze and render the system safe. If the fan fails during operation the heater will continue to run, however, the thermal fuse will open the circuit and the heater will cut-out well below the rated melting temperature of the PMP electrochemical cell. The front side of the cell compartment is closed with a 5 mm-thick acrylic window, providing adequate insulation for the heated air while allowing clear visibility into the cell enclosure and electrochemical cell during operation. The circuit diagram of the cell electrolyte heater along with temperature controller is shown in Figure 4.2.

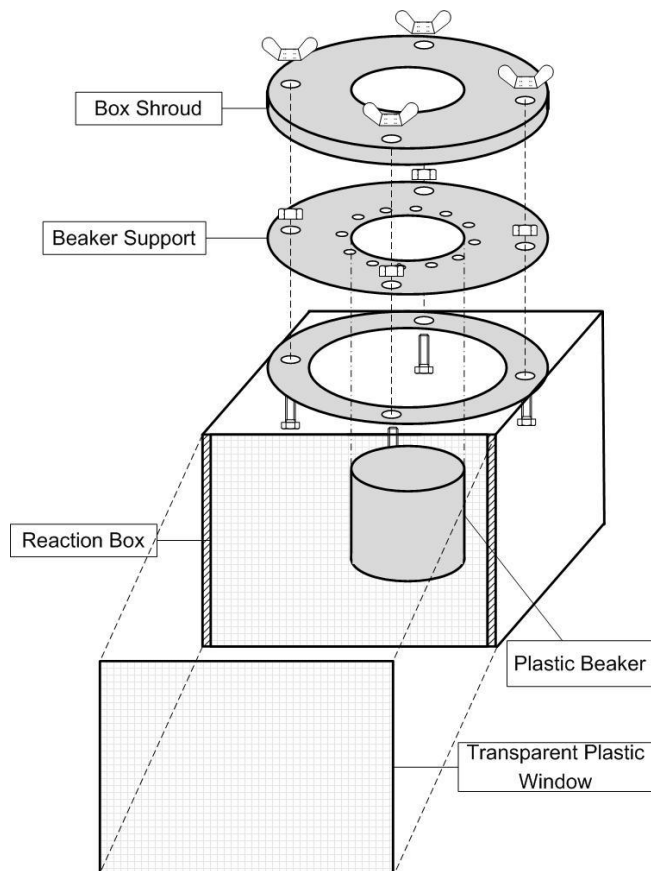
**Fig. 4.2: Circuit Diagram of Cell Electrolyte Heater**



Circuit diagram of cell electrolyte heater showing the fan, temperature controller, relay, heater, and thermocouple components.

The cell compartment (Fig. 4.3) has design features to promote uniform heating of the cell electrolyte and allow cell components to be easily changed during heater operation. The hot air enters from the centre of the cell enclosure, but is directed below the PMP cell. This prevents a local heating hot-spot on the beaker, which may lead to thermal fatigue of the beaker from the non-uniform heating that could occur. The electrochemical cell was inserted through the top of the compartment and held in place by a silicone sheet

**Fig. 4.3: Schematic of Heater Compartment for Cell Electrolyte**



Heater cell enclosure showing exploded view of box shroud, beaker support plate, and viewing screen

and a venting plate (Fig. 4.3). The silicone sheet was cut to size to hold the beaker in place, while the venting plate directed the hot air out of the box. The hot air shroud had a dual purpose of directing the hot exhaust air over the top of the cell to improve heating, as well as containing the cell lid if the cell became pressurized. The cell heater components were fastened with nuts and bolts, so that the hot air shroud could be easily removed if the cell needed to be adjusted or heater components needed to be replaced. The large circular opening at the top of the hot air shroud makes it possible to insert and exchange electrodes, gas purge hoses, and the thermocouple through the cell lid and into the cell compartment without having to disassemble the unit. As well, the electrical leads from the instrumentation are easily connected to the electrodes from the top of the compartment. A list of parts for the cell electrolyte heater is provided in Table 4.3.

**Table 4.3: Parts List for Cell Electrolyte Heater**

<b>Component</b>	<b>Source</b>	<b>Part Number</b>
Filter fan	Omega Engineering, Inc.	#FF01801800001
Tube heater	Omega Engineering, Inc.	#AHF-06120
Temperature controller	Omega Engineering, Inc.	#CN742
K-Type thermocouple	Omega Engineering, Inc.	#BLMI-INC-K-116U-12
5 mm acrylic screen	N/A	N/A
Thermal fuse	Cantherm	#317-1136-ND

#### 4.2.2. Electrochemical Cell Design Features and Construction

The purpose of the electrochemical cell is to safely contain the highly corrosive KF·2HF electrolyte at operational temperatures (~90 °C) for the duration of the experiments. Design parameters include: the isolation and venting of H<sub>2</sub> and F<sub>2</sub> gases; the ability to easily switch electrodes between experiments; and optical clarity to allow the cell contents and electrodes to be monitored.

The cell container was a 250 mL PMP beaker produced by Nalgene. It was selected for its chemical resistance to the electrolyte, relatively high heat resistance, and transparency. It is rated for a continuous use temperature of 150 °C, and an intermittent service temperature of 175 °C. The remaining cell components include the cell lid, gas shrouds, plugs, and electrode holders, which were all made of polytetrafluoroethylene (PTFE) because it is chemically inert in the electrolyte. An image for the fully assembled cell is shown in Figure 4.4. The cell lid was machined from a 8.89 cm diameter PTFE rod that was cut 0.953 cm thick. The lid was faced to yield a smooth surface, and six holes were drilled for the different cell components labelled in Figure 4.5. Two of the holes (2.54 cm diameter) are for gas shrouds and their respective electrodes, one hole (1.27 cm diameter) is for the Cu/CuF<sub>2</sub> reference electrode (+0.4 V vs. SHE) [45], one hole (0.953 cm diameter) is for the thermocouple, and the remaining two holes are for inert gas purge lines. The cell lid was affixed to the cell body using silicone caulking to prevent the egress of HF fumes (i.e., ensuring a good seal), and is a simple method for closing the spout on the PMP beaker. The gas shrouds were designed so that the working or counter electrode can extend through the shroud cap down into the cell, and any H<sub>2</sub> or F<sub>2</sub> gas evolved traveled up the shroud and out through a hole near the cap to vent the gases

**Fig. 4.4: Image of Fully Assembled Electrochemical Cell**

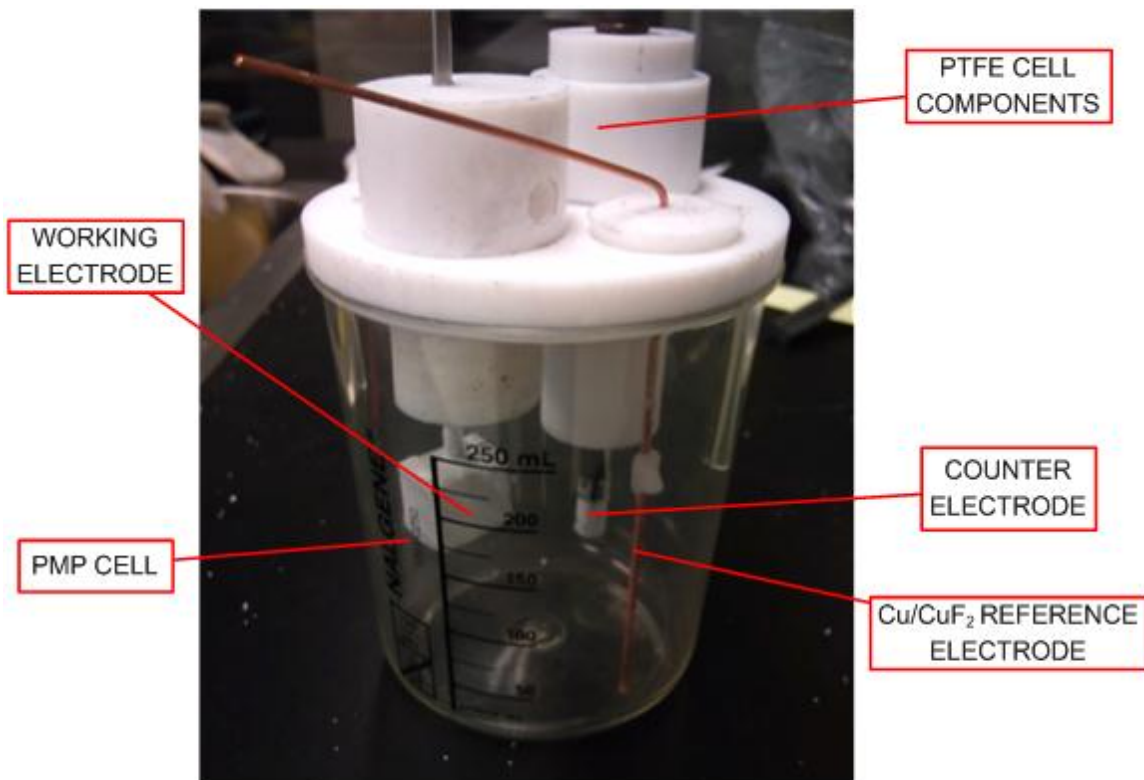
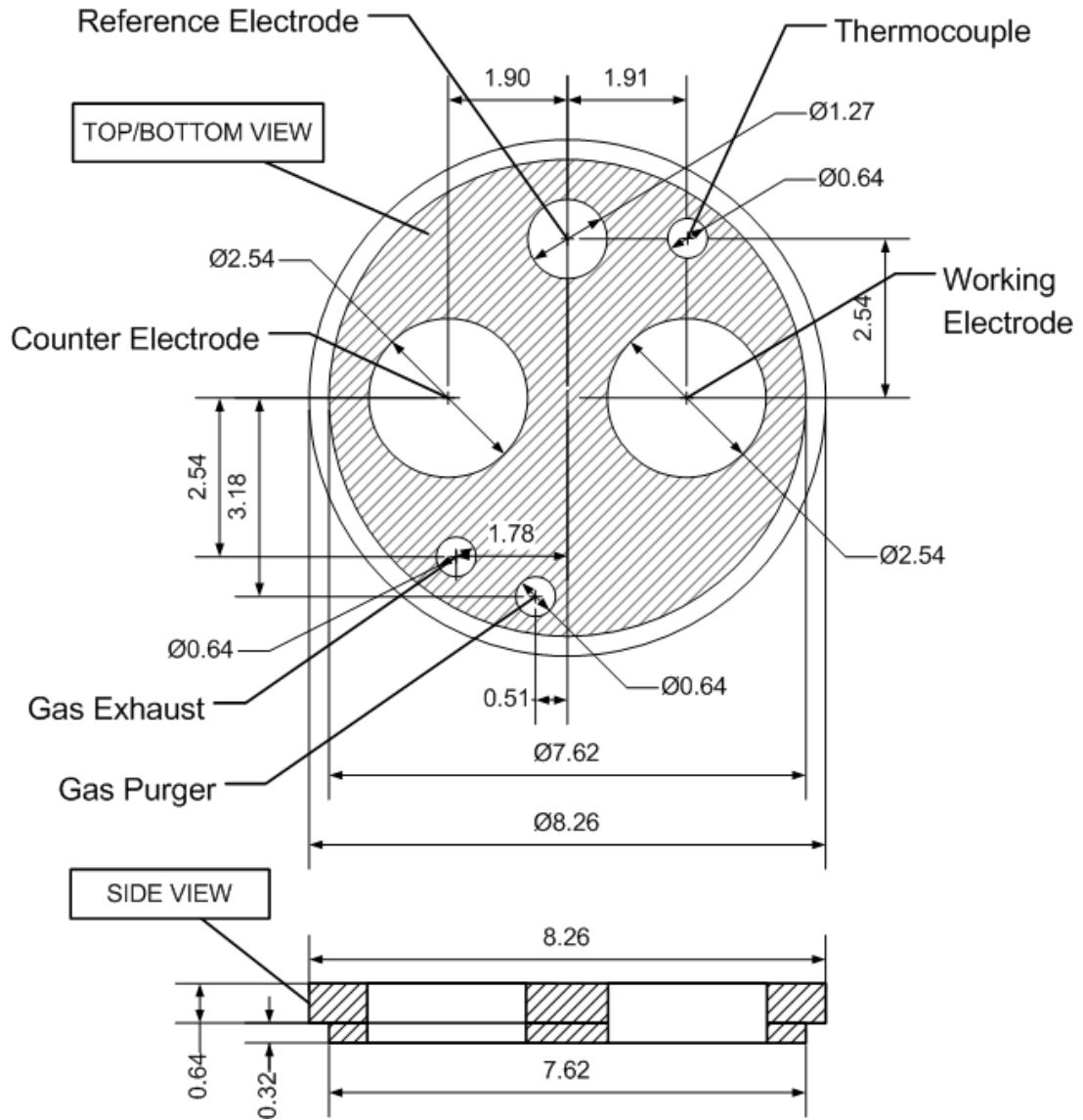


Image of fully assembled electrochemical cell for fluorine generation (KF·2HF electrolyte not shown)

(Fig. 4.6). The gas shrouds were machined from 3.175 cm diameter PTFE rods to a length of 6.985 cm. The upper section was 3.175 cm, while the shaft was machined down to 2.54 cm in diameter. This would allow the gas shroud to be inserted into the cell lid and hold any electrode in stable, vertical position. The upper section of the gas shroud would prevent the material from falling into the cell if thermal creep occurs in the cell lid. Any overpressure from the build-up of evolved gases could cause the lid to pop off. The evolved gases were separated because the recombination of H<sub>2</sub> and F<sub>2</sub> could cause an explosive reaction. Also, 6.35 mm diameter fluorinated ethylene propylene (FEP) tubing connected to the gas shrouds directed the vented gases away from the cell and each other, out into the fume hood. For the small quantities of gas generated, the fumehood provided adequate dilution and the scrubber provides adequate removal of F<sub>2</sub> gas prior to release.

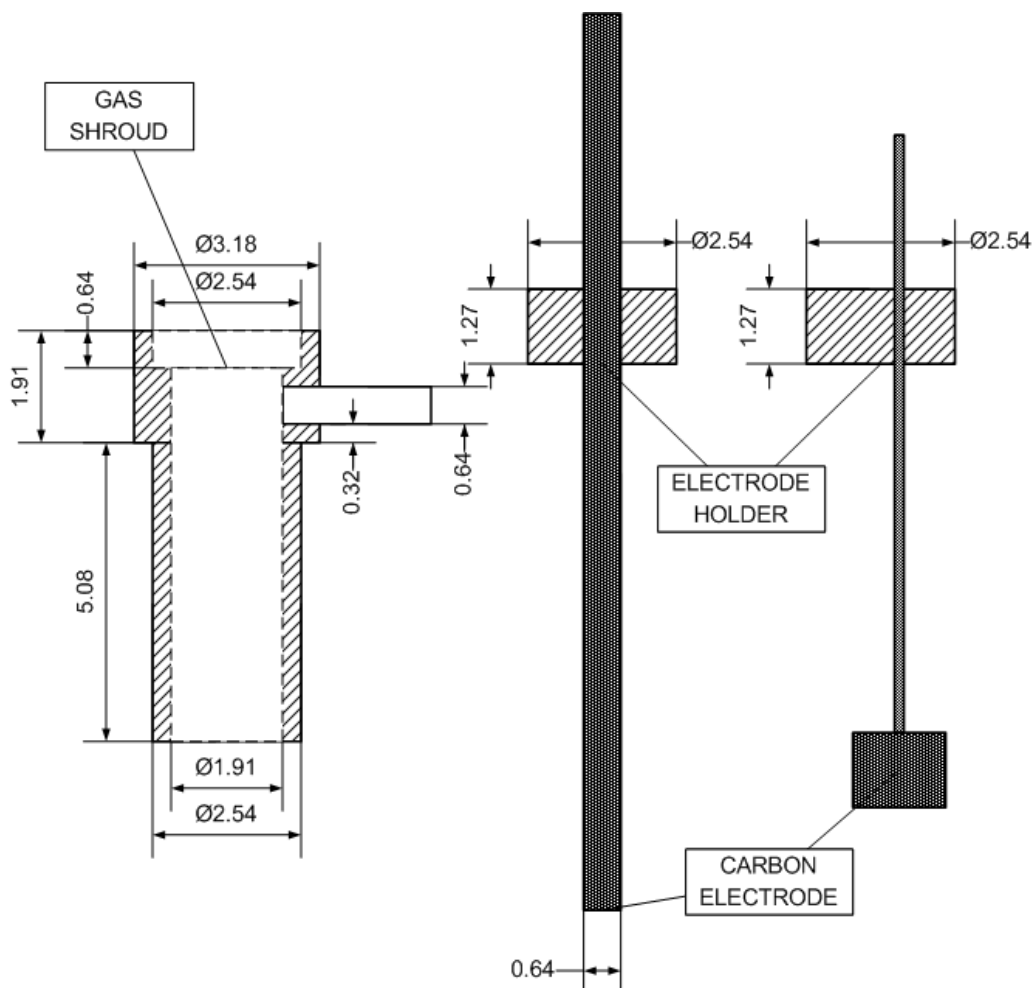
**Fig. 4.5: PTFE Cell Lid**



Schematic of designed and machined PTFE cell lid, showing the positions for the  $\text{F}_2$  and  $\text{H}_2$  gas shrouds. The electrodes were positioned in the centre of the gas shrouds. The ports for the gas purge lines and thermocouple are shown. All dimensions provided are in centimetres.

Simple PTFE plugs/blanks were used as caps for the gas shrouds when electrodes were not inserted into the cell, particularly when the electrolyte was melting, or freezing. PTFE thermocouple and reference electrode holders were used to position these components in the cell, and allow these two components to be easily manipulated. It should be noted that the Cu/CuF<sub>2</sub> electrode was not separated from the cell electrolyte through a membrane, but rather inserted directly into the cell. The K-type thermocouple was wrapped with Teflon-tape to protect the Inconel sheath from corrosion in the KF·2HF electrolyte. Finally, the holes for inert gas purge lines were sized to fit 0.635 cm diameter FEP tubing, where they could be inserted directly into the electrochemical cell.

**Fig. 4.6: PTFE Gas Shroud and Electrode Holders**



Schematic of PTFE gas shroud and electrode holders for rod and block electrodes. All dimensions given are in centimetres.

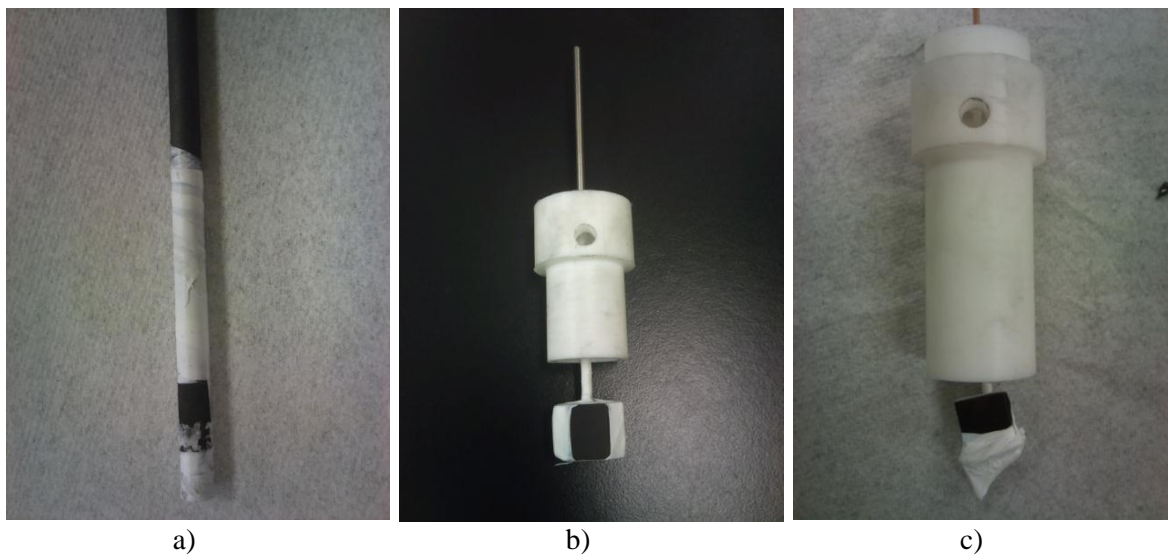
The carbon electrode materials were purchased as rods, blocks, or plates (Table 4.1). Rod electrodes were used with a PTFE holder, which was a PTFE plug with a centered 0.635 cm hole for the electrode to be extended into the cell (Fig. 4.6). The rods were held in place by a friction fit, and a Viton O-ring maintained the vertical position of the rod to allow for any expansion by PTFE thermal creep. The vertically exposed surface area was controlled with heat-shrink PTFE tubing or with Teflon-tape. The exposed geometric surface areas of the carbon electrodes were accurate to  $0.01 \pm 0.001 \text{ cm}^2$ . Amorphous carbon electrode material was acquired in a block form and was cut to roughly 1.5 cm x 1.5 cm x 2 cm in size. These carbons were drilled and tapped, and a threaded, plated-steel rod was screwed into the carbon (Fig. 4.6) to establish a direct electrical contact without the use of conductive paste. The electroactive surface area was controlled by partially wrapping the carbon with Teflon-tape to expose only the desired surface area. The section of metal rod within the cell was protected from the HF fumes using Teflon tape. The section of rod outside of the cell was left exposed for connecting the electrical leads to the potentiostat. For vitreous carbon, the plate was scored using a diamond-tipped glass cutter, and then broken. A copper wire was flattened and pressed directly against the carbon surface before being wrapped with Teflon tape. The electroactive surface area of the carbon electrode was also controlled with preferential wrapping using the tape. The section of copper wire within the cell connecting the carbon electrode to the electrical leads was wrapped to prevent the formation of  $\text{CuF}_2$ , which may affect electrochemical measurements. As with the metal rod, the section outside of the cell was left unwrapped for connection to the leads to the potentiostat. All electrodes were positioned vertically to promote bubble detachment. Images of each type of electrode are shown in Figure 4.7.

### **4.2.3. Instrumentation**

#### ***4.2.3.1. Electrochemical Hardware***

All electrochemical experiments were conducted using a Solartron SI 1286 Electrochemical Interface controlled by a PC running Windows XP (3.0 GHz Core 2 Duo, 4 GB DDR3 RAM). A Solartron 1255 HF Frequency Response Analyzer was used

**Fig. 4.7: Images of Rod, Block, and Plate Electrodes**



Images of carbon electrode samples a) graphite rod electrode, b) amorphous carbon block electrodes, and c) plate electrode

to conduct AC Impedance measurements. Experimental results were transferred off the computer using a standard USB key.

#### ***4.2.3.2. Software***

Electrochemical polarization experiments were conducted using CorrWare® 3.2a and analyzed using CorrView® 3.2a. AC impedance experiments were conducted using ZPlot® 3.2a, and analyzed using ZView® 3.2a. All of the software for electrochemical experiments was produced by Scribner Associates, Inc.

#### ***4.2.3.3. Raman Spectroscopy***

Raman spectra were acquired with a RM Renishaw Raman spectrometer with a class 3B, 514.6 nm green laser. Controlled by Renishaw WiRE, Windows Raman Environment V1.3.15 software. Data was analyzed using GRAMS/32® Spectral Notebase™ V4.15.

#### ***4.2.3.4. Thermogravimetric Analysis***

TGA experiments were performed using TA Instruments Q600 SDT thermal analyzer.

## 4.3. Experimental Methods

### 4.3.1. Operating Personal Safety Measures

#### 4.3.1.2. Personal Protective Equipment (PPE)

All operations involving hydrofluoric acid or  $\text{KF}\cdot 2\text{HF}$  electrolyte were carried out in the walk-in fume hood and may require the use of additional PPE in addition to standard equipment such as a lab coat, nitrile/latex liner gloves, and safety glasses (Table 4.4).

These operations include:

- regular day-to-day experiments (and handling exposed electrodes),
- the replacement of depleted electrolyte,
- preparation of the  $\text{CuF}_2$  reference electrode,
- working around molten electrolyte inside the walk-in fume hood, and
- supporting personnel for the replacement of depleted electrolyte.

During routine operations involving the manipulation of electrodes or connection of electric leads, only the standard PPE was required provided that operations were carried out outside of the walk-in fume hood. These operations include handling exposed electrodes and positioning of fresh electrodes. In these cases, the fume hood door remained closed and the sash was down, with only one's arms extended into the fume hood. Any work involving the handling of molten electrolyte or aqueous HF required the additional use of a chemical-resistant apron and long gauntlet-style gloves if the work was carried out from the outside of the fume hood (Table 4.5) with the sash partially raised. For any work requiring entry into the walk-in fume hood around molten electrolyte or liquid HF, one must wear shoe covers and a full-face shield (or full-face respirator) in addition to the chemical apron and gauntlet-style gloves (Table 4.5). When the solid electrolyte was being mechanically cracked inside the fume hood or the depleted, molten electrolyte was being transferred, one was required to wear the full-face respirator in place of the face shield, to minimize the risk of inhaling any particulates or HF fumes. Finally, any personnel in the supporting role for the replacement of electrolyte (if they remained outside of the fume hood) was required to wear a chemical-resistant apron, medical face mask, as well as safety glasses or a full-face shield

(Table 4.5). An image of complete set of personal protective equipment worn is shown in Figure 4.8.

**Table 4.4: Personal Protective Equipment**

1	Lab coat
2	Nitrile/latex gloves
3	Safety Glasses
4	Long gauntlet-style, neoprene, butyl II, or viton II gloves of 12 to 14 inch length
5	Neoprene, chemical-resistant apron
6	Full-face shield
7	Full-face respirator (3M 6800) with multi gas/vapour cartridge
8	Medical face mask
9	Shoe covers

**Table 4.5: Operations and Required Personal Protective Equipment**

		PPE Required								
		1	2	3	4	5	6	7	8	9
<b>Operation</b>	Routine operations (cell manipulation)	■	■	■	■	■	■	■	■	■
	Solid electrolyte (preparation for cell)	■	■	■	■	■	■	■	■	■
	Molten depleted electrolyte (cell-to-storage)	■	■	■	■	■	■	■	■	■
	Supporting role (outside of fume hood)	■	■	■	■	■	■	■	■	■
	Cu/CuF <sub>2</sub> preparation (handling aqueous HF)	■	■	■	■	■	■	■	■	■

Table illustrating required personal protective equipment for various operations involving potential exposure to hydrofluoric acid, based on PPE listed in table 4.4.

#### **4.3.1.3. Handling and Use of the KF·2HF Electrolyte**

KF·2HF is used as the electrolyte in the molten state maintained at a temperature between 85 to 100 °C for fluorine generation. The solid KF·2HF electrolyte was received a single solid mass contained in sealed 1000 mL Nalgene bottles with screw caps. The solid electrolyte was mechanically broken into smaller pieces suitable for it to be transferred into the electrochemical cell. Full PPE is required to safely transfer the electrolyte because the electrolyte, when struck, breaks into fine particles and is an inhalation hazard, especially when being poured into the cell. The PPE required are: lab coat, chemical resistant apron, full face respirator, latex/nitrile inner gloves, gauntlet-style gloves, as well as shoe covers (Fig. 4.8). The closed Nalgene bottle containing the

electrolyte was placed in a large, sealable plastic bag before being struck with a heavy object to crack the electrolyte. The crushed electrolyte was transferred from the bottle into the electrochemical cell and weighed. When sufficient electrolyte was transferred to the cell (~400 g), the cell cap with the gas shrouds and PTFE blanks were placed on the cell, and was sealed using silicone caulking. Once properly sealed, the cell was carefully inserted into the heater, and supported by a lab jack to achieve the correct position in the heater.

**Fig. 4.8: Photograph of Full Personal Protective Equipment**



Full personal protective equipment showing full-face respirator, lab coat, chemical resistant apron, gauntlet-style gloves, and shoe covers. Not shown: nitrile inner gloves.

When a fresh batch of electrolyte was replaced in the cell and melted for the first time, pre-electrolysis of the melt was carried out to lower the amount of water present in the electrolyte. When the electrolyte was completely molten, a 0.635 cm diameter unwrapped carbon rod was inserted as a sacrificial working electrode, while the counter electrode was a 0.953 cm diameter carbon rod. The working electrode was polarized at 2.5 V (vs. Cu/CuF<sub>2</sub>) for one hour to minimize the amount of water present in the electrolyte. In order to minimize the ingress of moisture from the air, the cell was kept closed except for two venting holes on the gas shrouds, and the electrolyte was maintained in a molten state overnight.

During the course of the experiments, the electrolyte was never handled in the solid or molten form. Between experiments, care was taken when electrodes were switched, because the molten electrolyte adheres to the electrode and may release hazardous HF fumes when outside of the cell. When an electrode was removed from the cell, it was carefully tapped against the inside of the gas shroud to remove any molten electrolyte. The electrode was then carefully placed into a wide-mouthed Nalgene bottle to allow any residual electrolyte to freeze. If another electrode was not immediately inserted into the cell, the gas shroud was capped with a PTFE blank to prevent the release of harmful HF fumes. When electrodes were being switched in-between experiments, and the electrodes were being manipulated from the outside of the fume hood, only partial PPE (lab coat, nitrile gloves, and safety glasses) was required. This was only the case if the fume hood door was kept closed and the sash was down, with only one's arms extending into the fume hood.

When the electrolyte was considered depleted, the cell containing partially frozen KF·xHF electrolyte was removed from the heater, and the electrolyte was carefully poured into a wide-mouthed Nalgene bottle for storage. The bottle was then labelled for regeneration in the future, or disposal.

## 4.3.2. Methodology

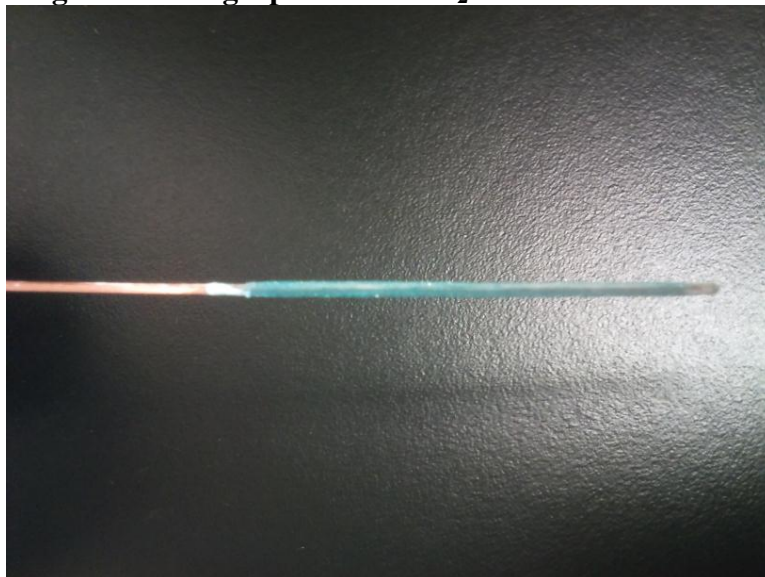
### 4.3.2.1. Preparation of Reference Electrodes

#### Preparation of Cu/CuF<sub>2</sub> Reference Electrode

Standard 18 gauge copper household wiring was stripped of the protective covering and straightened. The bare wire was washed with Sparkleen 1 powdered cleanser, rinsed well with distilled water, and wiped dry. The oxide layer was removed by abrading, and the wire was degreased using acetone then dried in air. A 60 mL polypropylene bottle with a screw cap was used as the reaction vessel. A 1.59 mm hole was drilled in the cap, then the cap was wrapped in two layers of Parafilm to maintain a seal for the aqueous HF, and roughly 5 cm of wire was inserted through the film and cap into the bottle.

Approximately 15 mL of aqueous HF was transferred into the reaction bottle using a polypropylene funnel. A high concentration of HF was not required for the formation of the CuF<sub>2</sub> coating, because the coating process was carried out over several weeks. The bottle was quickly and carefully recapped using the wire-inserted bottle cap making sure that the aqueous HF did not spill and the wire did not make direct contact with the aqueous HF. The height of the wire was adjusted so that the bottom of the wire was at

**Fig. 4.9: Photograph of Cu/CuF<sub>2</sub> Reference Electrode**



Cu/CuF<sub>2</sub> reference electrode for KF-2HF cell electrolyte

least 1 cm above the surface of the aqueous HF solution, and was positioned vertically in the bottle. The wire was left exposed for 2 to 3 weeks until a uniform, blue  $\text{CuF}_2$  coating was observed (Fig. 4.9). The electrode was then carefully removed from the lid to avoid any damage (cracking of the film) to the coating, allowed to dry in air, and was transferred to a desiccator for storage.

The  $\text{Cu}/\text{CuF}_2$  reference electrode used for electrochemical experiments was uncalibrated, but was estimated to be  $\sim +0.5$  V vs. SHE. The  $\text{Cu}/\text{CuF}_2$  reference electrode was replaced when black spots on the copper wire or visible damage to the  $\text{CuF}_2$  film appeared.

#### Preparation of Ag/AgI Reference Electrode

A 0.5 mm  $\text{Ag}/\text{Ag}^+$  electrode (CH Instruments) wire was thoroughly cleaned with Sparkleen 1 (Fisher Scientific) powdered cleanser, rinsed well with distilled water and wiped dry. Any remaining organic material on the wire was then removed with ethanol before being wiped dry again. A Pt wire CE was washed with powdered cleanser, rinsed well with distilled water, and wiped dry. The wire was then rewashed using ethanol before being wiped dry for a second time. A 0.01 mol/L KI solution was prepared by dissolving 414 mg of KI in distilled water and diluting to 250 mL. Sufficient KI solution was transferred to a 250 mL beaker to ensure that the Ag wire would be submerged during electrolysis. Using a 9.0 V battery, the Ag wire electrode was connected to the positive terminal (anode), while the Pt wire was connected to the negative terminal (cathode). The Ag wire was then immersed into the gently stirring KI solution until a smooth, thin yellow coating of AgI was deposited on the Ag wire (Fig. 4.10) (approximately 30 min). The electroplating of the AgI was performed in a darkened room because AgI is photosensitive and decomposes in light. The electrode was removed from the KI solution, and carefully wiped dry with Kim-wipe paper. The Ag/AgI electrode was then rinsed well with distilled water and wiped dry again.

A saturated NaI-PC solution was prepared as a filling solution for the Ag/AgI reference electrode. A syringe was used to fill the glass body of the RE with the NaI solution to avoid any trapped bubbles in the tube. The Ag/AgI wire was carefully inserted into the tube, taking care to avoid contact with the sides of the glass which may damage the coating. The completed reference electrode (Fig. 4.10) was stored in a capped plastic

tube which was wrapped in electrical tape to protect the AgI layer from light.

**Fig. 4.10: Photograph of Ag/AgI Reference Electrode**



Ag/AgI reference electrode for galvanostatic experiments

#### ***4.3.2.2. Electrochemical Fluorinations***

Various electrochemical methods were selected to carry out the fluorination of carbon electrodes, as well as assess the effects of polarization by the change in the reaction efficiency of a particular sample. Each of the electrochemical methods outlined in this section have a specific purpose in the examination of the overall C/KF·2HF system.

##### Open Circuit Potential

An open circuit potential (OCP) measurement is the potential measured between the working and reference electrode when no current is applied to the electrodes. The OCP is dependent on the background reactions present on the electrodes and are dependent on the surface chemistry. When a carbon electrode has been polarized in the KF·2HF media, the OCP changes as the difference in potential between the working electrode and the reference electrode change. This method is useful to measure when a polarized electrode (or local solution) has returned to equilibrium. This ensures that subsequent measurements (particularly the EIS measurements) focus on the physical structure of the

fluorinated electrodes rather than active, residual electrochemical processes remaining from a polarization.

### Polarization

A polarization (or, potentiostatic) measurement is an electrochemical method in which the potential is held at a constant value while the current is recorded as a function of time. This is the primary method to carry out fluorine discharge studies in an electrochemical cell. This method pushes the electrode potential into a range at which the particular reactions can be studied with greater detail.

### Cyclic Voltammetry

Cyclic voltammetry (CV) is a potential sweep method where the electrode potential is changed linearly with time from an initial value to a final value, at which point the potential is swept in the opposite direction to another set-point. The current is recorded as a function of time, and is used to quickly access the electrochemical processes occurring over a potential region. It is particularly useful to assess the degree of electrode passivation based on how the current is limited at high potentials by an insulating  $CF_x$  layer.

### Galvanostatic

Galvanostatic measurements are experiments in which a constant current is applied across two electrodes, and a third electrode, the reference electrode, measures the potential response of the working electrode as a function of time. Galvanostatic experiments are used to force the reduction of species on the cathodic working electrode to occur at a constant rate, to measure how reducible species on the electrode are.

### Electrochemical Impedance Spectroscopy/AC Impedance

Electrochemical impedance spectroscopy (EIS) is a method which measures the system response to the application of a small amplitude AC signal. The impedance response provides a measure of the capacitance and resistance at the solution/electrode interface in relation to the frequency of the AC signal.

## Experimental Conditions

Electrochemical polarization experiments for fluorination of the electrodes were carried out in KF·2HF cell electrolyte. Measurements were carried out at a nominal temperature of  $90 \pm 5$  °C, and the electrolyte was kept molten in the electrochemical cell using a specially designed electrolyte heater (described above). The cell container was a 250 mL PMP beaker with machined PTFE cell components—lid, gas shroud, electrode holders (described below). In the fluorine cell, the counter electrode was a carbon rod and the reference electrode was Cu/CuF<sub>2</sub> (+0.40 V vs. SHE) [45] exposed directly to the cell electrolyte. All electrode potentials measured in the melt are quoted relative to the experimental Cu/CuF<sub>2</sub> reference electrode. All carbon electrodes were positioned vertically to promote bubble detachment from the surface. The concentration of the molten salt electrolyte was assumed to be KF·2HF regardless of the age/history of the electrolyte (before it was considered to be depleted). An example of the electrochemical experiments involved with fluorinating carbon anode materials is described in section 4.4 of this chapter.

Electrochemical impedance measurements were performed at 0.5 V with a 10 mV RMS amplitude over a frequency range of  $10^5$  to  $10^0$  Hz (10 measurements per decade). The AC voltage response was integrated over 100 cycles vs. voltage until a maximum standard deviation of 10% was achieved (“V1, short” setting).

Measurements made using the Solartron potentiostat were estimated to be accurate within  $\pm 5$  mV of the stated values. The error for applied potentials were  $\pm 8$  mV and the error in current was ~5%.

### ***4.3.2.3. Galvanostatic Discharge Experiments***

Galvanostatic experiments were conducted in PC with LiClO<sub>4</sub> supporting electrolyte (PC-LiClO<sub>4</sub>). A 250 mL PMP beaker was used as the cell container with machined PTFE cell components. Galvanostatic experiments were carried out in ambient air at a temperature of  $22 \pm 2$  °C, since a low oxygen environment (i.e., a glove box) was not available. The carbon samples were fluorinated graphite rods that had been polarized in KF·2HF at 6.0 V for a total charge density of 50 C/cm<sup>2</sup>. The total charge applied to each graphite

rod sample was normalized to the exposed surface area for fluorination. Once the rods had been fluorinated, the electrodes were washed with hot (~95 °C) demineralized water to remove any frozen electrolyte that had adhered to the electrode. The rods were quickly wiped to remove excess water and left to dry in air. Once dried, the electrode was inserted into the cell equipped with an Ag/AgI reference electrode and Pt foil counter electrode. Cathodic current densities of 1 mA/cm<sup>2</sup> down to 0.025 mA/cm<sup>2</sup> were applied across the electrodes for 1200 seconds. The electrodes were considered to be depleted if the potential dropped to approximately -1.0 V (vs. Ag/AgI). All galvanostatic experiments were carried out in an open-air environment, in a darkened room to prevent delamination of the AgI coating from the reference electrode.

#### *4.3.2.4. Raman Spectroscopy*

A more complete description of the technique is provided in Appendix 1.

The carbon samples selected for analysis using Raman spectroscopy were polarized potentiostatically at the desired potential. After fluorination, the samples were washed with hot demineralised water to remove frozen electrolyte that had adhered to the surface of the electrode. Once the Raman laser was on and set up, the carbon sample was placed into the optical microscope. The position on the bare carbon for the Raman laser was selected based on the amount of carbon that could be focused clearly at the highest magnification (300 X). Once the image was focused, the Raman instrument was switched from optical view mode to laser mode. The Raman laser was further focused (as much as possible) to a single point using the optical microscope. This minimized the signal-to-noise ratio of the outputted data. Once focused, the instrument was controlled using software to make 20 scans over the wavelength range of 4000 to 400 cm<sup>-1</sup>. When the scans were complete, the instrument was returned to optical view mode and the sample was removed. The deconvolution method was applied to the Raman spectra with a curve fitting scheme to minimize  $\chi^2$  values of fitted peaks. The data file was exported as an ASCII text format for further re-plotting and analysis.

#### *4.3.2.5. Characterization of Carbon by Thermogravimetric Analysis*

Small samples of the carbon electrode materials were cracked into small pieces and were

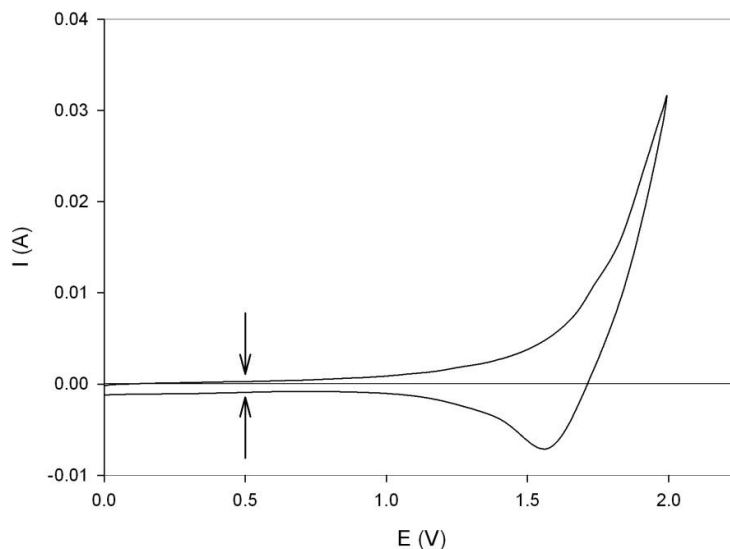
used as-is, without grinding the sample into a powder. The carbon samples were heated from room temperature to 1000 °C at the rate of 5 °C/min under flowing Argon gas atmosphere (50 mL/min).

#### *4.3.2.6. Fitting Criteria of EIS Data*

Impedance experiments were conducted in between individual potentiostatic polarization experiments to obtain impedance measurements of the double-layer capacitance. Impedance measurements were taken at 0.5 V (vs. Cu/CuF<sub>2</sub>), where electrochemical processes are in the double-layer region (Fig. 4.11) and no major reactions occur. Therefore, the impedance measurements were only dictated by physical effects. The capacitance values were obtained by a non-linear, least-squares method of the impedance results over the frequency range of 10<sup>5</sup> to 10<sup>4</sup> Hz. The high frequency range makes it possible to study the outer layers of the C/KF·2HF interface (region A and B, Fig. 3.3), without the contributing effects of the slower processes caused by the microstructure. Once the frequency range was selected, an instant fit was performed using ZView® to obtain preliminary capacitance and resistance values. Once complete, the values were transferred over to a prepared equivalent circuit to further improve the fit. The fitting of the impedance data over the frequency range was improved using 100 optimization iterations, although the fitted circuit values were not manually optimized to obtain a better fit. Certain stray data points were omitted during the data selection of the fitting if the  $\chi^2$  value was found to decrease by one order of magnitude over the limited frequency range of the fitting. A KK (Kramers-Kronig) transform was applied to the fitted values for the different circuit components of the basic RC circuit to examine the suitability of the circuit model against the measured values. The  $\chi^2$  value reflects the overall goodness-of-fit for all of the fitted circuit component values, and not individual components.

Although impedance measurements were taken over a frequency range of 10<sup>5</sup> to 10<sup>0</sup> Hz, the data values were fit over a smaller range. The complete ranges of values were not fitted to a circuit simply because for many results, the resistances were too high to obtain meaningful data at the lower frequency range. In multiple cases, the smallest frequency that could be used to obtain reasonable impedance measurements was ~100 Hz. As previously stated, the upper frequency range was used to study the surface layer effects

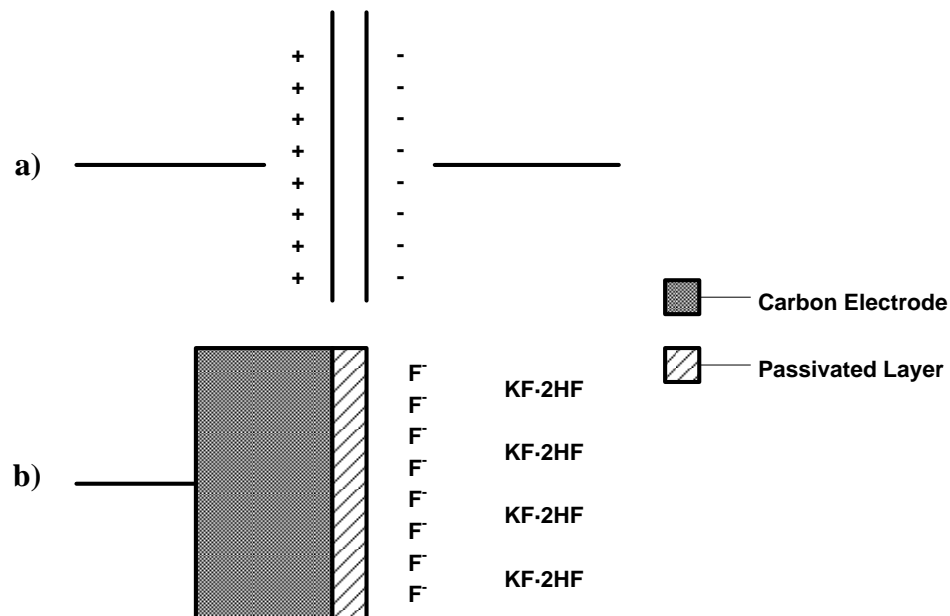
**Fig. 4.11: Selection of Potential for in Double-Layer Region**



Cyclic voltammogram showing selection of potential for EIS experiments as being in the double-layer region (in absence of a reaction). Arrows show potential for impedance measurement. Carbon sample was a graphite rod in KF·2HF at 90 °C with a 100 mV/s sweep rate. Potential is reported vs. Cu/CuF<sub>2</sub> reference electrode.

where the processes occur much faster than within the electrode itself, which are more sensitive to slower frequency perturbations. In addition, a frequency range fitted to a circuit model to obtain capacitance values was more representative of the physical surface where measurements are heavily influenced by solution resistance as well as resistance from the passivated layer. This is in contrast to a simple parallel-plate model (Fig. 4.12) that strictly assumes that the surface only has capacitive characteristics. When data was fitted to a single capacitance value at a single frequency, larger error values were obtained because the fitting process was limited without more data points for comparison. In addition, since even the most basic circuit models account for solution resistance and resistance of the surface layer, the errors obtained from the fit of a single data point yield unrealistic values. As shown in section 3.2.3., it was not necessary to develop a more complex equivalent circuit than the one shown in Table 4.3.

**Fig. 4.12: Representation of  $CF_x$  Layer as Electrical Double-Layer**



Representation of  $CF_x$  passivated layer and carbon electrode as electrical double-layer, where a) is the electrical equivalent of b) the physical system. Positive carbon anode creates an electrical double-layer through the  $CF_x$  layer involving negatively charged fluoride ions from the bulk  $KF \cdot 2HF$  electrolyte.

#### 4.4. Sample Experimental Procedure

In order to examine the effect of potential and the fluorine discharge reaction on the surface conditions of the carbon anode materials, a series of polarization experiments were required. An example of an electrochemical experimental series, is given below:

- 1) OCP, 300 seconds
- 2) Potentiostatic, 0.5 V, 300 seconds
- 3) OCP, 300 seconds
- 4) Cyclic Voltammetry, 0 to 8.0 V, 100 mV/s, 2 sweeps
- 5) Potentiostatic, 0.5 V, 300 seconds
- 6) Potentiostatic, 4.0 V, 2400 seconds
- 7) Potentiostatic, 0.5 V, 300 seconds
- 8) OCP, 300 seconds
- 9) Electrochemical Impedance, 0.5 V vs. OCP, 10 mV RMS amplitude,  $10^5$  to  $10^0$  Hz (8 times)

10) Repeat steps 6 – 9 sequentially for potentials 5.0 – 8.0 V.

...

31) Cyclic Voltammetry, 0 to 8.0 V, 100 mV/s, 2 sweeps

The experiment series was designed to yield a wide variety of information about the electrochemical properties of the different carbon anode materials.

- a) In order to obtain information on the effect of a short-term polarization on the electrochemical characteristics of the carbon anode, CV experiments conducted at the beginning of the series were compared to the voltammograms obtained at the end of the series. The initial CV scan conducted on a fresh electrode surface provided information such as the peak current density, critical potential prior to electrode deactivation by bubble adhesion, and decay in electrode performance on subsequent scans. The final CV run after approximately 3.5 hours of polarization at potentials greater than the FDR potential (~4.0 V) would show the effects of passivation and intercalation that incurred during the series of polarizations. A comparison of the peak current densities clearly illustrates the negative effects of electrode passivation, caused by the insulative effects of the passive layer, or kinetic effects due to bubble adhesion. The series is considered short-term, since industrial electrodes are expected to operate continuously at relatively high currents for thousands of hours. Thus, it would be difficult to replicate the full effects of a long-term polarization on electrodes in the current laboratory setup.
  
- b) To determine the optimal potential for the FDR in the current cell configuration, it was determined to be the potential at which the highest amount of charge was passed (potentiostatically) for each applied potential. The amount of charge relates to how much fluorine was evolved as a gas, intercalated into the electrode, or reacted with the carbon surface (as a  $\text{CF}_x$  passivating layer). The steady state current extracted from the potentiostatic measurements yields information regarding the onset of electrode deactivation.

- c) To study the growth of the  $CF_x$  passive film at potentials greater than the FDR potential, the thickness of the  $CF_x$  electrical double-layer was calculated from the measured impedance of the C/KF·2HF interface at high frequencies. The  $CF_x$  is highly insulating, and should show a strong relationship between the polarization potential and resistance (or impedance). Impedance measurements of the passive film following each polarization can yield this useful information and identify critical conditions for passive layer formation.
  
- d) To determine which of the selected carbon anode materials were the most effective for fluorine generation, the total amount of charge passed over the polarization series (section 3.4) for each of the carbons selected, is related to the amount of FDR that has occurred.

## 4.5. Characterization of Carbon Electrode Materials by TGA

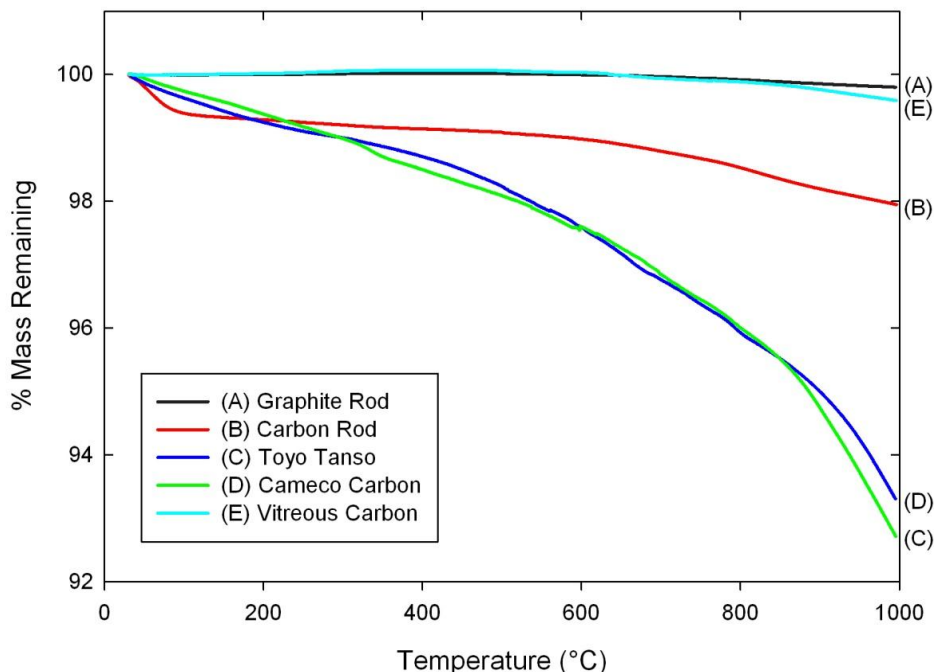
### 4.5.1 Background

Thermogravimetric analysis (TGA) is used to study the decomposition profile of a material or compound by measuring the weight change and heat flow at elevated temperatures. This method is useful for determining the purity of a sample and studying decomposition reactions. The samples were studied under an Argon atmosphere in order to loosely differentiate carbon samples based on the quantity of impurities present and microstructural phase transformations which may affect the electrochemical properties of the electrode material as a whole. The residue from TGA under an Argon atmosphere was mainly carbon or other minor impurities that did not react under the experimental conditions. In contrast, TGA under an air atmosphere would allow carbon to react with oxygen in the air stream to form  $CO_2$ , making it difficult to differentiate the volatile products evolved without further elemental analysis.

### 4.5.2. Sample Impurity

The thermal stability of the unexposed carbon samples under an Ar atmosphere at a heating rate of 5 °C/min is shown in Figure 4.13. The graphite rod and vitreous carbon

**Fig. 4.13: TGA of Carbon Materials in Ar**



Percent mass remaining as a function of temperature for carbon materials: (A) graphite rod, (B) carbon rod, (C) Toyo Tanso carbon, (D) Cameco carbon, (E) vitreous carbon. Conditions: Ar atmosphere, 5 °C/min heating rate.

had high thermal stability up to 600 °C prior to minor decomposition down to 99.8% and 99.6% of initial mass, respectively. These two carbon samples had no appreciable loss in mass, even with heating to high temperatures, indicating that they had a high degree of purity. The graphite rod was prepared by an extrusion process with an extensive heat treatment at high temperatures to obtain a high degree of graphitization. Any non-graphitic carbon precursors or binder used would have been transformed or burned off during the baking process. Over the course of the TGA experiment the binders present undergo volatilization giving rise to a negative (endothermic) derivative heat flow profile that accompanies the loss in mass (Fig. 4.14). In contrast, the high purity of the vitreous carbon stems from the process required to synthesize this material, namely the thermal degradation of (specific) organic polymers followed by heat treatment at temperatures above 1000 °C for several days. Vitreous carbon does not require the use of organic binders, unlike graphitic or amorphous carbon materials which would normally be

extruded or pressed during production. Naturally, the vitreous carbon is a highly pure form of non-crystalline graphite, and would not be expected to decompose significantly at these relatively low temperatures (compared to that required for its synthesis) (Fig. 4.15). The carbon rod underwent a 0.5% loss in mass starting at 100 °C which was attributed to the evaporation of adsorbed water, followed by a period of thermal stability up to 600 °C, before decaying further to 98% of the original mass (Fig. 4.16).

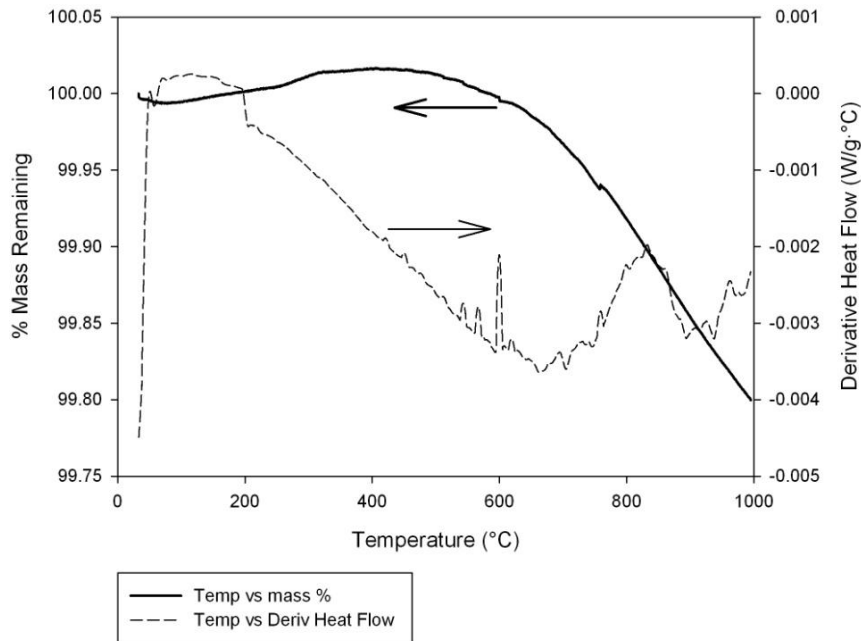
The carbon rod was expected to be highly graphitized, undergoing a similar heat treatment process as that of graphite rod. Lower graphite content suggests that the rod was not subjected to the same heat treatment as the graphite rod, in order to limit graphitization of the carbon precursors. A greater amount of residual binders or carbon precursors would remain, explaining the larger change in mass and derivative heat flow over the TGA experiment (Fig. 4.16), since more volatile compounds would be removed.

The industrial amorphous carbon materials (Toyo Tanso and Cameco) have significantly different thermal decomposition profiles than the graphitic carbons. The mass decreased gradually between 30 and 800 °C, at which point the rate of mass loss increased slightly towards the end of the TGA experiment. The residue was 93% to 93.5% of the initial mass. This 7% change in mass is attributed to the presence and evaporation of binders such as coal-tar pitch or other volatile compounds in the material. The melting and evaporation of the coal-tar pitch would be consistent with a phase change based on the (overall) endothermic derivative heat flow profile (Fig. 4.17). Further, the peak in the heat flow at 800 °C which corresponds to the decomposition of the more stable chemical bonds in the binder, and a change in the rate of mass loss (Fig. 4.18). The TGA curve for a sample of coal-tar pitch is given in Figure 4.19. Although the rate of mass loss above 500 °C is small, the TGA results are consistent with the overall decomposition rates observed on the carbon material samples, particularly for the carbon rod and amorphous carbons. Industrial amorphous carbon materials are prepared through cold-isostatic pressing or by extrusion. In either process, the resulting material would not be subjected to an extensive heat treatment to avoid graphitization of the amorphous carbon precursors, and so a greater amount of coal-tar pitch would be present.

### 4.5.3. Summary

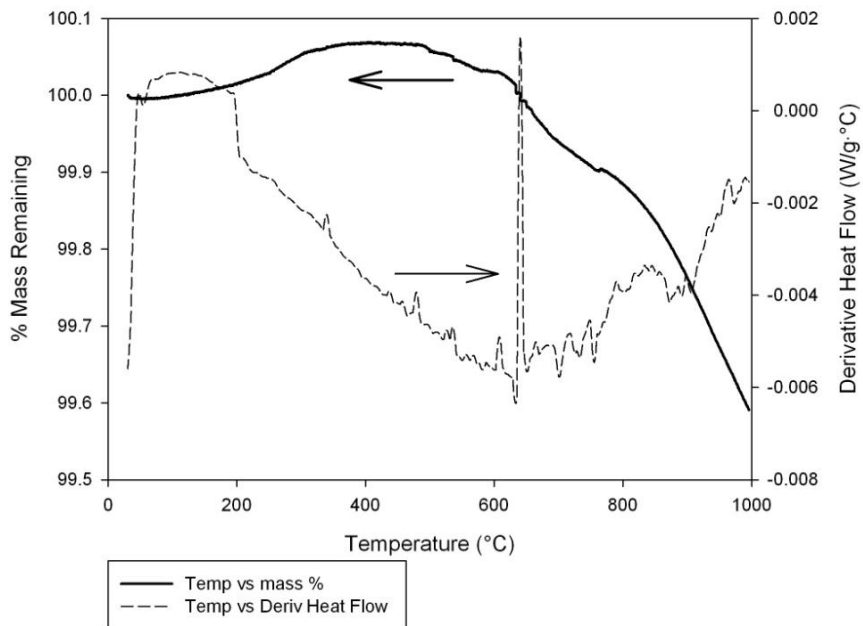
The carbon anode materials were heated to 1000 °C in an Ar atmosphere. The industrial amorphous carbons have the highest amount of non-carbon impurities, making up approximately 7% of the overall mass. The impurity was expected to be coal-tar pitch, which is a common binder used in the manufacture of extruded amorphous carbon materials. The graphitic rods (graphite and carbon rod) and vitreous carbon are highly pure forms of carbon, undergoing minimal changes in mass (~0.5 to 2%).

**Fig. 4.14: TGA of Graphite Rod in Ar**



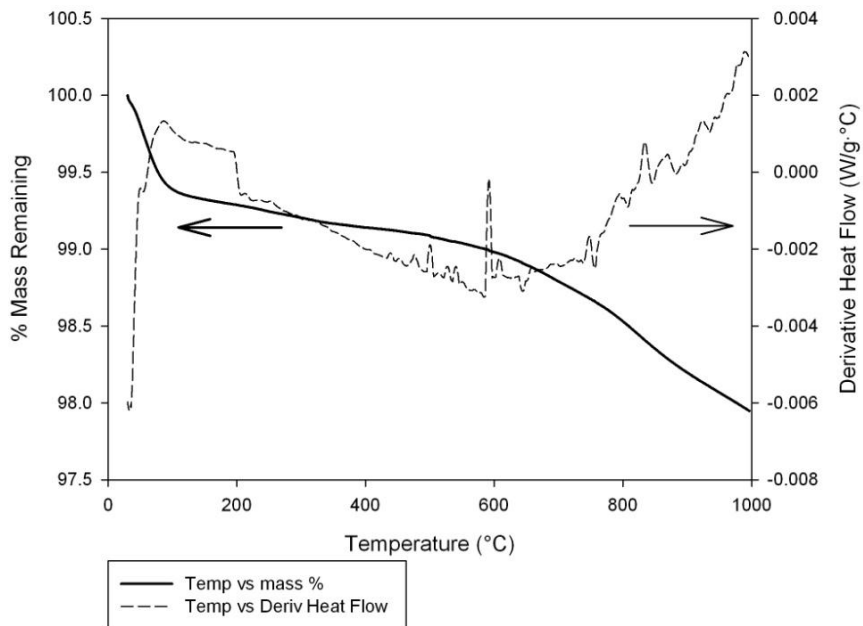
TGA of graphite rod showing % mass remaining (left, —) and derivative heat flow (right, ---). Conditions: Ar atmosphere, 5 °C/min heating rate.

**Fig. 4.15: TGA of Vitreous Carbon in Ar**



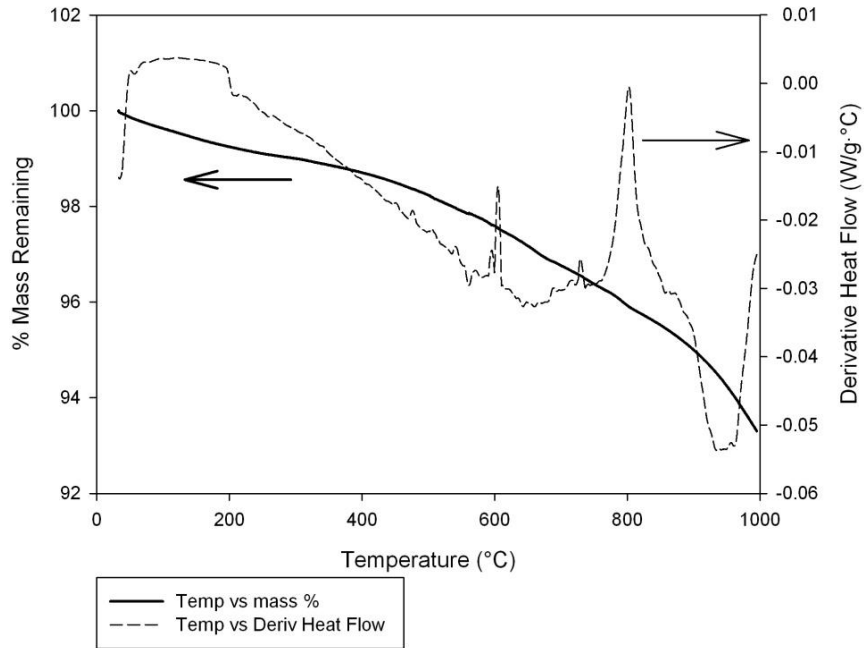
TGA of vitreous carbon showing % mass remaining (left, —) and derivative heat flow (right, - - -). Conditions: Ar atmosphere, 5 °C/min heating rate.

**Fig. 4.16: TGA of Carbon Rod in Ar**



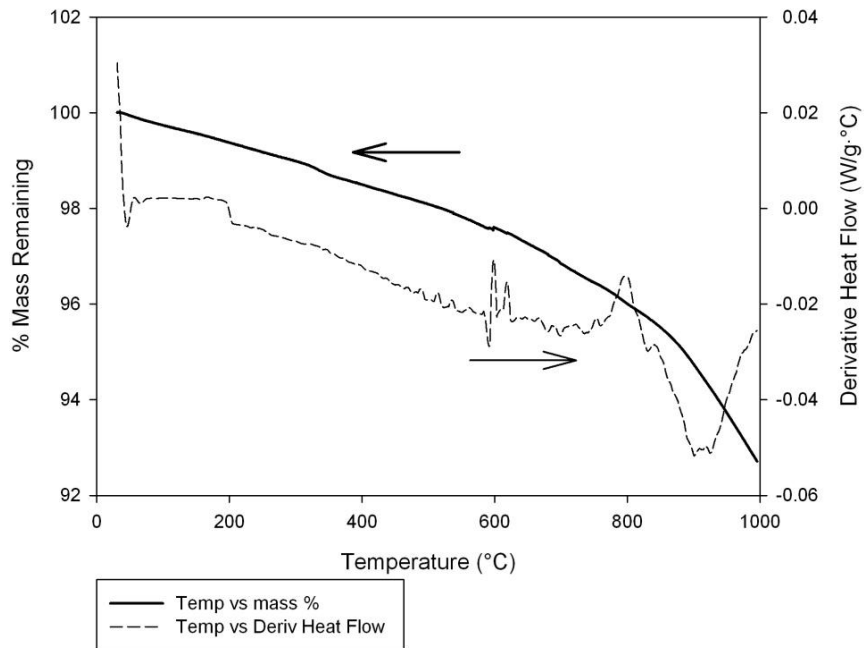
TGA of carbon rod showing % mass remaining (left, —) and derivative heat flow (right, - - -). Conditions: Ar atmosphere, 5 °C/min heating rate.

**Fig. 4.17: TGA of Toyo Tanso Amorphous Carbon in Ar**



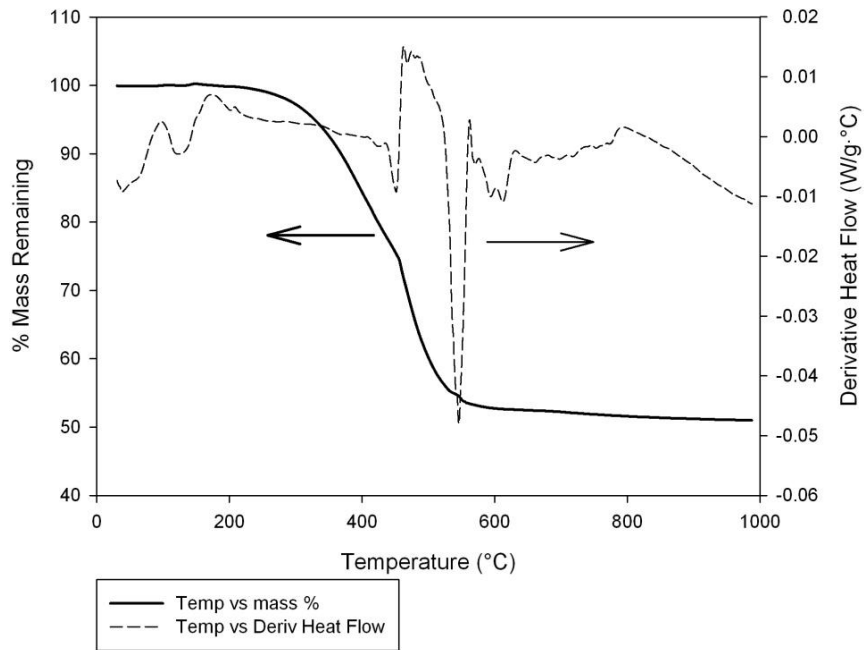
TGA of Toyo Tanso amorphous carbon showing % mass remaining (left axis, —) and derivative heat flow (right axis, - - -). Conditions: Ar atmosphere, 5 °C/min heating rate.

**Fig. 4.18: TGA of Cameco Amorphous Carbon in Ar**



TGA of Cameco amorphous carbon showing % mass remaining (left axis, —) and derivative heat flow (right axis, - - -). Conditions: Ar atmosphere, 5 °C/min heating rate.

**Fig. 4.19: TGA of Coal-Tar Pitch in Ar**



TGA of Coal-Tar Pitch binder showing % mass remaining (left axis, —) and derivative heat flow (right axis, - - -). Conditions: Ar atmosphere, 5 °C/min heating rate.

## 5. Results

### 5.1. Polarization Experiments

#### 5.1.1. Steady State Currents ( $I_{ss}$ )

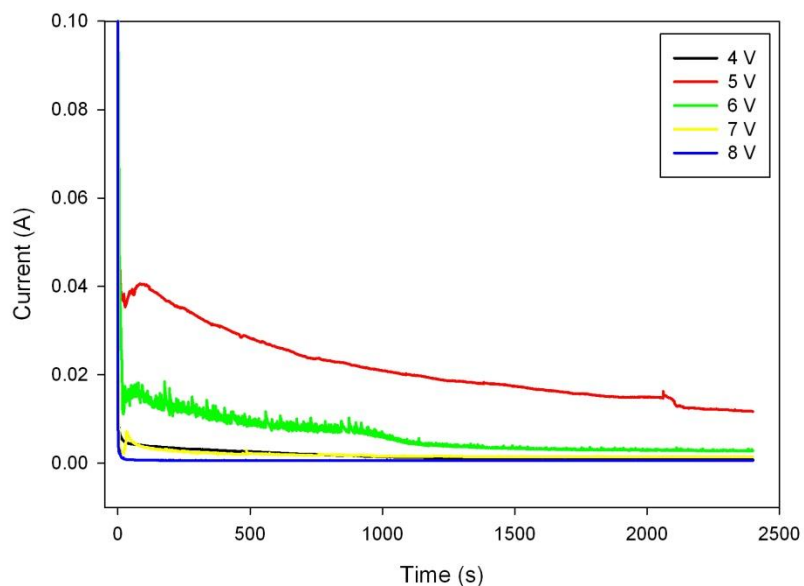
The steady state current is the rate at which the fluorine discharge reaction (FDR) can be sustained at a particular potential. Fresh carbon electrodes were polarized in series for 40 minutes at each potential, at progressively higher potentials (from ~4.0 to 8.0 V). The potentials selected were above the starting potential for the FDR (~4.0 V). The current decay curves for potentiostatic experiments of the carbon materials polarized in series are given in Fig. 5.1 to 5.5. The steady state currents ( $I_{ss}$ ) for the carbon electrode materials are summarized in Fig. 5.6. For the graphite rod, the  $I_{ss}$  at 5.0 V was larger than that at 4.0 V, but decreased significantly during subsequent potentiostatic polarizations at 6.0 to 8.0 V as more charge had been passed (Fig. 5.7).

The industrial amorphous carbons showed consistently higher  $I_{ss}$  over the potentials tested, clearly indicating their effectiveness at the FDR compared to the graphitic samples. The Toyo Tanso carbon had  $I_{ss}$  values greater than 40 mA/cm<sup>2</sup> for applied potentials between 5.0 and 7.0 V, before reaching a kinetic limit at 8.0 V (Fig. 5.6). The optimal potential for fluorine generation on the Cameco carbon appeared between 6.0 and 7.0 V because high rates of reaction were obtained (~80 mA/cm<sup>2</sup>). A four-fold increase in the  $I_{ss}$  between 5.0 and 6.0 V indicated that the rate of FDR was potential-dependent, and unlike the graphitic samples, was not inhibited at 6.0 V by processes such as electrode passivation. For both amorphous carbons, the  $I_{ss}$  value decreased significantly at 8.0 V (Fig. 5.6). The vitreous carbon electrode, however, had consistently low  $I_{ss}$  values, with the highest current occurring at 5.0 V. The electrode was deactivated by 6.0 V and the  $I_{ss}$  did not increase further with increasing potentials.

#### 5.1.2. Charge vs. Potential

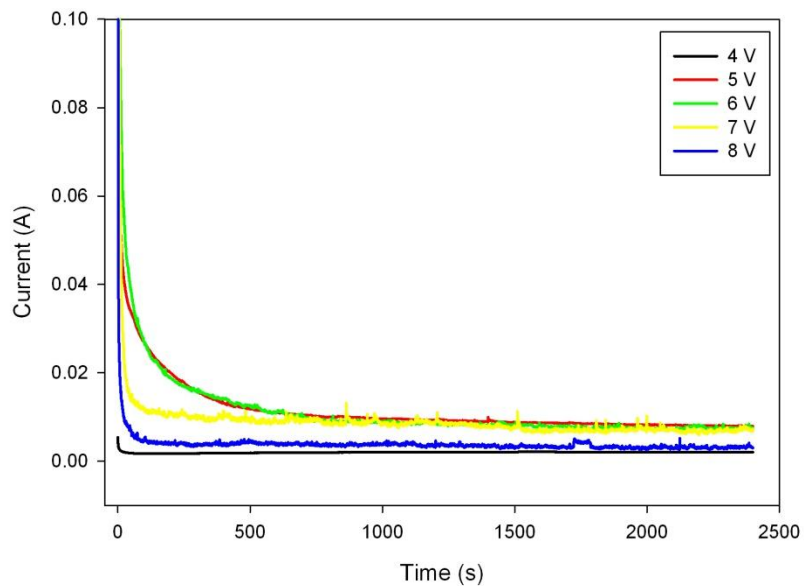
The amount of charge passed was used as a measure of how effective each carbon material was for fluorine generation, since the total charge is related to the amount of FDR that had occurred. For the two graphitized carbon samples (the graphite and carbon rod), the cumulative charges passed over the duration of the experiment were 101 and

**Fig. 5.1: Potentiostatic Response of Graphite Rod Polarized from 4.0 to 8.0 V**



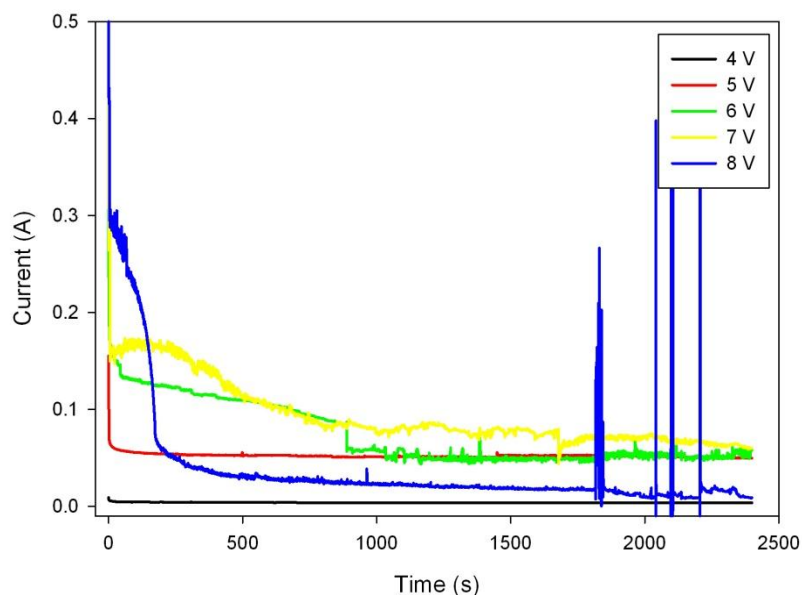
Potentiostatic response of graphite rod sample polarized in series from 4.0 to 8.0 V for 40 minutes at each potential.

**Fig. 5.2: Potentiostatic Response of Carbon Rod Polarized from 4.0 to 8.0 V**



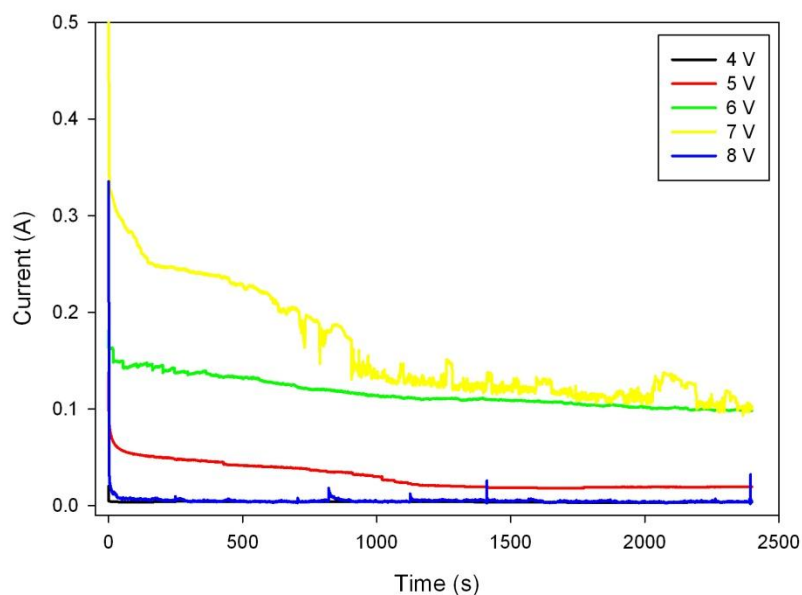
Potentiostatic response of carbon rod sample polarized in series from 4.0 to 8.0 V for 40 minutes at each potential.

**Fig. 5.3: Potentiostatic Response of Toyo Tanso Carbon Polarized from 4.0 to 8.0 V**



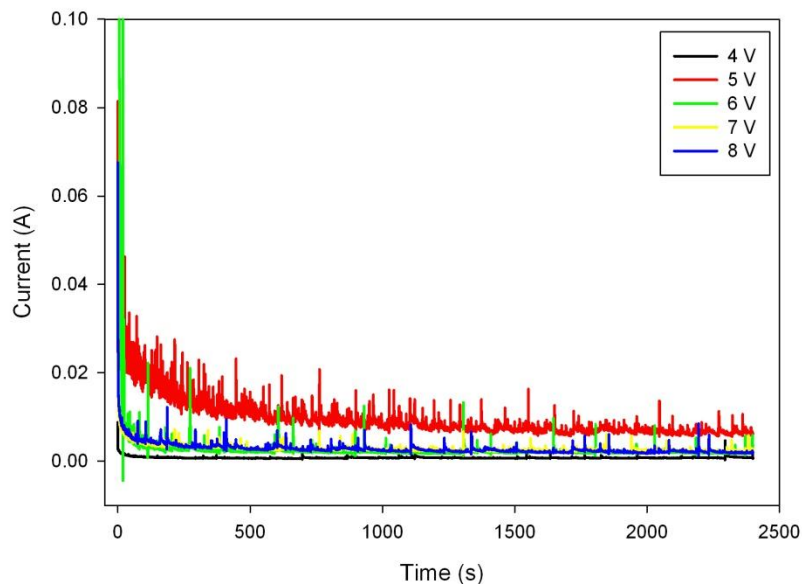
Potentiostatic response of Toyo Tanso carbon sample polarized in series from 4.0 to 8.0 V for 40 minutes at each potential.

**Fig. 5.4: Potentiostatic Response of Cameco Carbon Polarized from 4.0 to 8.0 V**



Potentiostatic response of Cameco carbon sample polarized in series from 4.0 to 8.0 V for 40 minutes at each potential.

**Fig. 5.5: Potentiostatic Response of Vitreous Carbon Polarized from 4.0 to 8.0 V**

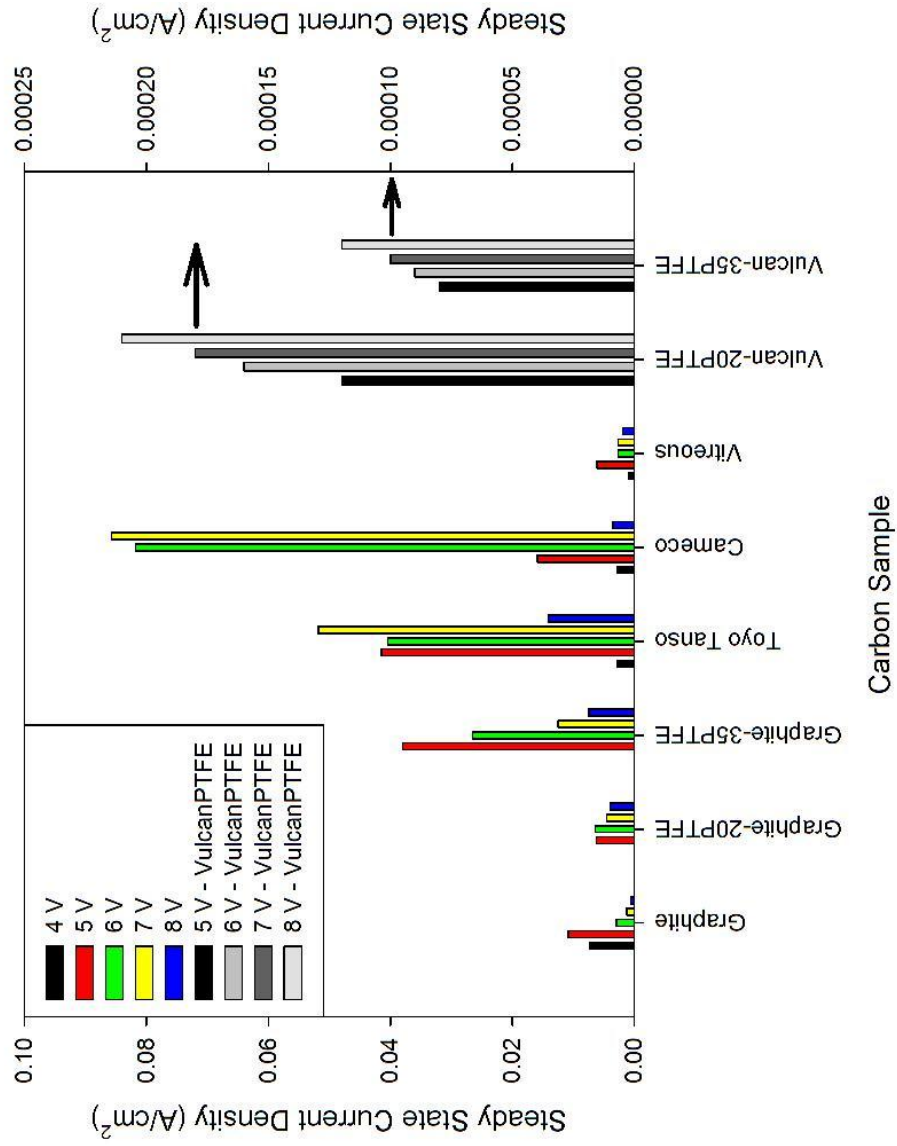


Potentiostatic response of vitreous carbon sample polarized in series from 4.0 to 8.0 V for 40 minutes at each potential.

86 C, respectively (Fig. 5.8). The two samples displayed similar electrochemical responses, with the most charge being passed at 5.0 or 6.0 V (Fig. 5.7). In both cases, the amount of charge passed at each potential dropped off quickly after this point, and did not increase even during polarizations at higher potentials. The Toyo Tanso and Cameco industrial amorphous carbons passed increasing amounts of charge with increasing positive potential up to 7.0 V before being significantly inhibited at 8.0 V. At the end of the experiment, the amorphous carbons passed significantly more charge (692 and 838 C, respectively) over the potential range tested, compared to the graphitized carbon samples (Fig. 5.8).

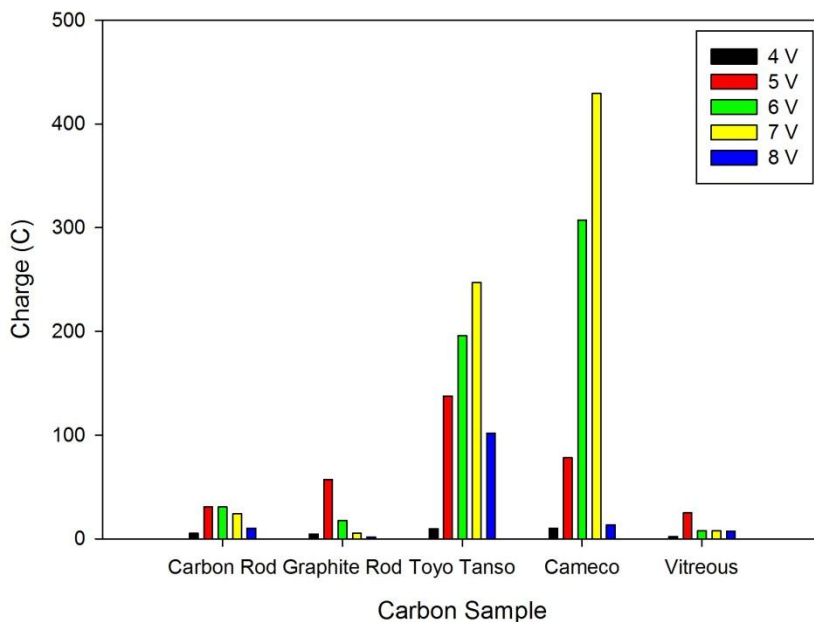
Vitreous carbon passed the lowest amount of charge (49 C) over the applied potential series (Fig. 5.8), indicating that it was the least effective for fluorine generation. The vitreous carbon sample was passivated early at 4.0 V, completely hindering the FDR at potentials greater than 5.0 V (Fig. 5.7).

**Fig. 5.6: Steady State Current Density vs. Potentials from 4 to 8 V**



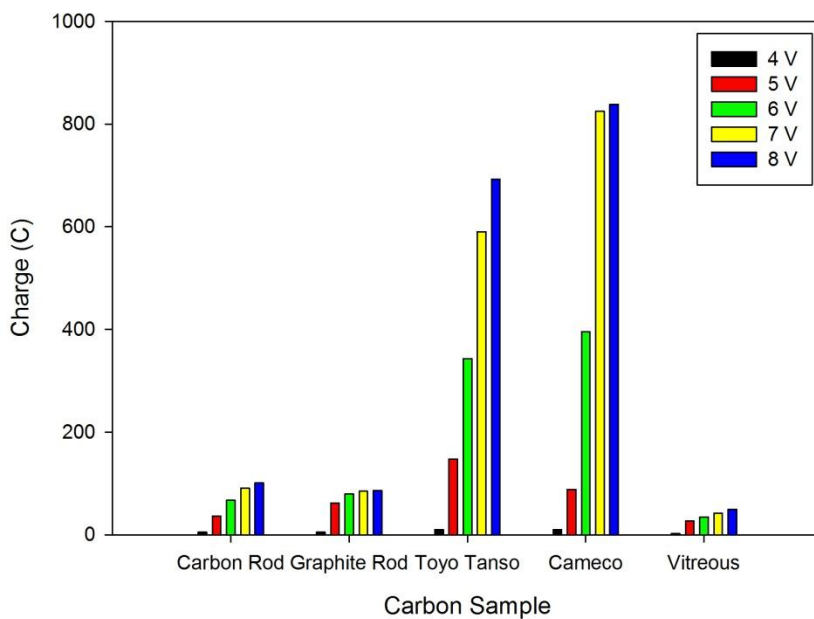
Steady state currents for carbon samples polarized in series from 4.0 to 8.0 V for 40 minutes. Graphite to vitreous carbon samples follow primary axis, while Vulcan-PTFE samples [73] follow secondary axis.

**Fig. 5.7: Charge vs. Potential for Different Carbon Materials**



Charge passed for each carbon electrode sample at each potential from 4.0 to 8.0 V for 40 minutes.

**Fig. 5.8: Total Cumulative Charge Over Polarization Series vs. Potential for Different Carbon Materials**



Cumulative charge passed for each carbon sample at each potential polarized, from 4.0 to 8.0 V for 40 minutes at each potential, showing overall effectiveness of the FER on each carbon.

### 5.1.3. Cyclic Voltammetry

Voltammetric sweeps showing the electrochemical response of four carbon materials before and after the short-term polarization series are given in Figures 5.9 to 5.12. The initial potential sweep on a fresh graphite rod electrode (Fig. 5.9a) reached a peak current density of approximately  $0.8 \text{ A/cm}^2$  at 8 V on the first sweep, but only a maximum current density of  $0.5 \text{ A/cm}^2$  (at 7.0 V) on the second sweep. Whereas the first sweep was relatively smooth between 5.0 and 8.0 V, the second sweep was noisy from 5.0 to 7.0 V and the current became significantly limited at 8.0 V ( $\sim 0.05 \text{ A/cm}^2$ ). The roughness of the voltammetric curve was attributed to the rapid formation and detachment of gas bubbles from the surface of the electrode (Fig. 5.10). Industrial amorphous carbons displayed a much different voltammetric response compared to graphite (Fig. 5.11a and 5.12a). Both the Toyo Tanso and Cameco carbons achieved high current densities on the first sweep ( $0.70$  and  $0.75 \text{ A/cm}^2$ , respectively). On the second sweep, the peak current density on the Toyo Tanso decreased slightly to  $0.60 \text{ A/cm}^2$ , while the Cameco carbon was unchanged from the first sweep. Compared to the graphite rod, both the curves were smooth at high potentials and small bubbles were observed coming off the surface at potentials as low as 4.0 V. Similar to the industrial amorphous carbons, the vitreous carbon had potential sweeps that were relatively linear, although the slope changed slightly between the first and second sweep. Large peak current densities of  $1.1$  and  $0.90 \text{ A/cm}^2$  were obtained on the first and second sweeps, respectively (Fig. 5.13a). The curves at high potentials, however, were noticeably more jagged compared to the amorphous carbons.

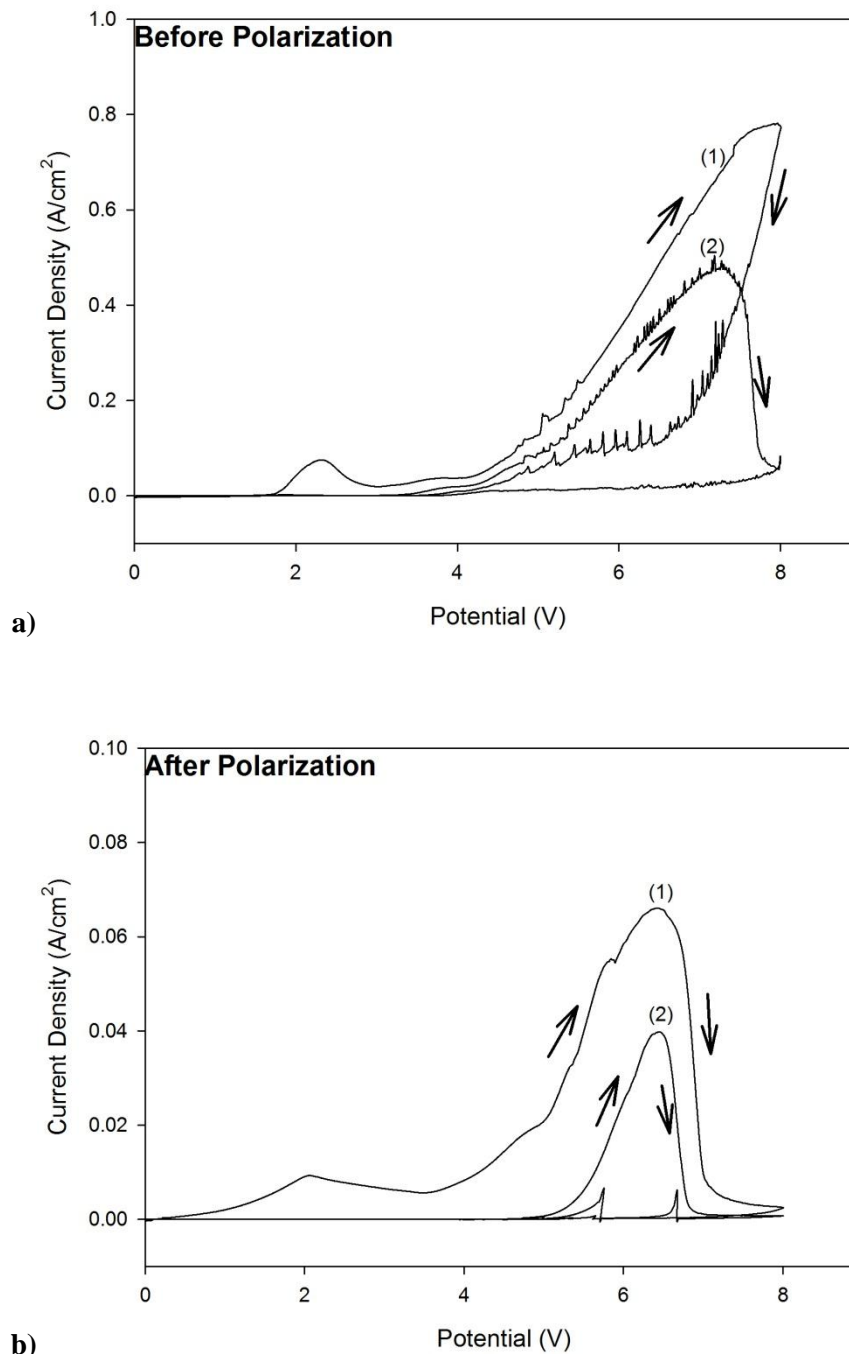
The voltammetric sweeps conducted after the short-term polarization series show the effect of passivation on the electrochemical responses of the different carbon materials over the potential range. The graphite rod achieved a peak current density of only  $0.065$  and  $0.040 \text{ A/cm}^2$  at 6.5 V on the first and second sweeps, respectively (Fig. 5.9b). Following this peak, the current dropped quickly to less than  $0.010 \text{ A/cm}^2$ , and the current did not recover even at 8.0 V. In particular, following the peak current in the second sweep, the electrode became deactivated, and the current decreased to less than  $0.0050 \text{ A/cm}^2$ . Following the polarization series, the peak current density on the Toyo Tanso carbon dropped by half from the values attained on the fresh electrode, while the

second sweep drops even further to  $0.10 \text{ A/cm}^2$  with the peak shifted to  $6.0 \text{ V}$  (Fig. 5.11b). The Cameco carbon, however, appeared to be largely unaffected by the polarization series, with the peak current density reaching  $\sim 0.55 \text{ A/cm}^2$  at  $8.0 \text{ V}$  on the both of the first two sweeps (Fig. 5.12b).

Finally, the vitreous carbon underwent the most significant change in terms of electrode passivation. The first sweep following polarization reached a peak current of only  $0.010 \text{ A/cm}^2$  at  $5.5 \text{ V}$ , which was in stark contrast to the  $1.1 \text{ A/cm}^2$  at  $8.0 \text{ V}$  on the fresh vitreous carbon surface (Fig. 5.13b). The peak current density on the second sweep of the vitreous carbon was larger than the peak current density on the first sweep ( $0.014$  vs.  $0.010 \text{ A/cm}^2$ , respectively) although the FDR appears to occur earlier on the first sweep than it does on the second ( $4.0$  vs.  $5.0 \text{ V}$ , respectively). After the peak current density is reached at  $\sim 5.5 \text{ V}$ , there is a rapid drop in current and inhibition of the FDR attributed to coverage of the surface by a gas film or bubble (Fig. 5.13b). There appeared to be a slight recovery in the current at higher potentials, although the currents were still limited at  $0.004 \text{ A/cm}^2$ . There is a slight decomposition of the surface layer on the reverse sweep as seen by the small current peak present again at  $\sim 5.5 \text{ V}$ .

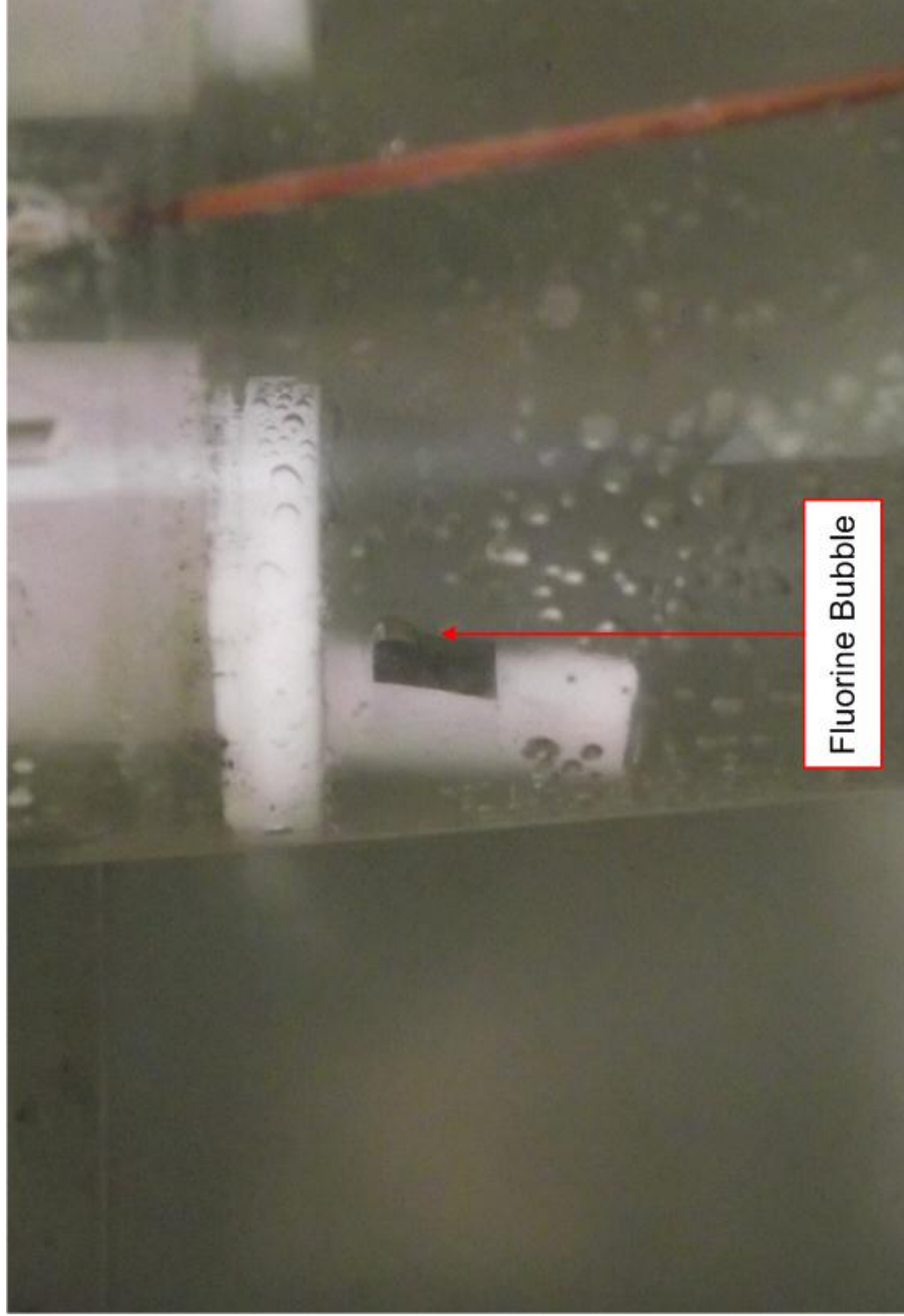
By looking at the change in peak current densities from the initial scans to the scans following the short-term polarizations, the effect and degree of passivation on each electrode is clear. The peak current density decreased by a factor of 10 on the graphite rod (from  $0.8$  to  $0.07 \text{ A/cm}^2$ , respectively), a factor of 100 on the vitreous carbon (from  $1.1$  to  $0.01 \text{ A/cm}^2$ ), but less than 50% on the industrial amorphous carbons.

**Fig. 5.9: Voltammograms of Graphite Rod Initially and After Fluorination**



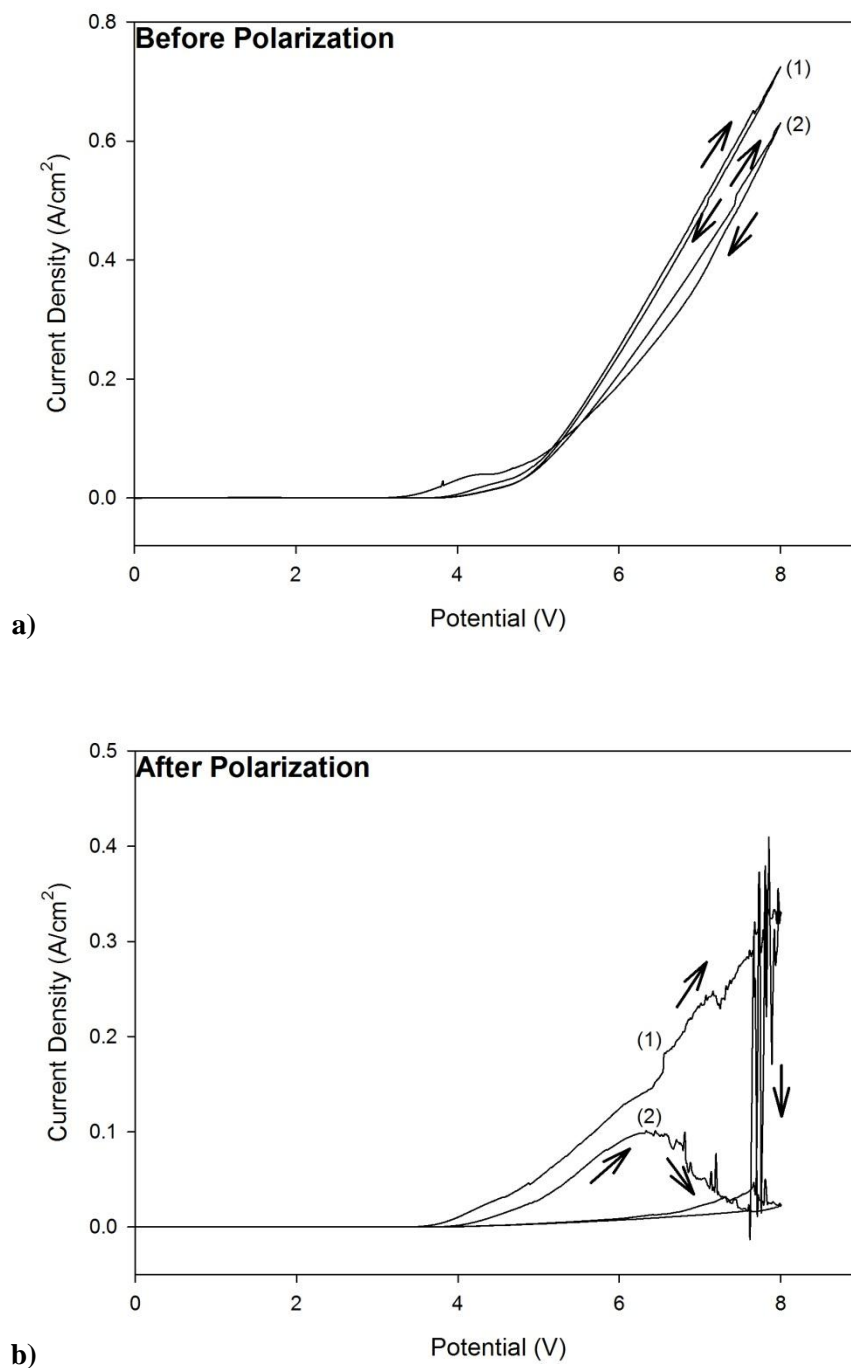
**a)** The first (1) and second (2) cyclic voltammetry scans of a vertical graphite rod electrode at 100 mV/s (a) before and (b) after short-term polarization series between 4.0 and 8.0 V. Arrows show forward and reverse sweeps.

**Fig. 5.10: Photograph of fluorine bubble on graphite rod**



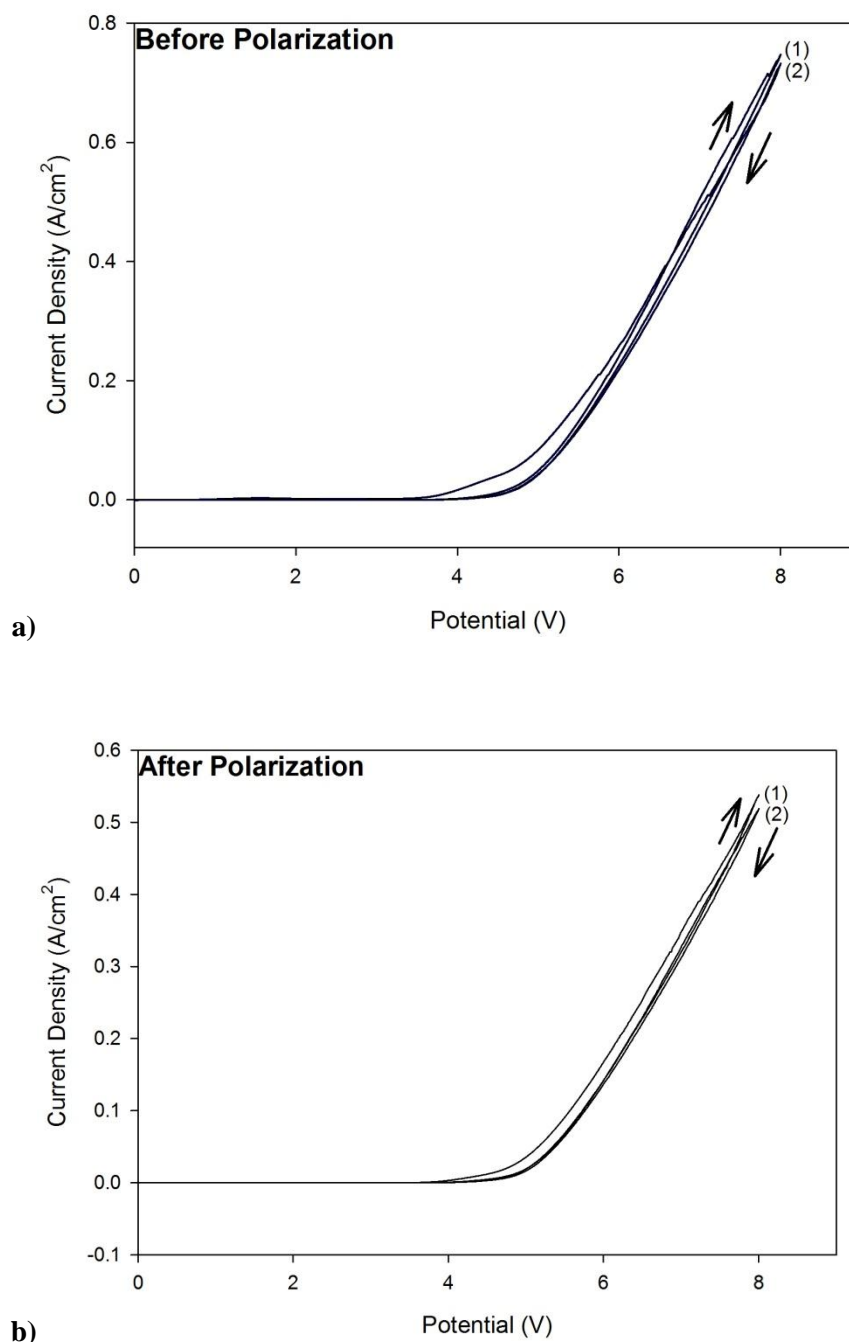
Photograph of fluorine bubble evolved on surface of a graphite rod polarized at 6.0 V in  $\text{KF}\cdot 2\text{HF}$ .

**Fig. 5.11: Voltammograms of Toyo Tanso Initially and After Fluorination**



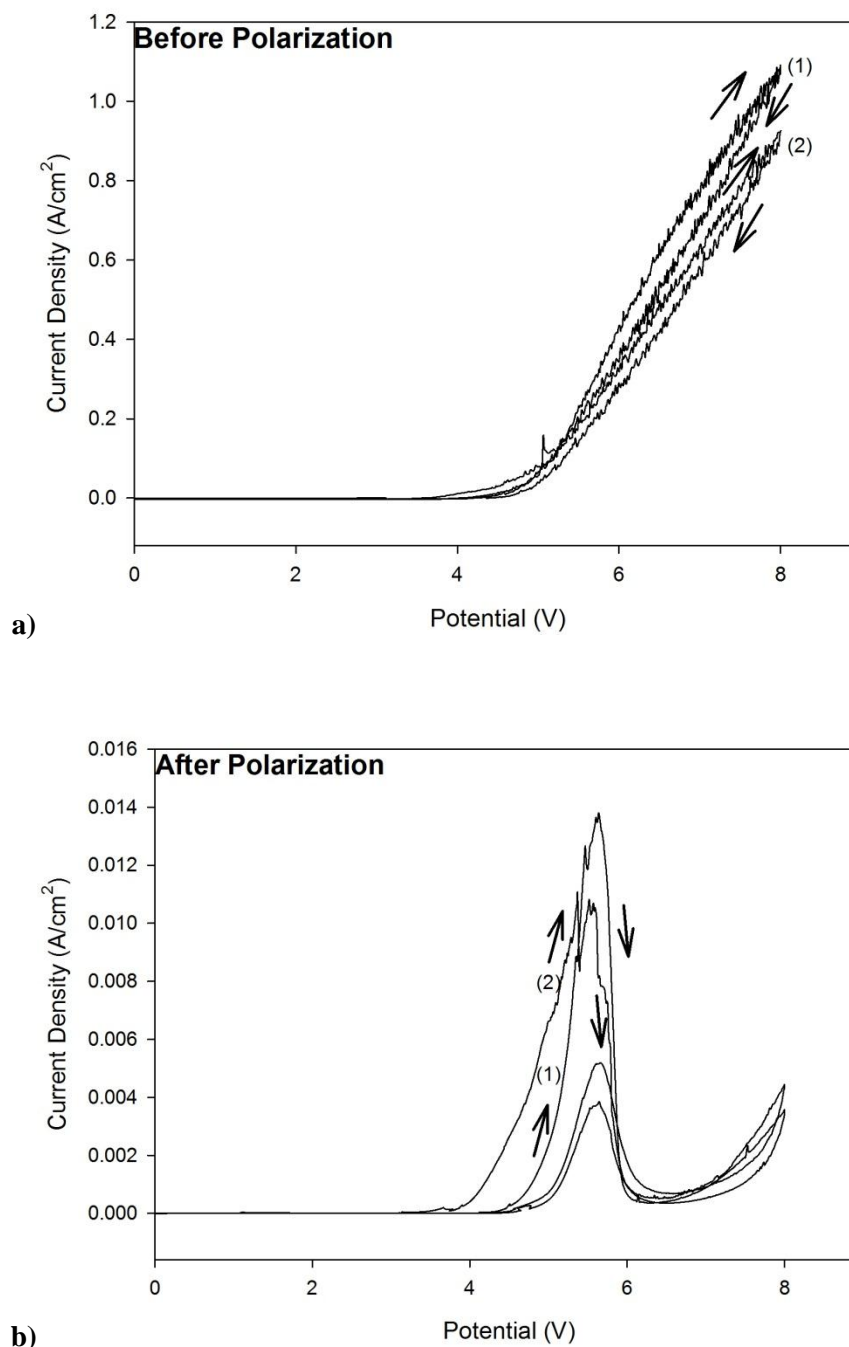
The first (1) and second (2) cyclic voltammetry scans of a vertical Toyo Tanso amorphous carbon electrode at 100 mV/s (a) before and (b) after short-term polarization series between 4.0 and 8.0 V. Arrows show forward and reverse sweeps.

**Fig. 5.12: Voltammograms of Cameco Amorphous Carbon Initially and After Fluorination**



**a)** The first (1) and second (2) cyclic voltammetry scans of a vertical Cameco amorphous carbon electrode at 100 mV/s (a) before and (b) after short-term polarization series between 4.0 and 8.0 V. Arrows show forward and reverse sweeps.

**Fig. 5.13: Voltammograms of Vitreous Carbon Initially and After Fluorination**



The first (1) and second (2) cyclic voltammetry scans of a vertical vitreous carbon electrode at 100 mV/s (a) before and (b) after short-term polarization series between 4.0 and 8.0 V. Arrows show forward and reverse sweeps.

## 5.2. Raman Spectroscopy Results

The Raman spectra of the initial, non-fluorinated carbon electrode materials shown in Figure 5.14 provide a measure of the degree of graphitization (or order) in each material. The characteristic peaks corresponding to the “ordered” and “disordered” C-C bond vibrational modes occur in the region of  $1580\text{ cm}^{-1}$  and  $1350\text{ cm}^{-1}$ , respectively. The peak intensity ratio,  $I_O/I_D$ , is a measure of the amount of order in a particular carbon material and is simply the ratio of intensities of the “ordered” to the “disordered” peak ( $I_O$  and  $I_D$ , respectively). The peak intensity ratios of the carbon starting materials are given in Table 5.1. Highly oriented pyrolytic graphite (HOPG) was selected as a reference material for graphitic carbons because it is considered to be the most ordered form of graphite. The  $I_O/I_D$  of the HOPG sample was 10.1. The polycrystalline graphite rod had an  $I_O/I_D$  of 3.6, whereas the carbon rod had an  $I_O/I_D$  of 3.7, indicating that the carbon and graphite rods were still highly crystalline compared to the Toyo Tanso and Cameco amorphous carbons ( $I_O/I_D$  of 1.3 and 1.1, respectively). Vitreous carbon, a completely non-graphitic carbon sample, had an  $I_O/I_D$  of only 0.69. The intensity peaks for the ordered and disordered C-C vibrational modes were present in their characteristic positions (wave numbers), even in the case of the broadened peaks of the amorphous carbons (Fig. 5.14, lines A to C).

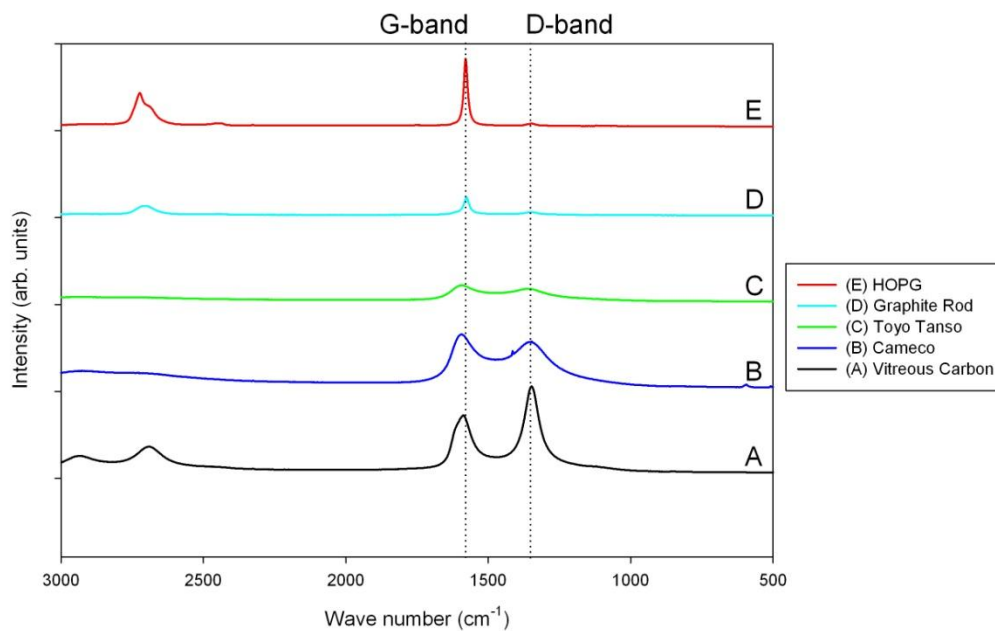
**Table 5.1: Initial Peak Intensity Ratios of Carbon Materials**

Carbon Material	Initial $I_O/I_D$
HOPG	10.1
Graphite Rod 1	3.6
Graphite Rod 2	4.5
Carbon Rod	3.7
Toyo Tanso	1.3
Cameco	1.1
Vitreous Carbon	0.69

Initial peak intensity ratios derived from Raman spectroscopy measurements of carbon electrode materials prior to fluorination.

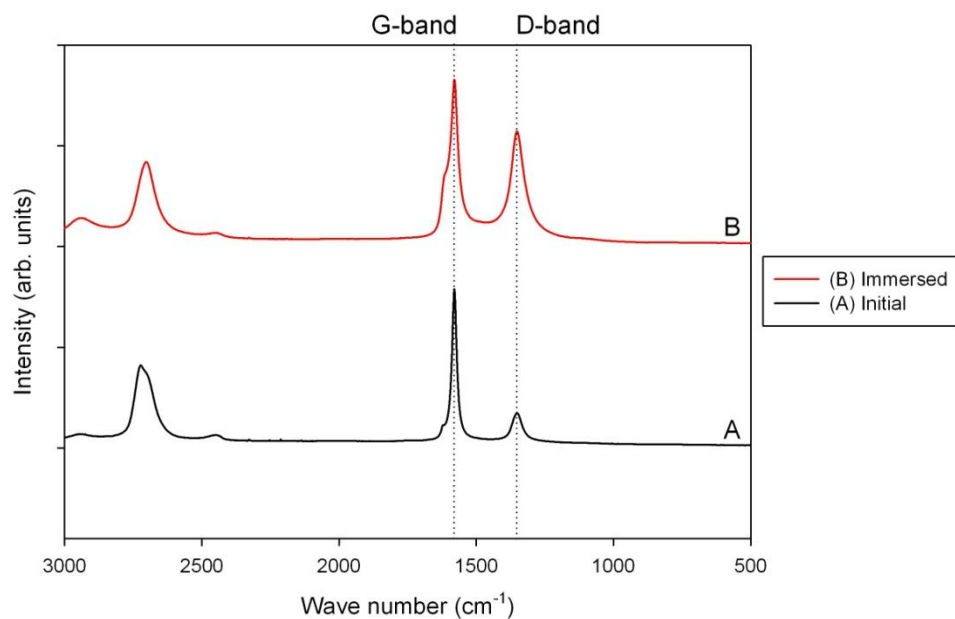
The Raman spectra of a graphite rod immersed into molten  $\text{KF}\cdot 2\text{HF}$  (Fig. 5.15) shows how susceptible the graphitic lattice is to intercalation of charged species, in the absence of an externally applied current. The  $I_O/I_D$  of the graphite rod decreased from 4.5 to 1.4, but there was no shift in the position of the peaks detected.

**Fig. 5.14: Raman Spectra of Non-Fluorinated Carbon Materials**



Raman spectra of non-fluorinated carbon anode materials. Where: (A) Vitreous Carbon, (B) Cameco, (C) Toyo Tanso, (D) Graphite Rod, (E) HOPG.

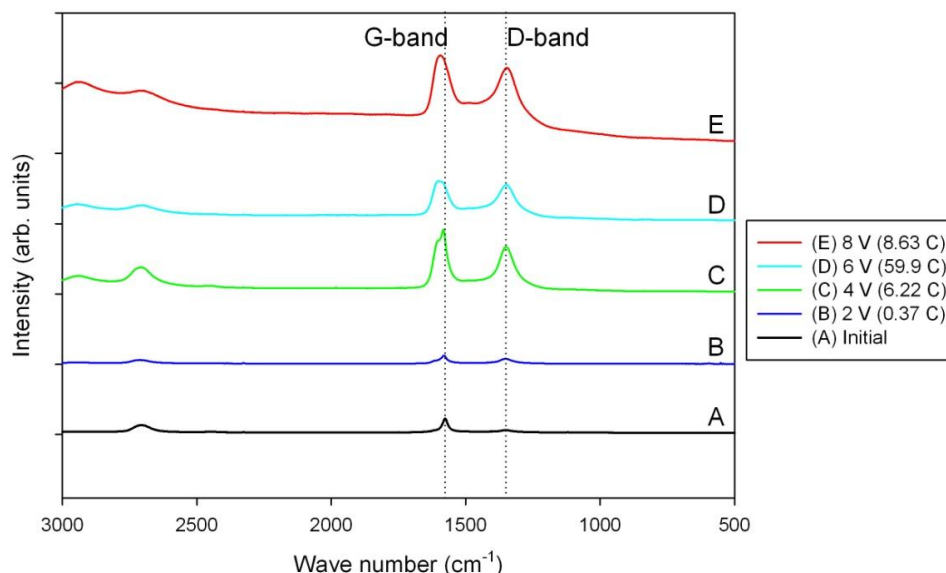
**Fig. 5.15: Raman Spectrum of Initial and Immersed Graphite Rod**



Raman spectra of a fresh graphite rod (A) and following immersion (B) in  $\text{KF}\cdot 2\text{HF}$  electrolyte for 30 minutes.

The Raman spectra of polarized graphite rods showing the effect of intercalation on the vibrational modes of the C-C bonds in the surface are shown in Figure 5.16. Results for the effect of the polarization potential on total charge passed, peak intensity ratios, and wave number shifts are given in Table 5.2. The graphite rod showed the highest degree of intercalation following polarization at 6.0 V based on the largest change in the  $I_{\text{O}}/I_{\text{D}}$  from 3.5 down to 1.1. A shift in the position of the ordered and disordered peaks (+21.4 and  $-1.1 \text{ cm}^{-1}$ , respectively) occurs as a result of C-C bond lengthening (lower energy vibrations). The second largest wavenumber shift occurred following polarization at 8.0 V, while the graphite polarized at 2.0 and 4.0 V showed only a minor shift.

**Fig. 5.16: Raman Spectrum of Graphite Rod Following Polarizations**



Raman spectra showing non-fluorinated graphite rod (A), as well as graphite rods fluorinated for 30 minutes at 2.0 V (B), 4.0 V (C), 6.0 V (D), and 8.0 V (E).

The Raman spectra of the fluorinated industrial amorphous carbons (Toyo Tanso and Cameco) were largely unchanged, indicating that the materials were unaffected by intercalation during the FDR (Fig. 5.17 and 5.18). There was no appreciable change in the  $I_{\text{O}}/I_{\text{D}}$  ratio at any of the potentials tested, remaining at  $\sim 1.1$  on both carbons (Table 5.2). In addition, there was no discernable trend for the shift in wavenumber of the ordered and disordered peak intensity positions. Based on these results, intercalation does not appear to be occurring on the industrial amorphous carbon samples.

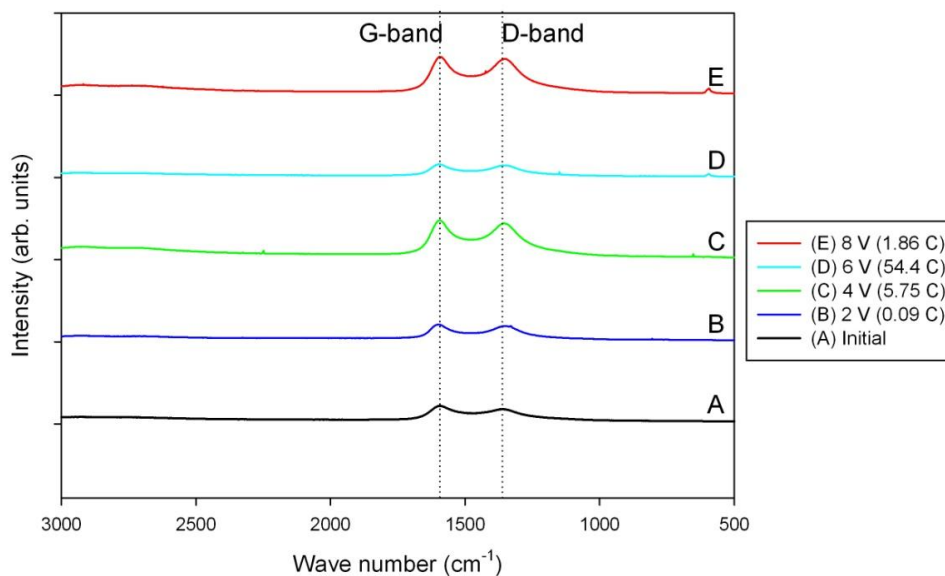
**Table 5.2: Summary of Peak Intensity Ratios and Shifts Following Polarization**

Potential (V)	Charge (C)	“Graphitic” Peak Intensity	Wavenumber (cm <sup>-1</sup> )	“Disordered” Peak Intensity	Wavenumber (cm <sup>-1</sup> )	Baseline Intensity	Peak Ratio (Graphitic: Disordered)	Wavenumber Shift “Graphitic”	Wavenumber Shift “Disordered”
<b>Graphite Rod</b>									
Initial	0	199721	1577.4	57829	1348.7	3167	3.60	0	0
2.0	0.374	12484	1581.0	7895.9	1352.0	1084	1.67	+ 3.6	+ 3.3
4.0	6.22	91598	1582.5	67074	1350.6	8363	1.42	+ 5.1	+ 1.9
6.0	59.9	60748	1598.8	55432	1347.6	12247	1.12	+ 21.4	- 1.1
8.0	8.63	139392	1595.8	121882	1347.6	56470	1.27	+ 18.4	- 1.1
<b>Toyo Tanso</b>									
Initial	0	22182	1595.2	18115	1356.5	5475	1.32	0	0
2.0	0.0893	21222	1600.3	19305	1352.0	4654	1.13	+ 5.1	- 4.6
4.0	5.75	48002	1595.8	44852	1356.5	7086	1.08	+ 0.6	0
6.0	54.4	16154	1595.8	14905	1355.0	2734	1.10	+ 0.6	- 1.5
8.0	1.86	46891	1595.8	44357	1350.6	4834	1.06	+ 0.6	- 1.9
<b>Cameco</b>									
Initial	0	65807	1594.4	57580	1347.6	10559	1.17	0	0
2.0	0.251	41213	1594.4	36902	1353.5	6172	1.14	0	+ 5.9
4.0	1.36	56779	1592.9	51601	1352.0	6346	1.11	- 1.5	+ 4.4
6.0	184	74547	1592.9	67701	1349.1	11405	1.12	- 1.5	+ 1.5
8.0	3.02	59533	1598.8	53464	1346.1	10182	1.14	+ 4.4	- 1.5

Summary of Raman spectra of fluorinated carbon anode materials showing change in graphite/disordered peak-intensity-ratio with electrochemical fluorination.

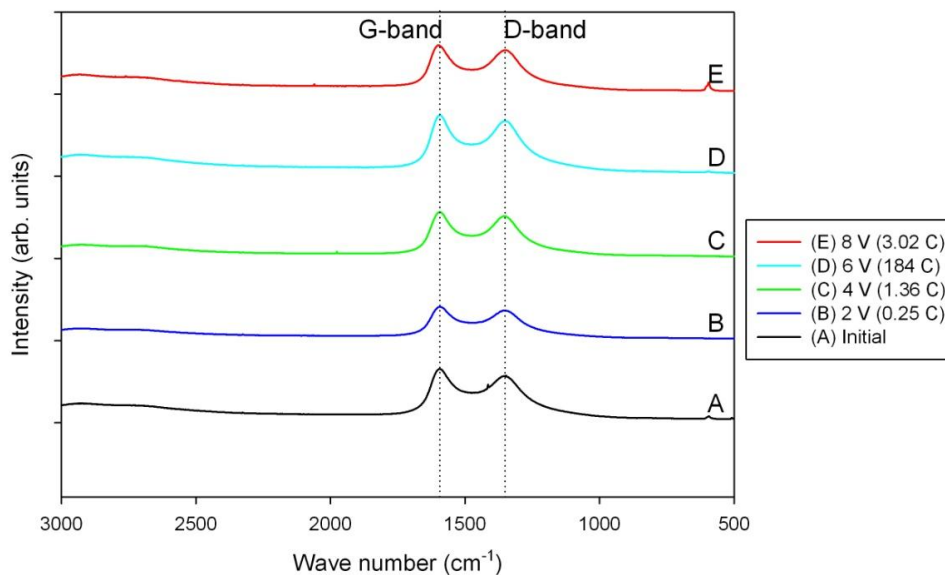
The corrections applied to the intensity values in the Raman spectrum for the carbon samples (to account for the signal-to-noise ratio) were between 1 to 5% (Table 5.2).

**Fig. 5.17: Raman Spectrum of Toyo Tanso Amorphous Carbon Following Polarizations**



Raman spectra showing non-fluorinated Toyo Tanso amorphous carbon (A), and fluorinated for 30 minutes at 2.0 V (B), 4.0 V (C), 6.0 V (D), and 8.0 V (E).

**Fig. 5.18: Raman Spectrum of Cameco Amorphous Carbon Following Polarizations**



Raman spectra showing non-fluorinated Cameco amorphous carbon (A), and fluorinated for 30 minutes at 2.0 V (B), 4.0 V (C), 6.0 V (D), and 8.0 V (E).

## 5.3. Electrochemical Impedance Spectroscopy (EIS)

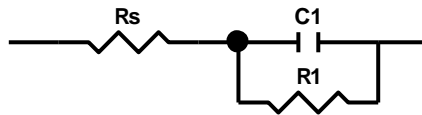
### 5.3.1. CF<sub>x</sub> Film Thicknesses

AC Impedance results for the C/KF·2HF interface on carbon electrodes were obtained between polarization experiments. Calculated thickness values for the CF<sub>x</sub> surface layer were based on the simplified circuit model shown in Table 3.1 over the frequency range of 10<sup>5</sup> to 10<sup>4</sup> Hz. The thicknesses were calculated using Eq. (17) and are given in Table 5.3. The capacitance values on each of the ‘initial’ samples represent the solution double-layer only, since the electrodes had not been polarized and so no passive film had formed (or the CF<sub>x</sub> film was sufficiently thin that it did not contribute to the overall measurement). The graphite and carbon rod had CF<sub>x</sub> film thickness values that increased as the electrodes were polarized at progressively higher potentials. The calculated thickness of the CF<sub>x</sub> layer on the graphite rod increased from 0.13 to 7.4 nm, while the layer on the carbon rod increased from 0.13 to 2.2 nm. The industrial amorphous carbons (Toyo Tanso and Cameco) had capacitance values that were consistently low (~0.02 to 0.1 μF/cm<sup>2</sup>) over the potentials tested. The capacitance values of the amorphous carbons were one order of magnitude lower than those of the graphitic carbons. The calculated thickness values for the CF<sub>x</sub> layer on the amorphous carbons following the polarization series were 28 and 151 nm on the Toyo Tanso and Cameco carbons, respectively. The thickness values were one to two orders of magnitude larger than those on the graphitic carbons. Finally, the calculated film thickness on vitreous carbon following polarization at 4.0 V was already 4 nm, and increased to 19 nm after the polarization at 8.0 V. A full table of fitted data including solution resistances and CF<sub>x</sub> passivated layer resistances is provided in Appendix 3. Following polarization experiments, there was no visible change in the surface of the carbons (for example, colour or roughness) that could be clearly attributed to CF<sub>x</sub> film formation.

The measured solution resistance (R<sub>s</sub>) values obtained on the fresh electrode surfaces were ~4 Ω (Table 5.3).

On each carbon, there was little change in the measured capacitance value between the ‘initial’ carbons and the carbons which had been polarized to 4.0 V. There was, however, a much more significant change following polarization at 5.0 V. The capacitance

**Table 5.3: Measured Capacitance Values and Calculated CF<sub>x</sub> Layer Thickness**



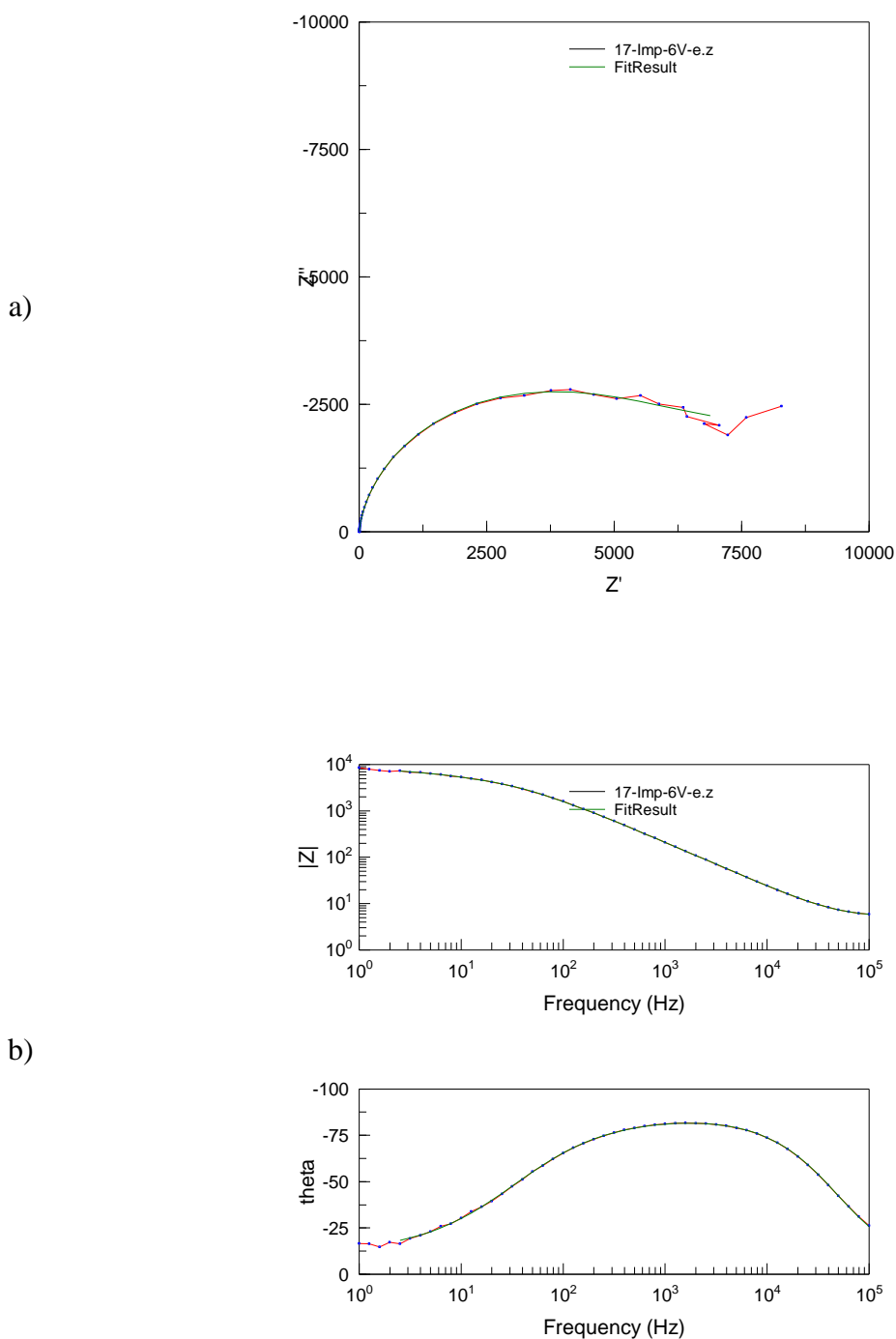
Carbon Sample	Polarization Potential (V)	Capacitance ( $\mu\text{F}/\text{cm}^2$ )	Thickness (nm)	$\chi^2$
Graphite Rod	Initial	16	0.13	$3.76 \times 10^{-3}$
	4.0	13	0.15	$1.74 \times 10^{-3}$
	5.0	1.7	1.18	$1.08 \times 10^{-2}$
	6.0	0.34	6.07	$1.13 \times 10^{-3}$
	7.0	1.5	1.41	$1.09 \times 10^{-2}$
	8.0	0.28	7.39	$2.06 \times 10^{-4}$
Carbon Rod	Initial	16	0.13	$8.42 \times 10^{-3}$
	4.0	13	0.15	$1.01 \times 10^{-3}$
	5.0	0.44	4.74	$3.05 \times 10^{-2}$
	6.0	1.4	1.52	$1.78 \times 10^{-2}$
	7.0	1.5	1.38	$9.30 \times 10^{-3}$
	8.0	0.94	2.18	$1.46 \times 10^{-2}$
Toyo Tanso Amorphous Carbon	Initial	29	0.08	$2.93 \times 10^{-4}$
	4.0	23	0.10	$8.30 \times 10^{-4}$
	5.0	0.09	24.4	$8.39 \times 10^{-3}$
	6.0	8.1	0.28	$1.30 \times 10^{-3}$
	7.0	0.06	37.8	$4.16 \times 10^{-3}$
	8.0	0.08	28.3	$1.86 \times 10^{-3}$
Cameco Amorphous Carbon	Initial	17	0.13	$7.12 \times 10^{-4}$
	4.0	11	0.20	$1.55 \times 10^{-3}$
	5.0	0.11	21.0	$9.43 \times 10^{-3}$
	6.0	0.03	69.7	$3.01 \times 10^{-3}$
	7.0	0.02	101	$1.83 \times 10^{-2}$
	8.0	0.02	151	$5.99 \times 10^{-2}$
Vitreous Carbon	Initial	2.81	0.66	$5.86 \times 10^{-4}$
	4.0	0.48	3.84	$1.16 \times 10^{-3}$
	5.0	0.42	4.40	$2.14 \times 10^{-4}$
	6.0	2.04	0.91	$1.43 \times 10^{-2}$
	7.0	0.11	17.0	$7.24 \times 10^{-2}$
	8.0	0.10	19.4	$7.34 \times 10^{-3}$

Capacitance and double-layer thickness values calculated from impedance data measured following polarization experiments. Data was fitted to a simple RC circuit over the frequency range  $10^5$  to  $10^4$  Hz with 100 optimization iterations applied to the fitted values.

decreased by two orders of magnitude indicating that  $\text{CF}_x$  film formation had occurred and progressed much more at 5.0 V than it had at 4.0 V. All of the values presented in Table 5.3 have  $\chi^2$  values that indicate a high goodness-of-fit (a low  $\chi^2$  value) for each of the circuit fittings conducted.

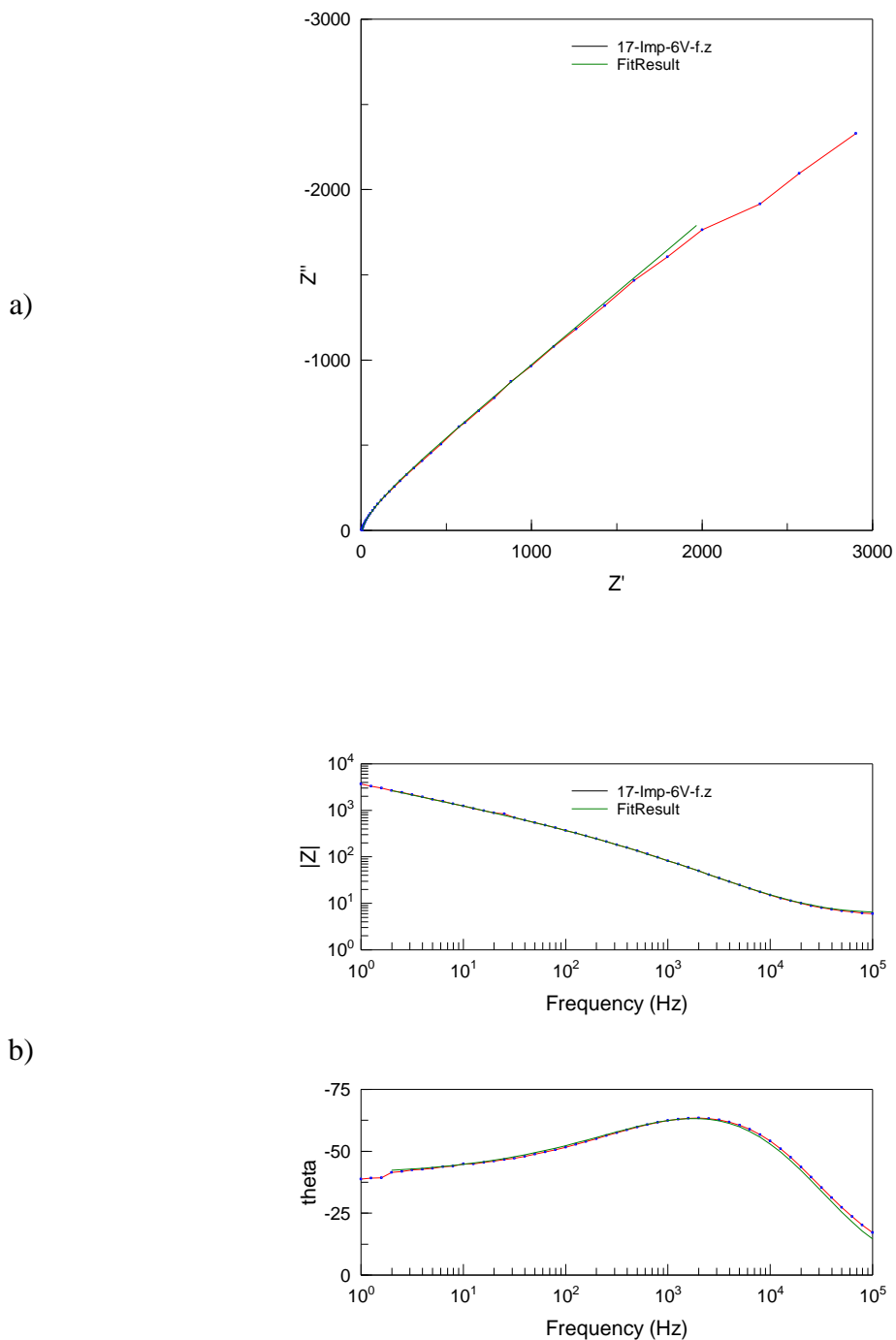
Deviations in the calculated film thickness values presented in Table 5.3 may be caused by a time-dependence of the EIS measurement following the end of the polarization experiment. Substantially larger capacitance values for the graphite rod following polarization at 7.0 V and the Toyo Tanso carbon following polarization at 6.0 V were obtained compared to the C1 values at higher and lower potentials for each of the samples tested. The C1 values for the impedance measurements taken 2340 s and 2640 s after the polarization at 6.0 V, are 0.667 and 0.945  $\mu\text{F}/\text{cm}^2$  based on the circuit model shown in region A and B of Fig. 3.3. These capacitances correspond to film thicknesses of 3.1 nm and 2.2 nm, respectively. The Nyquist plots of the two EIS experiments (Fig. 5.19a and 5.20a) show dramatically different impedance results. The Bode plots have similar curves, reaching a peak in the  $\theta$  value around 1000 Hz, before gradually decreasing towards lower frequencies (Fig. 5.19b and 5.20b). As more time passed from the end of the polarization experiment, there was an increase in the C1 value and an appreciable decrease in the R1 and R2 values. The measured increase in film capacitance results in a decrease in the calculated film thickness.

**Fig. 5.19: Nyquist and Bode Plots for Graphite Rod Polarized at 6 V After 2340 s**



Nyquist (a) and Bode (b) plots for graphite rod polarized at 6.0 V, based on impedance results that were obtained 2340 seconds after the end of the polarization period, showing effect of time-delay on impedance.

**Fig. 5.20: Nyquist and Bode Plots for Graphite Rod Polarized at 6 V After 2640 s**



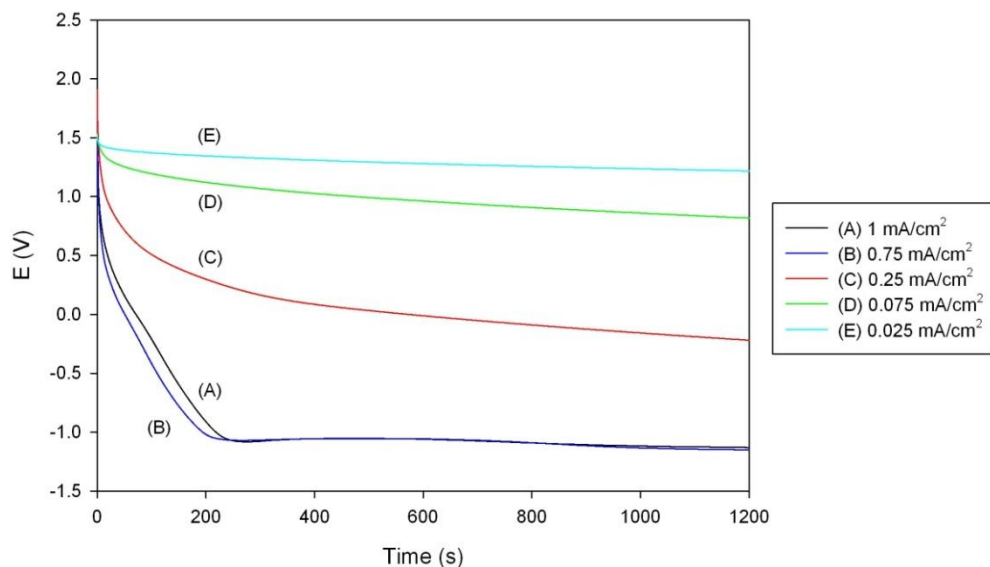
Nyquist (a) and Bode (b) plots for graphite rod polarized at 6.0 V, based on impedance results that were obtained 2640 seconds after the end of the polarization period, showing effect of time-delay on impedance

## 5.4. Galvanostatic Discharge Experiments

The galvanostatic discharge curves of electrochemically fluorinated graphite rods are shown in Figure 5.21. The graphite rods were polarized at 6.0 V for a total charge density of 50 C/cm<sup>2</sup> per electrode. Current densities were applied to the fluorinated samples to maintain a steady rate of fluorine discharge, and the discharge potential was monitored. All of the graphite rods tested under these conditions had a discharge potential of approximately 1.8 V (vs. Ag/AgI). At current densities of 1.0 and 0.75 mA/cm<sup>2</sup>, the discharge potential decreased rapidly from approximately 1.9 V for both samples, reaching a potential minimum of -1.1 V. This potential was believed to correspond to electrolytic decomposition of the propylene carbonate (PC) cell electrolyte, as well as depletion of the intercalated fluorine. The potential reached a steady state of ~-1.1 V for the remainder of the experiment indicating that the species being reduced (PC) was present in high concentrations. The decomposition potential of PC was reported to be 1.0 V (vs. Li/LiClO<sub>4</sub>) in the literature [74]. Current densities of 0.075 and 0.025 mA/cm<sup>2</sup> appeared to be too low for the electrodes to become depleted, and an estimated amount of intercalated fluorine in the sample could not be obtained. An applied current density of 0.25 mA/cm<sup>2</sup> yielded a (relatively) steady potential of ~0 V after 300 seconds from the start of the experiment, and may be a suitable current density for longer discharge studies.

An inflection point was observed on the two curves at the high discharge currents (lines A and B, Fig. 5.21) around 90 s, which suggested that a change in the primary reduction reaction had occurred. Using this inflection point as the depletion of F atoms, the total charge passed up to this point was calculated and assumed to represent the amount of intercalated fluorine. This value was used to estimate what the fraction of the total charge applied (to fluorinate the samples) was involved with fluorine intercalation. On the two depleted samples (at current densities of 1.0 and 0.75 mA/cm<sup>2</sup>), the time at which both samples were considered to be depleted was 100 and 85 s, respectively (Fig. 5.21, lines A and B). The amount of intercalated fluorine was estimated by the average of the product of the applied current density and time, for the two samples. The averaged value

**Fig. 5.21: Fluorine Discharge from Graphite at Various Current Densities**



Galvanostatic discharge of fluorine ions electrochemically intercalated into the graphite in PC-LiClO<sub>4</sub> at current densities of: (A) 1 mA/cm<sup>2</sup>, (B) 0.75 mA/cm<sup>2</sup>, (C) 0.25 mA/cm<sup>2</sup>, (D) 0.075 mA/cm<sup>2</sup>, and (E) 0.025 mA/cm<sup>2</sup>. Fluorinated graphite rod was polarization at 6.0 V in KF·2HF at 90 °C for a charge density of 50 C/cm<sup>2</sup>.

of the charge for intercalated fluorine was then divided by the total charge density applied during the fluorination step (50 C/cm<sup>2</sup>). Based on the calculation, intercalation was estimated to account for 0.16% of the total charge passed during the polarization step. This fraction was then multiplied by the surface areas for the individual electrodes at the other three current densities. The estimated amount of intercalated fluorine and discharge times are shown in columns 4 and 5 in Table 5.4. The predicted discharge times indicate that while the depletion of intercalated fluorine at current densities of 0.25 and 0.075 mA/cm<sup>2</sup> could occur within the time scale used in Figure 5.21, the galvanostatic results did not fully agree. A current density of 0.025 mA/cm<sup>2</sup>, however, would be too low to completely discharge the intercalated fluorine atoms within the time scale of the experiment.

A Tafel plot created from the galvanostatic experiments was based on potential values at 50 s from the start of the experiment under different current densities. The Tafel plot is

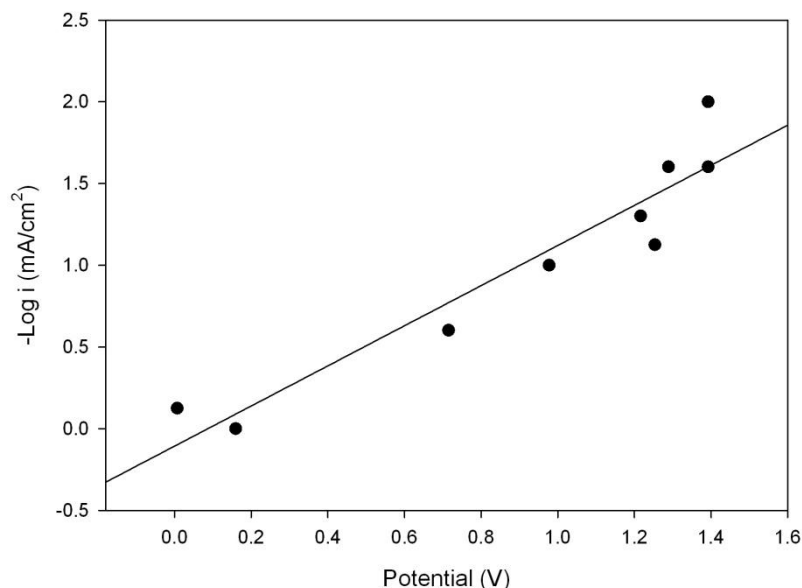
shown in Figure 5.22. The Tafel slope was calculated to be 0.81 V/decade. The  $R^2$  value for the set of data was 0.901, which reflects a relatively good fit (a value close to 1) of the data against the regression.

**Table 5.4: Calculated Amount of Intercalated Fluorine and Discharge Times**

Current Density (mA/cm <sup>2</sup> )	Surface Area (cm <sup>2</sup> )	Normalized Charge (C)	Estimated Amount Intercalated (C)	Predicted Discharge Time (s)
1	0.638	31.9	0.064	100
0.75	0.675	33.8	0.043	85
0.25	0.630	31.5	0.051	330
0.075	0.595	29.8	0.049	1100
0.025	0.720	36.0	0.059	3500

Calculated discharge times for intercalated fluorine content estimated to be 0.163% of total applied charge (50 C/cm<sup>2</sup>) as a function of applied current density.

**Fig. 5.22: Tafel Plot for Discharge of Fluorine Ions**

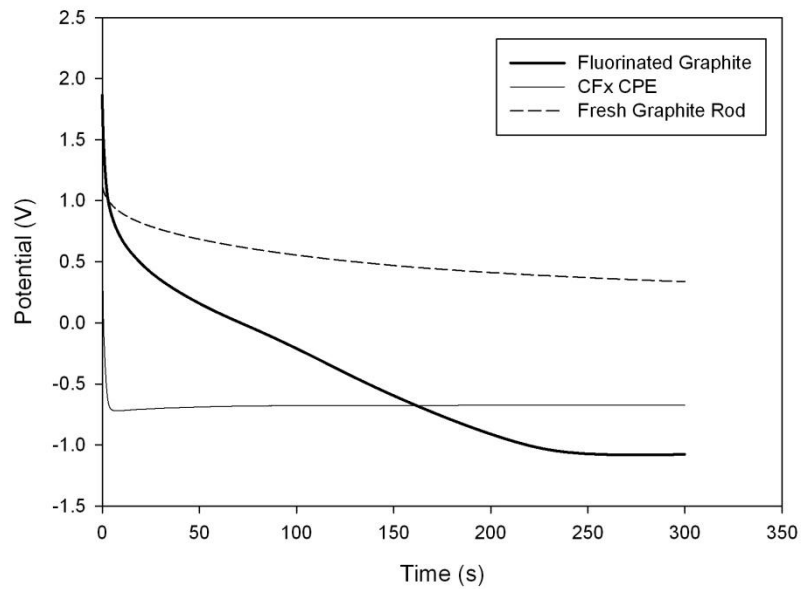


Tafel plot of de-intercalation of fluorine ions from graphitic lattice in PC-LiClO<sub>4</sub> taken from potentials after 50 s from the start of the galvanostatic experiment.

A comparison of electrochemically fluorinated graphite, chemically fluorinated CF<sub>x</sub> carbon paste electrode, and a fresh graphite electrode is shown in Figure 5.23. The initial potentials for the three carbon materials were 1.8, 0.6, and 1.1 V, respectively. The fluorinated graphite rod had a gradual potential decay over the duration of the experiment, whereas the CF<sub>x</sub> had an abrupt drop in the measured potential down to -0.7 V within 10 s of the start of the experiment (Fig. 5.23) and remained steady for the

remainder of the experiment. The fresh graphite attained a steady state discharge potential of 0.5 V (which does not represent fluorine discharge).

**Fig. 5.23: Discharge Curves for  $\text{CF}_x$  CPE vs. Fluorinated and Fresh Graphite Rods**



Galvanostatic discharge curves for chemically fluorinated graphite fluoride,  $\text{CF}_x$ , (2:1, graphite powder: $\text{CF}_x$ ) as a carbon paste electrode in PC- $\text{LiClO}_4$  at a current density of  $1 \text{ mA/cm}^2$ .

## 6. Discussion

### 6.1. Polarization Experiments

#### 6.1.1. Sustainable Rate of Reaction

A steady state current ( $I_{ss}$ ) is the result of a limitation of charge ( $e^-$ ) or mass transport to the surface of the electrode, representing a kinetic or diffusion limited process. This limited transport may be due to a capacitive layer or a physical barrier on the surface of an electrode that impedes the movement of electroactive species in the system. The thickness of the capacitive layer depends on the chemistry at the surface of the electrode and, in particular, the passivated layer in a reactive environment.

The decrease in  $I_{ss}$  at potentials above 5.0 V on the graphite rod suggests that the surface was progressively more passivated as the potential became more positive, and the FDR became inhibited by the presence of a gas film or bubble on the electrode. It was likely that a relatively thick passivating layer was formed on the electrode by 8.0 V, as indicated by the low  $I_{ss}$  towards the end of the polarization series. Santhanam [73] reported that the passivated-graphite model carbons, graphite-20% and 35%PTFE, performed very differently from the graphite electrodes following polarization at 4.0 V (Fig. 5.6). The graphite-20%PTFE sample displayed relatively low  $I_{ss}$  values ( $\sim 5 \text{ mA/cm}^2$ ) over the potentials tested, whereas the graphite-35%PTFE sample had a high  $I_{ss}$  at 5.0 V ( $\sim 40 \text{ mA/cm}^2$ ), that decreased gradually at higher potentials (Fig. 5.6). The low  $I_{ss}$  values indicate that the FDR was slower on the 20%PTFE sample, while the “more passivated” 35%PTFE sample performed better than the plain graphite rod itself. Thus, the PTFE content in the graphite samples did not appear to have a repelling (or, passivating) effect on the electrolyte since relatively high  $I_{ss}$  values were obtained. Further alternative techniques (such as XPS or EDX) would be required to determine the distribution of  $\text{CF}_x$  regions on the surface of the electrode, and its relation to the position of PTFE particles. This will determine if the PTFE particles effectively repel the electrolyte and limit the FDR at the surface of the electrode.

The amorphous carbons were able to maintain high currents even during polarizations at high potentials ( $>6.0 \text{ V}$ ), which suggested that they were generally resistant to passivation

at lower potentials (4.0 V). The characterization TGA results indicated that up to 7% of the initial sample mass was composed of a volatile organic material, which was likely a coal-tar pitch binder used during the manufacture of amorphous carbons. The results of the potentiostatic series were consistent with the findings by Root et al. [51], that coal-tar pitch binder material was resistant to chemical fluorination, and that the presence of coal-tar pitch at the surface of the amorphous carbons may have minimized fluorination (and, passivation). Santhanam's work [73] on model Vulcan-PTFE carbons show that even 20%-PTFE is enough to deactivate a carbon electrode (Fig. 5.6). The significant decrease in  $I_{ss}$  at 8.0 V may suggest the formation of a persistent gas film or bubble that limits the electrolyte from reaching the surface. This may be particularly true if bubbles filled the pores of the Cameco carbon and acted as a nucleation point for a surface-covering gas film. Overall, the rates of fluorine generation on the amorphous carbons were significantly higher than those obtained on the graphitic samples.

The consistently low rate of reaction on the vitreous carbon following polarization at 5.0 V suggests that the electrode was passivated quickly, inhibiting the FDR at even higher potentials. In addition, the smooth surface of the vitreous carbon meant that the actual (active) surface area was very close to the geometric surface area, which was lower than the rough (and likely, porous) surface of amorphous carbons, resulting in a lower  $I_{ss}$ . The coverage of the surface by a gas film or bubble had a more detrimental effect on the passing of current, especially on a passivated layer that had formed early in the polarization series.

Vulcan-PTFE samples also produced by Santhanam [73] were reported to have  $I_{ss}$  values that increased with increasing potentials even up to 8.0 V (secondary axis on Fig. 5.6); however, the currents were up to 2 orders of magnitude smaller than those obtained on the other carbons. At 8.0 V, PTFE-containing Vulcan carbon samples had maximum  $I_{ss}$  of only 0.2 and 0.1 mA/cm<sup>2</sup> for the 20%- and 35%-PTFE samples, respectively. In comparison, the  $I_{ss}$  decreased with increasing potentials for the graphite-PTFE samples [73] (Fig. 5.6). The industrial amorphous carbons behaved similarl to the Vulcan carbons and showed an upward trend in  $I_{ss}$  values; however, the PTFE may be responsible for  $I_{ss}$  values that were more than 100 times lower on the Vulcan carbons than those on the Toyo Tanso or Cameco carbons.

Overall, the industrial amorphous carbons were able to maintain the FDR at a high rate even during polarizations at higher potentials which, in the case of the graphitic carbons, were greatly inhibited. The graphitic carbons were passivated at lower potentials, which slowed the FDR, while the amorphous carbons were not affected by electrode deactivating processes until 8.0 V. Vitreous carbon behaved like the graphitic carbons and became deactivated after the polarization at 5.0 V. Results from the PTFE “passivated” carbon by Santhanam [73] were not directly comparable to the fluorinated carbon materials, since the graphite-PTFE performed better than the graphite rod while the Vulcan-PTFE was worse than vitreous carbon.

### **6.1.2. Electrode Effectiveness for Fluorine Generation**

There is a close relationship between the susceptibility of electrode passivation and the low rate of FDR for a carbon anode material. The graphitic carbon rods were passivated after small amounts of charge were passed between 4.0 and 5.0 V, which resulted in low quantities of charge during subsequent polarizations from 6.0 to 8.0 V. The passivation of the carbon and graphite rods may be due to the high activity of the edge planes of the graphite lattice, especially on a sample of polycrystalline graphite [12,75]. Since both samples were considered to be graphitized rods, it was expected that there would not be a significant difference in the conductivity of the carbon and graphite rod which would lead to more charge being passed in one sample over the other. As previously stated, however, a higher quantity of coal-tar pitch in the carbon rod could explain the higher effectiveness of the carbon rod over the graphite rod. In comparison, the industrial amorphous carbons were much more effective for fluorine evolution, and large charges were passed even during polarizations up to 7.0 V. While the Toyo Tanso had a relatively smooth, continuous surface, the Cameco carbon had visible surface roughness with pores up to 0.5 mm in diameter. The peaks on the surface of the electrode may have promoted bubble detachment at lower potentials. Passivation of the surface and bubbles trapped in pores of the electrode may have supported the formation of an insulating gas film. Whereas the Cameco carbon had become deactivated at 8.0 V, the smoother surface of the Toyo Tanso carbon allowed the FDR to continue effectively at the same potential.

Since graphitization was the primary difference between the carbon samples, intercalation of fluorine atoms was expected to occur in the graphitic samples, but not the amorphous carbons. The deleterious effects of covalently-bonded intercalated fluorine would generally be avoided on the non-graphitized carbons. It is expected that the amorphous carbon samples would contain small crystals of graphite due to the inherent characteristics of the precursors; however, it is not known whether fluorine intercalation has any appreciable effect on the characteristics of these materials. Vitreous carbon was the least effective for the FDR, since very little charge was passed for polarization above 5.0 V. Although vitreous carbon might be a reference material for a purely non-graphitic amorphous carbon, its electrochemical properties were unlike those of the two industrial amorphous carbons. These variations may be attributed to the degree of surface roughness, or the absence of impurities present in the sample (as indicated by TGA results during characterization).

The graphitic carbons samples were more passivated than the amorphous carbons even though significantly less charge was passed (on the graphite and carbon rods). Passivation of the graphitic carbons after a lower amount of charge meant that there was an overall loss in the FDR for all subsequent polarizations, making the graphitic carbons, overall, ineffective for fluorine generation.

### **6.1.3. Electrode Passivation**

Electrode passivation was evident even during initial cyclic voltammetry (CV) sweeps of some of the carbon materials (Fig. 5.9a). The decrease in peak current density between the first and second sweeps on the graphite rod suggested the formation of a thin  $\text{CF}_x$  layer. The subsequent generation of a gas film or bubble on the second sweep could explain the sudden drop in current at 7.5 V (Fig. 5.9a). The rate of the FDR is inhibited by concentration-control due to the presence of this barrier, particularly when it is formed during a potential sweep. The appearance of a smooth curve on the first sweep suggests the rapid detachment of evolved gas bubbles, whereas the rough curve on the second sweep corresponds to the rapid growth and detachment of larger, surface-covering bubbles, which had a greater effect on the current (reaction rate) (Fig. 5.9a).

The CV curves of the amorphous carbons show a near-perfect trace of the reverse sweeps

as on the forward sweeps (Fig. 5.10 and 5.11), indicating that the reactions were electrochemically reversible. These results suggest that amorphous carbons were not easily passivated even at high potentials. Similar to the initial graphite sweeps (Fig. 5.9a) the smooth curves at high currents were consistent with the formation of small fluorine bubbles that easily detach from the surface. The linear shape of the voltammetric curves at high potentials on the amorphous carbons (Fig. 5.10 and 5.11) were indicative of ohmic resistance in the electrochemical system. This is caused by solution resistance. The effect known as ohmic resistance is observed when the resistance of the electrolyte is sufficiently large that it becomes the current-limiting factor in a voltammogram, rather than the charge-transfer resistance or mass transport limitation. Thus, if the electrode is still highly conductive, the electrochemical response of the system follows Ohm's law, which is a linear relationship. The ohmic resistance-limited region of the voltammograms was used to estimate the resistance of molten  $\text{KF}\cdot 2\text{HF}$ , which was found to be approximately  $4 \Omega$ , which was consistent with the results obtained from AC impedance.

On each of the non-graphite carbons, the actual potential being applied to the FDR was only about 6.0 V at the peak current density, due to losses in the system attributable to solution resistance. The difference of  $\sim 2.0$  V (in the present experimental configuration) reflects an inefficiency in the system, and may be even larger in industrial cells for reasons other than solution resistance, such as bus-bar contact resistance.

The CV curves of the vitreous carbon featured a noisy curve at potentials above 5.0 V consistent with the generation of larger, surface-blocking bubbles at high currents (compared to those on amorphous carbon samples), followed by their detachment from the surface (Fig. 5.13). The inhibited bubble detachment created a more significant fluctuation in current density at higher potentials. Reactions occurring at high potentials showed a measure of reversibility since the reverse sweep on the CV showed a trace of the forward-going sweep. Ohmic resistance was present on the vitreous carbon as well (as indicated by the shape of the curve), even though it was not as well defined due to the jagged peaks for fluorine bubble detachment.

While the first sweep in the CV of the graphite rod (Fig. 5.9) indicated that the reaction

was not completely reversible, the second sweep indicated that the electrode had been partially passivated by a thin  $\text{CF}_x$  film. In contrast, the reactions on the surface of the amorphous carbons were completely reversible, indicating that an insulating  $\text{CF}_x$  film had not formed on the surface. Thus, the FDR during voltammetry was limited by the electrode (and the passivating film) in the case of graphite, but the same reaction was limited by the electrolyte in the case of the amorphous carbons.

The decrease in the peak current densities indicate that over similar experimental exposures, the vitreous carbon was the most highly passivated, the graphite was partially passivated, and the amorphous carbons were not particularly passivated. The amorphous carbons were still able to pass a high current at the end of the polarization series. The high currents obtained on the vitreous carbon indicated that it was highly electroactive, but was easily passivated. While vitreous carbon was considered to be a perfectly amorphous carbon lacking any graphitic regions, the industrial amorphous carbons behave radically different, resisting the formation of a thick passivating layer. This passivating  $\text{CF}_x$  layer ultimately leads to the presence of an inhibiting fluorine gas film or bubble, and electrode polarization.

#### **6.1.4. Summary of Polarization Studies**

The potentiostatic studies conducted clearly indicate that the industrial amorphous carbons were the most suitable as electrodes for fluorine generation. The graphitic rods and vitreous carbon were ineffective for carrying out the FDR. These three samples were passivated at low potentials (5.0 V), and did not pass very much charge at higher potentials. A thick  $\text{CF}_x$  layer and gas film acted as a barrier to charge and mass transfer, severely limiting the current that could be sustained. In comparison, both the Toyo Tanso and Cameco carbons did not show a decrease in the ability to pass charge until 7.0 V. It should be noted, however, that due to ohmic drop at high current densities, the potential being applied towards the FDR was lower than the potential being applied to the system. Also, the potential drop across the system is larger at higher potentials because higher currents are obtained at this potential range in voltammetric sweeps where the applied potential is transient. The inefficiency caused by ohmic resistance means that if 6.0 V had been actually applied towards the FDR (without any loss to the system) the current

should be much higher. In potentiostatic experiments, ohmic resistance effects are minimized when the current reaches a steady state. This is because the  $I_{ss}$  is significantly lower than those obtained from CV, where the electrode surface is constantly changing with higher applied potentials. Toyo Tanso showed a slight decrease in  $I_{ss}$ , the Cameco carbon became significantly limited at 8.0 V. In stark contrast to the 450 C passed at 7.0 V, only 25 C was passed at 8.0 V on the Cameco carbon. Whereas the smoother surface of the Toyo Tanso sample promoted bubble detachment, the pores of the Cameco carbon may have become sites for the development of a stable gas film, resulting in much lower charge passed. Overall, the total charge over the course of the polarization experiments indicated that the Cameco and Toyo Tanso are the most effective carbons for fluorine generation.

The  $I_{ss}$  of the graphite rod and vitreous carbon showed a decreasing trend after 5.0 V, consistent with the smaller charge passed at higher potentials. The two graphite-PTFE samples showed a similar behavior, with the highest steady state current at 5.0 V, gradually decreasing towards 8.0 V. Although the Vulcan-PTFE samples showed an upward-going trend with higher potentials, the overall currents were two orders of magnitude smaller, indicating that these electrodes were not effective for fluorine generation. The two industrial amorphous carbons showed an upward-going trend for  $I_{ss}$  to applied potentials of 7.0 V, where the greatest amount of charge was passed. These indicated resistance to electrode passivation, since the FDR occurred at potentials as low as 4.0 V, yet the two materials were able to reach high currents even after the previous polarizations were applied.

Finally, the voltammograms provided a clear indication of the effect of the polarization experiments on the carbon electrodes. While the graphite rod underwent a decrease in the peak current density by a factor of 10, vitreous carbon had a 100-fold decrease in the current density. The two industrial amorphous carbons were still able to maintain a high current density following the polarization experiments, further confirming that the electrodes were not easily passivated even at high potentials. Thus, these experiments show the greater effectiveness of industrial amorphous carbons for fluorine generation compared to the graphitic carbons. Exfoliation was not observed on the graphite rod samples in any experiment.

## 6.2. Raman Spectroscopy

Raman spectroscopy is a particularly useful method for studying the intercalation of fluorine into graphite. The insertion of ionic fluorine increases the interlayer spacing between graphene layers, whereas the formation of ionic or covalent C-F bonds modifies the vibrational modes of adjacent C-C bonds. The general result is that for highly intercalated graphite (and amorphous carbons), there is a depression and broadening of the “ordered” carbon peak, as well as an increase and broadening of the “disordered” C-C vibrational mode. Broad peaks of the vibrational modes for amorphous or disordered carbons are due to the many strained and mixed bonding states present in the material.

The results of the immersion of graphite rod into molten KF·2HF suggested that intercalation occurred near the surface of the graphite rod, and that C-F bond formation was completely ionic in nature. A low degree of ionic C-F would increase the interlayer spacing between graphite layers, but would have little effect on the C-C planar  $sp^2$  bond, unlike what covalent C-F bonds would cause. The polarity of the C-C bond would remain largely unchanged, and so a shift in the ordered and disordered peak position would be minor, or in this case, remains unchanged. During bond formation, however, an electron transfers from the graphite to intercalated fluorine, affecting the C-C bond character [52,60]. This causes a lengthening of the C-C bond, a decrease in the vibrational energy, and an upshift in the vibrational mode (wave number).

A shift in the peak intensity position and change in  $I_O/I_D$  shows charge-dependence, rather than a potential-dependence. During preparation of the graphitic samples, almost 7 times more charge was passed at 6.0 V than at 8.0 V. A greater amount of charge suggests that more fluorine was intercalated in the process, resulting in a greater shift in peak position and change in  $I_O/I_D$ . In addition, passivation of the graphite surface inhibits the FDR, and limits the amount of intercalation that is possible. The FDR does not occur at potentials as low as 2.0 V (and only starts at 4.0 V), so there was no appreciable change in the Raman spectrum.

The absence of crystalline graphitic particles in the bulk material of amorphous carbons is consistent with the absence of change in the  $I_O/I_D$  and peak positions. A significantly larger amount of charge was passed on the amorphous carbons compared to that on the

graphite, but a corresponding change to the Raman spectrum was not observed (Table 5.2). Although it is possible that a small degree of intercalation could occur on the surface of the amorphous carbons (since graphitization may occur during manufacture of the carbons), any change to the surface was not detected by Raman spectroscopy. The technique may not have been sensitive enough to detect intercalation at the outer surface layers, and the penetration depth of the Raman laser may blur the surface measurements with those made deeper into the material.

The Raman spectra show that fluorine ions are capable of intercalation into the crystalline lattice of the graphite rod at all of the potentials tested. The largest shift in peak position and change in the  $I_O/I_D$  ratio occurs following polarization at 6.0 V, which also corresponds to the greatest amount of charge passed over the polarization period. The potential at which the greatest amount of charge is passed is likely the potential at which the highest level of intercalation occurs. Although the fluorine evolution reaction is most efficient at 6.0 V across all of the carbons tested, intercalation is completely absent on the industrial amorphous carbons due the lack of graphitization.

### **6.3. Electrochemical Impedance Spectroscopy**

#### **6.3.1. Capacitance and Surface Layer Relationship**

The electrochemical double-layer (region B in Figure 3.3) is dependent on the functional groups on the surface of the electrode. The electrical response of the electrochemical double-layer can be mixed with the response of a smooth, uniformly thick dielectric layer formed on the surface. If the double-layer capacitance is negligible compared to the surface layer, the double-layer capacitance can be related to the degree of passivation, or thickness of the  $CF_x$  layer that has formed on the surface of the electrode. This surface model can then be simplified into region B of Figure 3.3, where the  $CF_x$  passive film is electrically indistinguishable from the electrochemical double-layer. The thickness of the insulating  $CF_x$  layer,  $d$ , represented as a parallel plate capacitor, is given by the relationship [13]:

$$C = \epsilon_r \epsilon_o \frac{S}{d} \quad (17)$$

Where C is the capacitance,  $\epsilon_r$  is the dielectric constant of the material (for a  $\text{CF}_x$  layer taken as 2.1, the same as PTFE) [45],  $\epsilon_o$  is the electric permittivity constant, S is the surface area, and  $d$  is the thickness of the  $\text{CF}_x$  layer (Fig. 4.12). When the electrode is being passivated and the thickness of the  $\text{CF}_x$  layer increases, the material surface becomes more insulating, and the ability to pass electrons becomes more difficult (R1 increases). Thus, the capacitance measured at the edge of the  $\text{CF}_x$  layer decreases as the thickness of the passive layer increases. The capacitive properties (C1) decrease and the resistive components of the  $\text{CF}_x$  layer (R1) increases as the electrical double-layer thickness of the  $\text{CF}_x$  increases.

### 6.3.2. Discussion of the Capacitance and Surface Layer

The calculated double-layer thickness on the carbon electrodes were based on the circuit diagram presented in Figure 3.3. The model was a single representation of a partially passivated C/KF·2HF interface, and will change depending on the system under examination. Section 3.2.3. showed that a complex circuit model could be simplified and yield a reasonable approximation of the double-layer capacitance, depending on the frequency range to which the model is being fitted (Table 3.1). For the simplified model, the calculated values for  $\text{CF}_x$  layer thickness on the graphitic carbons (Table 5.3) were considered to be reasonable based on the results reported by Brown et al. [45]. The values for thickness of the  $\text{CF}_x$  layer on the amorphous carbons were unusual, since such high thickness values are uncommon, and no visible change in the amorphous carbons had occurred. While chemically fluorinated  $\text{CF}_x$  is light grey in colour, the amorphous carbons were still black following polarization at 8.0 V. The visual appearances of the carbon samples were not consistent with the calculated film thickness values. Thus, the equivalent circuit model of the surface of the amorphous carbon will need to be reassessed. It is likely that the circuit model is too simplistic to accurately represent the  $\text{CF}_x$  surface layer, and that error in the impedance measurements were the result of surface resistance, roughness, microstructure, or a non-uniform  $\text{CF}_x$  layer. For instance, the highest calculated  $\text{CF}_x$  film thickness values were obtained on the Cameco amorphous

carbon, which also had the most visible surface roughness (compared to Toyo Tanso or graphitic rods). A more representative circuit model that takes surface roughness into consideration might include a constant phase element (CPE), rather than a simple capacitor, to represent the capacitive properties of the  $CF_x$  layer.

Another explanation for the large calculated film thicknesses may be the assumption that the dielectric constant of the  $CF_x$  surface layer was the same as that for PTFE (2.1). The dielectric constant may be a significant source of error in the calculation of the film thicknesses, depending on how close the actual constant was for the  $CF_x$  layer. It is possible, however, that the dielectric constant of PTFE was suitable for the graphitic rods, but not the amorphous carbons, depending on the chemistry and distribution (uniform or patchy) of  $CF_x$  on the surface of the electrode. This may explain why the calculated thickness values on the amorphous carbons were unusually large, whereas the graphitic and vitreous carbon samples were smaller.

The substantial film on the vitreous carbon even after polarization at 4.0 V suggests that a thick passive film forms quickly on the surface of the electrode at low potentials, and limits the FDR during later polarizations. The thickness values observed following polarizations at 7.0 and 8.0 V on vitreous carbon may properly reflect the actual  $CF_x$  film present on the electrode, according to the decrease in peak current densities on the voltammetric sweeps following the polarization series (Fig. 5.13a and b). Although the surface area affects the measured capacitance, it does not appear to be a decisive variable in the capacitance measurements under the conditions studied (see Eq. (17)). The amorphous carbons, particularly the Cameco sample, had a rough surface which meant that the actual surface area was larger than the apparent (measured) area. The vitreous carbon, however, was smooth and lacked any visible porosity indicating that the actual surface area is very close to the geometric measured value. By this point, one would expect the amorphous carbon to have the largest capacitance values, while the vitreous carbon to have the smallest. Based on the values calculated in Table 5.3 for potentials above the FDR, the relationship between surface area and capacitance was not evident when different materials were considered.

The low  $\chi^2$  values indicate that the overall fitting of the model was in good agreement

with the experimental results. It is important to note, however, that the  $\chi^2$  does not account for fitting errors in individual components. In a few cases, errors in individual components (particularly R1 values) were larger than 100%, and thus represented a point of contention. A complete table of data values is presented in Appendix 3. There was an appreciable increase in the solution resistance (Rs) which may be consistent with a larger zone of depleted electrolyte (thus a lower conductivity) following polarizations to higher potentials. R1 values have a large degree of variation between the set of measurements on the same electrode, which may reflect the constantly changing  $CF_x$  layer that forms rapidly at higher potentials. Individual errors could be reduced with a more extensive manual fitting process, although the existing results show a reasonable trend in the capacitance values for polarizations up to 8.0 V (Table 5.3). In other cases, however, the unusually large capacitance values (in relation to the polarization potential) measured may not be attributed to errors in the fitting process. These deviations instead may reflect discrepancies in the experimental procedure, particularly when the EIS experiment was conducted after the end of the polarization experiment as previously described.

Unusually small calculated  $CF_x$  film thicknesses (based on capacitance values obtained during impedance measurements) were observed on different carbon materials at different points in the polarization series (Table 5.3). A possible explanation for the high capacitance values was a time-dependence of when the impedance measurement was made after the polarization experiment. The higher capacitance value may be caused by excess fluoride ions present on or intercalated in the surface dissociating or de-intercalating, which affects the localized chemistry. The movement of these species away from the interface decreases conductivity of the electrode, and the capacitance of the electrode increases. In addition, R1 and R2 values decrease as the concentration of fluoride in the electrolyte near the surface returns to the nominal concentration after being depleted during the polarization experiment. When the electrolyte is depleted, there is an increase in the resistance since fewer active species are available to carry current through the system. The electrolyte is replenished by diffusion, which is also a time-dependent process, and would also influence the impedance measurements of the C/KF·2HF interface. Thus, deviations in the trend that reflect the growth of the passivating layer also can be explained by a time-dependence of the EIS experiment after

polarization experiment was conducted. The deviation is caused by differences in fluoride and electrolyte concentration following polarization, and the physical forces required to re-establish the equilibrium.

#### 6.4. Galvanostatic Experiments

The potential decay curves at the start of the experiment shown in Figure 5.21 were not completely consistent with typical discharge curves reported in multiple publications [23,70]. This may be attributed to the overall lower fluorine content in the graphite rod samples compared to chemically fluorinated graphite powders. Thus, the electrochemically fluorinated graphite rods may be quickly depleted at the applied current densities. The depletion of fluorine in the graphite sample with the applied current density of  $0.75 \text{ mA/cm}^2$  occurred earlier than that at  $1.0 \text{ mA/cm}^2$ , possibly showing the variability in the intercalation process and concentration of intercalated species. More work is required to improve the sensitivity of this technique, since the depletion of intercalated fluorine was expected at  $0.25 \text{ mA/cm}^2$  based on the estimated fluorine content, but did not occur.

The large Tafel slope of  $0.81 \text{ mV/decade}$  (Fig. 5.22) indicated that the reaction was not a simple electron transfer. A simple electron transfer mechanism has a Tafel slope of only  $0.06 \text{ mV/decade}$ . The Tafel slope for the process in question further indicates the reduction and discharge of C-F was an irreversible process (and  $\text{CF}_x$  layers are considered to be non-reducible), and the reaction is not potential dependent. This may be explained by the low conductivity of the PC- $\text{LiClO}_4$ , since the exchange current density is dependent on the electrode and the solution.

The high initial discharge potential of the fluorinated graphite rod in Figure 5.21 suggested that the intercalated fluorine was ionically bonded, whereas the  $\text{CF}_x$  is primarily made up of covalently bonded fluorine atoms. Covalent C-F bonds are much stronger than ionic ones, and so the activity of the bond is much smaller, resulting in a lower potential during discharge. The fluorinated graphite rod had a higher discharge potential, likely due to the more ionic nature of the C-F bonds present. This may reflect the spectrum of covalent-to-ionic C-F bonds present in the graphite rod, compared with

the mainly covalent C-F bonds in the  $\text{CF}_x$ . In addition, the potential for the  $\text{CF}_x$  carbon paste electrode did not drop to the  $-1.0$  V value that was previously observed on the graphite rod. This may have occurred for two reasons: galvanostatic experiments are susceptible to ohmic drop effects (which are dependent on conductivity), and the measurements tend to be surface sensitive. The concentration of  $\text{LiClO}_4$  supporting electrolyte has a significant effect on the C-F discharge system: while Li is believed to take part in the discharge mechanism of fluorine by reacting to form a LiF salt, the perchlorate is used to make the PC conducting. The drop in the discharge potential for the  $\text{CF}_x$  carbon paste may have been caused by a high resistance in the electrode, which is not evident on the graphite rod. The source of surface effects is visible on the samples tested. Whereas the fluorinated graphite rod is passivated and smooth, but contains ionically intercalated species, the  $\text{CF}_x$  is highly covalent and the CPE surface is uneven. Fluorine is completely absent on the fresh graphite rod. The fluorine discharge potentials may vary greatly since the surfaces present are sufficiently different, that a direct comparison may not be possible. Also, the equilibrium potentials for the reactions are expected to be different on each electrode. The three carbons samples have different steady state potentials, namely  $-1.0$ ,  $-0.7$ , and  $0.5$  V, for the fluorinated graphite,  $\text{CF}_x$ , and fresh graphite, respectively (Fig. 5.23).

An attempt to optimize the conductivity of the CPE by modifying the ratio of insulating  $\text{CF}_x$  to conducting graphite powder was made. This would help increase the charge transfer at the conductive electrode surface. Despite adjustments to the composition of the CPE (increasing graphite powder content to increase conductivity), the resistance measured using a DC voltmeter was still large. This was likely due to the low conductivity of the PC- $\text{LiClO}_4$  electrolyte. The discharge potential for the  $\text{CF}_x$  carbon paste electrode appears to be roughly  $-0.7$  V (vs. Ag/AgI), which is considerably lower than that of the reported  $\text{CF}_x$  discharge potential values ( $\sim 3.0$  V vs. Li/LiClO<sub>4</sub>). In order to identify the source of this difference in discharge potential, additional studies are required to determine the effect of the reference electrode, conductivity, impurities, or moisture on the measured potentials. The  $2.0$  V difference in the decomposition potential of PC in the study ( $-1.1$  V vs Ag/AgI) compared to that reported in the literature ( $1.0$  V vs. Li/LiClO<sub>4</sub>) was attributed to the difference in the reference electrodes used, water

impurities in the PC, as well as low conductivity of the electrolyte. The low conductivity of the PC electrolyte may be the result of a low concentration of  $\text{LiClO}_4$  (the supporting electrolyte) in the PC (the perchlorate ion has limited solubility in PC if it becomes hydrated).

The curves in Figure 5.23 indicate that different C-F bonds are present in the two fluorinated carbon samples. Whereas the fluorinated graphite rod is expected to be predominantly ionic C-F groups, the  $\text{CF}_x$  is made up of covalently bonded C-F. The different discharge potential reflects the difference in bond type, as the more active ionic bonds yield a more positive discharge potential. Since there is not enough intercalated fluorine in the fluorinated graphite rod, the discharge reaction does not reach a steady state before it has been depleted. A small inflection point observed at  $\sim 100$  s was believed to be the point at which reducible intercalated fluorine was depleted from the graphitic material, and decomposition of PC began. The early depletion may also indicate that intercalation only occurred near the surface of the electrode, and so the discharge of fluorine occurred rapidly. Thus intercalation of atoms deeper into graphitic material becomes inhibited if the lattice near the surface has become saturated in fluorine atoms.

## 6.5. Discussion Summary

The experiments were designed to examine why non-graphitized (amorphous) carbon is used as electrodes in the industrial generation of elemental fluorine. Various analytical techniques were used to examine the physical and chemical changes that occur to the carbon surfaces before and after polarization in the  $\text{KF}\cdot 2\text{HF}$  electrolyte. The experiments required the selection of various carbon materials for comparison. The criterion used to differentiate the different carbon materials was the microstructure: namely, whether the material was graphitic (crystalline) or amorphous, and whether the material was porous or fully dense. The materials selected were categorized roughly into three categories: the graphitic carbons (graphite and carbon rod), the industrial amorphous carbons (Toyo Tanso and Cameco), and vitreous carbon. The main points of comparison used to evaluate the materials was whether the material was effective for the FDR, whether the

material was easily passivated, and whether or not a physical change occurred in the microstructure due to intercalation.

Since the goal of this project was to compare different carbon materials for fluorine generation, the comparison was based on their ability to pass charge effectively over a series of experiments. The amount of charge passed is representative of the amount of fluorine generation that could occur on a particular electrode. Although passivation and intercalation cannot be distinguished based on the amount of charge passed, the fraction of the overall charge for intercalation is assumed to be minor based on galvanostatic discharge measurements. The electrodes were polarized at potentials above the FDR potential ( $\sim 4.0$  V), and it was found that the amorphous carbons passed significantly more charge ( $\sim 7$  to 8 times more charge) than the graphitic carbons, and even more than vitreous carbon. The cyclic voltammetric (CV) sweeps conducted at the end of the polarization experiments indicated that the amorphous carbons had undergone the least amount of passivation of the three groups of carbons. This characteristic was defined by the change in the peak current density of the CVs, because not only were the industrial amorphous carbons more effective for fluorine generation, they were the least passivated over the course of the experiments. In an attempt to measure the thickness of the  $\text{CF}_x$  layer that had developed on the amorphous carbons, EIS was used to obtain a value of capacitance of the  $\text{CF}_x$  surface layer on the electrodes. Under the assumption that the  $\text{CF}_x$  double-layer had a basic resistive and capacitive character, the calculated thickness of the  $\text{CF}_x$  layer was  $0.15 \mu\text{m}$  on the Cameco carbon, and  $0.04 \mu\text{m}$  thick on the Toyo Tanso carbon. This was unusual because one would expect a visible change in the colour of the electrode; however, none was observed. Chemically fluorinated  $\text{CF}_x$ , for instance, is light grey in colour. On each of the carbons tested, however, the surfaces of the electrodes were actually darker than before they had been polarized (and not lighter).

In contrast, the graphitic carbons were much less effective at maintaining the FDR for long periods of time. The steady state currents indicated that the electrodes were passivated even during polarizations at  $5.0$  V, and that the CV results showed that the peak current densities were smaller by a factor of 10 following polarizations. Calculated  $\text{CF}_x$  film thickness values (based on EIS results) were only  $\sim 5$  nm thick. These results appeared to be much more consistent with the visual appearance of the fluorinated

graphitic samples, and those reported by Brown et al. [45]. The results suggest that while the equivalent circuit model used to represent the surface of the graphitic carbon may be suitable, it may not be applicable to all of the carbons tested (i.e., the amorphous carbons). In addition, the circuit model may even change for the same carbon sample depending on the degree of fluorination, if the structure and/or chemistry of the amorphous carbons (it would seem) were different from the graphitic carbons. There are multiple reasons why a simple, parallel-plate capacitor model may not apply to the amorphous carbons. First, the amorphous carbons had high surface roughness (especially the Cameco carbon). The simple capacitor model does not take variations in surface height into consideration, and the measured capacitance is an average of values taken from the peaks (closest to the opposing plate), and the bottom of pores (furthest from the opposing plate). Second, the circuit model assumed that a uniform surface layer was present over the entire, flat surface. Thus uneven coverage of the electrode surface by a passivating  $CF_x$  layer may have also been a contributing factor to the small capacitance values. Third, porosity in the electrode microstructure may have also been a contributing factor to the small capacitance values, since the model only focuses on the surface of the electrode, but the macrostructure may influence the measurement (depending on the frequency). It is possible that a constant-phase element (CPE) is a better representation of the surface (as opposed to a capacitor), because the CPE considers the deviation in capacitance from an ideal capacitor, due to non-uniform surface structures such as roughness or uneven  $CF_x$  formation.

Despite also being non-graphitic, vitreous carbon was, overall, unsuitable as an anode material for fluorine generation due to the high degree of passivation that occurred at low potentials. Although initial voltammetric sweeps indicated a high degree of surface activity, a  $CF_x$  layer quickly formed on the surface of the electrode during potentiostatic experiments, even at 4.0 V. In addition, the smooth, uniform surface of the vitreous carbon did not promote bubble detachment once a  $CF_x$  layer was present.

Based on the polarization results, it was clear that the non-graphitized carbon electrodes were much more effective for fluorine generation. While degradation of graphite electrodes are commonly cited as the reason why non-graphitized carbons were used [1,5,19], industrial amorphous carbons are simply able to pass more charge (and thus are

better at the FDR) than the graphitic carbons sampled. A possible explanation for this result is the presence of impurities (likely coal-tar pitch binder) in both of the amorphous carbon samples (as shown by the TGA), but its absence in the graphitic rods and vitreous carbon. It had been previously reported [51] that pitch material was poorly fluorinated, so its inclusion in amorphous carbon samples may have had a positive effect on disrupting the chemical uniformity of the carbon materials, and on promoting bubble detachment. Thus, it would also appear that from the different points of comparison (chemistry, microstructure, surface roughness), variations in chemistry have the biggest effect on the effectiveness of the carbon electrode for fluorine generation. This variation in surface chemistry would be consistent with the results of the work done with embedded metal fluorides [1,29,31] in carbon electrodes.

Next, it was found that the potential at which the FDR occurs at a much faster rate was ~5.0 V. In terms of the  $I_{ss}$  values, the total charge passed on each carbon sample at 4.0 V was less than 10 C. The capacitance values for the  $CF_x$  surface layers after the 4.0 V polarization did not change significantly from the initial, “fresh” electrode values. Thus, although the FDR occurs, it may occur at a very slow rate resulting in a degree of  $CF_x$  film formation. In addition, at 4.0 V, the electrolysis of water may still be occurring, and contribute to the overall charge that is passed. At 5.0 V, however, the  $I_{ss}$  values increased significantly on all of the carbons tested (relative to 4.0 V). As well, there was a change in the capacitance values on all of the carbon materials by two orders of magnitude, indicating that the surface underwent a greater change compared to the earlier polarization. This was attributed to the  $CF_x$  film formation. The Raman results had indicated that a change in the peak-intensity-ratios had occurred following polarization at 2.0 V, and even by simply immersing the sample in the electrolyte. Therefore, although high levels of intercalation may lead to the formation of covalent C-F bonds, it is less likely to occur during electrochemical fluorinations. This was because not only is a small fraction of the overall charge passed going towards intercalation, electrode surface coverage by a film or bubble limits the movement of ions to the surface itself, and intercalation into a solid material is a difficult process.

In order to obtain a measure of the inefficiency in industrial electrochemical fluorine generation cells, the resistance of the electrolyte was determined by different

electrochemical methods. The Ohmic resistance in electrolyte estimated from cyclic voltammetric sweeps using the amorphous carbons was approximately  $4 \Omega$ . This was consistent with the solution resistance values measured by the EIS experiments on all of the unfluorinated carbon samples (Appendix 3). These results bring into perspective the issue faced in industrial fluorine generation cells in which larger distances between electrodes will be affected more significantly by Ohmic resistance effects. This is only one source of inefficiency in this electrochemical system, but the overvoltages created by components such as bus-bar contact, cathode, and anode are all issues for industrial fluorine generation. This outlines the importance of conductivity in the molten salt electrolyte. This also indicates that the addition of a metal fluoride (or other suitable compound) into the melt could be a critical step in lowering the overvoltages in industrial cells. These metal fluorides have been reported to improve conductivity in the melt, improve the charge transfer characteristics of the electrodes themselves [21,26,29-31].

Finally, electrochemically fluorinated graphite rods were found to behave differently than the chemically fluorinated graphite powders ( $CF_x$ ). The RS results clearly indicated a change in the microstructure of graphite due to the intercalation of ions as more charge was passed on the electrodes. The RS of the  $CF_x$ , however, was completely Raman-inactive. This indicated that unlike the highly covalent C-F bonds in  $CF_x$  which are Raman inactive, the C-F bonds in the fluorinated graphite rods were still largely ionic and remained Raman active. It is also less likely that electrochemical fluorination yields covalently-bonded, intercalated C-F groups, because of the low concentration of fluorine atoms that are intercalated into the material during polarization. The discharge curve of the fluorinated graphite rod in PC appeared to have a small inflection point which was attributed to a change in the primary reaction occurring, from the discharge of intercalated fluorine to decomposition of the propylene carbonate. Due to the low degree of intercalation, however, the rod had been depleted before it could reach a steady rate of fluorine discharge. If the potential curve for the fluorinated graphite rod was extended, it is possible that the potential of the curve could match the  $CF_x$  CPE. Thus, the discharge of fluorine follows a similar process, whether the C-F bond is ionic or covalent. The lower discharge potentials for covalent C-F bonds reported in publications [50,65-69] may be consistent with the sharper decrease in potential at the start of the experiment for

the  $\text{CF}_x$ . The fluorinated graphite rod had a higher discharge potential, consistent with lightly fluorinated graphite powders reported in the literature [50,65-69]. Thus, it would appear that galvanostatic discharge experiments have the potential to be able to measure the amount of electrochemically intercalated fluorine in a graphitic sample. Unfortunately, the amount of electrochemical intercalation is low, and so sufficiently small discharge currents must be applied across the system for visible potential decays to become apparent. The same current applied to a sample of  $\text{CF}_x$  would be a slow and tedious experiment, unless the concentration of  $\text{CF}_x$  in the sample was sufficiently low.

## 7. Concluding Remarks

The examination of carbon anode materials for the electrochemical evolution of elemental fluorine in  $\text{KF}\cdot 2\text{HF}$  molten salt electrolyte was carried out. Five different commercial carbon materials were selected for comparison: two graphitic rods, two industrial amorphous carbons (Toyo Tanso, Cameco), and vitreous carbon. The physical and chemical properties were briefly examined to help explain the performance of each electrode for the fluorine discharge reaction (FDR). In the main set of experiments, the electrodes were polarized potentiostatically between 4.0 and 8.0 V to measure the amount of charge passed on each material as a measurement of the effectiveness for the FDR. A variety of analytical techniques were used to examine the properties of the materials before and after polarization in the electrolyte: thermogravimetric analysis (TGA), Raman spectroscopy, electrochemical impedance spectroscopy (EIS), and galvanostatic discharge studies. Several conclusions were drawn from the results:

- The industrial amorphous carbons were the most effective for the FDR, passing significantly more charge than the graphitic carbons for similar electrochemical exposures. The higher performance was believed to be attributed to the coal-tar pitch used as a binder in the amorphous carbons. Coal-tar pitch has been reported to be very poor at fluorination [51], and its inclusion into amorphous carbon appears to have made the material more resistant to passivation ( $\text{CF}_x$  film formation), which in turn made bubbles less adherent to the surface. Evidence for the resistance to passivation was the small change in peak current density for voltammetric sweeps following the polarization series, compared to those taken before exposure. In contrast, the graphitic and vitreous carbon samples were homogeneous carbon materials and were passivated easily at low potentials. This impacted the overall effectiveness (charge passed) of these two groups of carbon materials.
- EIS is a useful method for the estimation of  $\text{CF}_x$  surface film thicknesses using a simple circuit model for the graphitic and vitreous carbons. The estimation was not accurate for the amorphous carbons due to the effect of surface roughness on impedance measurements or incorrect assumptions made for the dielectric

constant of the  $\text{CF}_x$  film. In addition, a simple parallel resistor-capacitor circuit may not have been sufficient to represent the surface due to roughness or a patchy, non-uniform  $\text{CF}_x$  layer.

- Intercalation into graphitic materials occurs readily, even for a polycrystalline graphite rod immersed in molten  $\text{KF}\cdot 2\text{HF}$  electrolyte (without polarization). This work indicates that intercalation of fluorine into graphite is a charge-dependent process, rather than potential-dependent one. Intercalation does not occur on amorphous carbons due to the lack of graphitic content in the material. This was shown by the absence of an appreciable change in the peak intensity ratios ( $I_{\text{O}}/I_{\text{D}}$ ) or shift in the wavenumber in the Raman spectrum of polarized amorphous carbon electrodes.
- Galvanostatic discharge experiments can be used to estimate the amount of fluorine that was electrochemically intercalated into a material. The discharge potential on the fluorinated graphite rod was higher than commercial  $\text{CF}_x$  powders, but had a lower discharge capacity, because electrochemical intercalation of a solid graphite rod is expected to be minimal. Electrochemical fluorination yields more ionically bonded fluorine atoms compared to the chemically fluorinated  $\text{CF}_x$ , which contains mostly covalently bonded fluorine.
- The resistance of the electrolyte was determined to be  $\sim 4 \Omega$ . This was determined from two separate electrochemical techniques: cyclic voltammetry and AC Impedance. The resistance value obtained from impedance measurements was relatively constant among different non-exposed carbon materials used, showing a measure of precision in the electrochemical measurements.
- The design, construction, and operation of the electrolyte heater and electrochemical cell to carry out electrochemical fluorinations at elevated temperatures were also completed successfully.

All of the methods selected to examine carbon electrode materials for fluorine generation were largely successful. TGA could measure the amount of volatile species in a carbon material if the experiment is conducted in an Argon atmosphere. Raman spectroscopy can provide a measure of graphitic crystallinity in the carbon materials, as well as observe deformation of the lattice due to intercalation. Finally, galvanostatic discharge

studies can be used to study the electrochemical intercalation of fluorine atoms into a graphitic lattice.

## 8. Recommendations for Future Work

Additional work is proposed to develop a more complete understanding of the passivation process of carbon electrodes in a fluorine-rich environment. Long-term polarization experiments are required to produce samples that resemble industrial electrodes which have been polarized continuously for thousands of hours. This work may not be completely practical given two major limitations: one, there are safety and environmental concerns with evolving fluorine for long periods; and two, the limited size of the cell means that experiments are limited by the rate at which the electrolyte is being depleted. Experiments approaching even one hundred hours have not been carried out in the current laboratory setup.

An interesting result obtained for the Raman experiments in this thesis was the shift in the peak intensity ratios corresponding to the “graphitic” and “disordered” peak for the immersed graphite rod. Material removal studies may be used to determine the depth of intercalation of fluorine species into the graphite rod. This may determine the natural driving force for intercalation of species into graphite, and one would be able to compare it against electrochemically polarized samples.

The “fluidized layer” model of a polarized electrode surface may be further studied using EIS, to determine if this model is realistic given resistance and capacitance measurements. The ability to model the proposed fluidized gas layer in a reasonable circuit model may be used to confirm or refute the model, in conjunction with other analytical techniques.

The use of TGA may be an alternative method for measuring the amount of intercalated fluorine in a graphitic sample. The limitation in sample weight for TGA prevents the fluorinated carbon materials from being analyzed using this technique. Breaking or cutting off pieces of fluorinated carbon samples is not a practical method for measuring the amount of fluorine present, also because the depth of intercalation into graphite is currently not known.

An interesting direction in research concerns the embedding of metal fluorides in carbon electrodes, which have been shown to minimize or delay the onset of electrode passivation and/or polarization. This also applies in the case of the carbon-PTFE

embedded samples. Various analytical surface techniques may be able to measure or scan the surface of the carbons to determine if there is a localization effect caused by the presence of the embedded particles. Metal fluorides may improve the local conductivity around the particle or serve as regions of non-homogeneity to disrupt the formation of fluorine bubbles. Surface studies may also determine if the PTFE particles do indeed cause a repelling effect against the electrolyte as one may suspect from a (simulated) passivated surface. An interesting direction of this research would be to determine if the composition of evolved gases is related to the carbon anode material used to generate the gaseous species in the first place. The FDR is expected to yield a variety of fluorinated species, not just simply  $F_2$ , but also  $CF_4$ ,  $OF_2$ , etc. This may drive the formation of new carbon anode materials that preferentially produce fluorine gas at the expense of lesser, undesired products.

Another possible step is to determine the degree or effect of intercalation on the surface of amorphous carbon electrodes. Although these samples are predominantly non-crystalline, it is always common that microscopic particles of graphite may exist among amorphous carbons. Intercalation may alter the conductivity of the electrodes and improve the performance of amorphous carbons, without the detrimental effects of a disrupted crystal lattice from extensive intercalation.

Finally, a surface technique such as XPS may be used to study a passivated carbon to determine the extent of  $CF_x$  formation on the electrode. This may help determine the average surface coverage by patches of  $CF_x$ , and/or determine if existing  $CF_x$  layers grow thicker and denser, rather than cover more area of the electrode surface.

## 9. References

1. R.J. Ring and D. Royston (1973). "A review of fluorine cells and fluorine production facilities", Australian Atomic Energy Commission, Report# E281.
2. R.G. Cochran, N. Tsoulfanidis (1990). *The Nuclear Fuel Cycle: Analysis and Management* (2<sup>nd</sup> Ed.), American Nuclear Society, U.S.A., pp. 52-76, Chap. 3. and pp. 77-104, Chap. 4.
3. H. Moissan. Comptes rendus hebdomadaires des séances de l'Académie des sciences, **106**:547, 1888
4. P. Lebeau and C.R. Damiens. Proceedings of the National Academy of Sciences of the United States of America **181**:917, 1925
5. A.J. Rudge (1971). "Production of elemental fluorine by electrolysis" in *Industrial Electrochemical Processes*, A.T. Kuhn (Ed.), Elsevier, Amsterdam, pp. 1-69, Chap. 1.
6. G.H. Cady. "Freezing points and vapour pressures of the system potassium fluoride-hydrogen fluoride", Journal of the American Chemical Society **56**:1431, 1934
7. C.E. Housecroft and A.G. Sharpe (2005). *Inorganic Chemistry* (2<sup>nd</sup> Ed.), Pearson Education Limited, England
8. K. Kinoshita (1988). *Carbon: Electrochemical and physicochemical properties*. John Wiley & Sons, New York, NY.
9. H. Groult, D. Devilliers, M. Vogler, P. Marcus, and F. Nicolas. "Effect of chemical fluorination of carbon anodes on their electrochemical properties in KF-2HF", Journal of the Electrochemical Society **144**:3361, 1997
10. W.D. Callister (2005). *Fundamentals of Materials Science and Engineering* (2<sup>nd</sup> Ed.), John Wiley & Sons, Inc., U.S.A., Appendix B
11. G.M. Jenkins and K. Kawamura (1976). *Polymeric Carbons – Carbon Fibre, Glass and Char*, Cambridge University Press, Cambridge, England, p. 72
12. A.J. Bard (Ed.) (1976). *Encyclopedia of electrochemistry of the elements* (VII-1). Marcel Dekker, Inc., New York, NY.
13. C.G. Zoski (2007). *Handbook of electrochemistry*. Elsevier, Amsterdam, Netherlands

14. J. Robertson. "Amorphous carbon", *Advances in Physics* **35**:317, 1986
15. D.R. McKenzie. "Tetrahedral bonding in amorphous carbon", *Reports on Progress in Physics* **59**:1611, 1996
16. F.A. Cotton, G. Wilkinson, C.A. Murillo, and M. Bochmann (1999). *Advanced Inorganic Chemistry* (6<sup>th</sup> Ed.), John Wiley & Sons, Inc., U.S.A., pp. 547-85, Chap. 14
17. H. Groult, F. Lantelme, M. Salanne, C. Simon, C. Belhomme, B. Morel, and F. Nicolas. "Role of elemental fluorine in nuclear field", *Journal of Fluorine Chemistry* **128**:285, 2007
18. C.B. Amphlett, L.W. Mullinger, and L.F. Thomas. "Some physical properties of uranium hexafluoride", *Transactions of the Faraday Society* **44**:927, 1948
19. H. Groult, C. Simon, A. Mantoux, F. Lantelme, and P. Turq. (2005) "Experimental and theoretical aspects of the fluorine evolution reaction on carbon anodes in molten  $\text{KF}\cdot 2\text{HF}$ " in *Fluorinated Materials for Energy Conversion*, T. Nakajima and H. Groult (Eds.), Elsevier, Oxford, pp. 1-30, Chap. 1.
20. K. H. Lieser (2007). "Nuclear Energy, Nuclear Reactors, Nuclear Fuel and Fuel Cycles" in *Nuclear and Radiochemistry: Fundamentals and Applications*, Wiley-VCH Verlag GmbH, Weinheim, Germany, Chap. 11
21. D. Devilliers, B. Teisseyre, and M. Chemla. "Electrolytic generation of fluorine with  $\text{KF}\cdot 2\text{HF}$  melts containing  $\text{AlF}_3$  or  $\text{LiF}$ ", *Electrochimica Acta* **35**:153, 1990
22. I. Crassous, H. Groult, F. Lantelme, D. Devilliers, A. Tressaud, C. Labrugere, M. Dubois, C. Belhomme, A. Colisson, and B. Morel. "Study of the fluorination of carbon anode in molten  $\text{KF}\cdot 2\text{HF}$  by XPS and NMR investigations", *Journal of Fluorine Chemistry* **130**:1080, 2009
23. A. Hamwi and I. Al Saleh. "Graphite oxyfluoride: behaviour as electrode material in lithium batteries", *Journal of Power Sources* **48**:311, 1994
24. T. Nakajima and M. Touma. "Surface free energy and chemical bonding of fluorine-graphite intercalation compounds", *Journal of Fluorine Chemistry* **57**:83, 1992
25. H. Groult, D. Devilliers, M. Vogler, C. Hinnen, P. Marcus, and F. Nicolas. "Electrochemical behaviour and surface analysis of crude and modified carbon

- electrodes for fluorine production”, *Electrochimica Acta* **38**:2413, 1993
26. T. Nakajima, T. Ogawa, and N. Watanabe. “Effect of a trace of water and solid LiF on anode effect in the KF<sub>2</sub>HF melt”, *Journal of the Electrochemical Society* **134**:8, 1987
  27. T. Nakajima, T. Ogawa, and N. Watanabe. “Graphite anode reaction in the KF<sub>2</sub>HF melt”, *Journal of Fluorine Chemistry* **40**:407, 1988
  28. H. Imoto, T. Nakajima, and N. Watanabe. “A study of the anode effect in KF-2HF system. I. ESCA spectra of carbon and graphite anode surfaces”, *Bulletin of the Chemical Society of Japan* **48**:1633, 1975
  29. T. Nakajima, M. Kawaguchi, and N. Watanabe. “Electrical conductivity and chemical bond of graphite intercalation compound with fluorine and metal fluoride”, *Solid State Ionics* **11**:65, 1983
  30. N. Watanabe. “Electrochemical application of fluorine chemistry”, *Journal of Fluorine Chemistry* **22**:205, 1983
  31. T. Tojo, J. Hiraiwa, M. Dohi, Y.-B, Chong. “A novel carbon electrode impregnated by molten metal fluoride for the production of fluorine”, *Journal of Fluorine Chemistry* **57**:93, 1992
  32. H. Groult and D. Devilliers. “Fluorine evolution reaction in KF·2HF: influence of Ni-doping particles on the electrochemical properties of the carbon-fluorine surface film”, *Journal of Fluorine Chemistry* **87**:151, 1998
  33. T. Nakajima, M. Kawaguchi, and W. Watanabe. “Graphite intercalation compound of fluorine with lithium fluoride”, *Synthetic Metals* **7**:117, 1983
  34. W.V. Childs and G.L. Bauer. “Improvements in fluorine generation: amorphous carbon anodes with vertical channels”, *Journal of the Electrochemical Society* **142**:2286, 1995
  35. L. Bai, and B.E. Conway. “Electrochemistry of anodic F<sub>2</sub> evolution at carbon electrodes: bubble adherence effects in the kinetics at rotating cone electrodes”, *Journal of Applied Electrochemistry* **18**:839, 1988
  36. H. Groult, D. Devilliers, S. Durand-Vidal, F. Nicolas, and M. Combel. “Electronic properties of passivating compounds: application to the fluorine evolution reaction”, *Electrochimica Acta* **44**:2793, 1999

37. H. Groult, S. Durand-Vidal, D. Devilliers, and F. Lantelme. "Kinetics of fluorine evolution reaction on carbon anodes: influence of the surface C—F films", *Journal of Fluorine Chemistry* **107**:247, 2001
38. M. Chemla and D. Devilliers. "Study of  $CF_x$  passivating layers on carbon electrodes in relation to fluorine production", *Journal of the Electrochemical Society* **136**:87, 1989
39. H. Groult. "Electrochemistry of fluorine production", *Journal of Fluorine Chemistry* **119**:173, 2003
40. L. Bai and B.E. Conway. "Electrochemistry of anode fluorine gas evolution at carbon electrodes: part III characterization of activated carbon anodes following onset of the 'anode effect'", *Journal of Applied Electrochemistry* **20**:925, 1990
41. H. Groult and D. Devilliers. "Fluorine evolution at carbon/KF-2HF interface", *Journal of Fluorine Chemistry* **101**:263, 2000
42. F. Lantelme and H. Groult. "Interfacial properties and gas bubble formation during the electrolytic preparation of fluorine", *Journal of the Electrochemical Society* **151**:D121, 2004
43. D. Devilliers, B. Teisseyre, H. Groult, and F. Lantelme. "Production of fluorine with pulsed currents", *Journal of Applied Electrochemistry* **22**:765, 1992
44. H. Groult and F. Lantelme. "Study of the mass transfer at fluorine-evolution carbon electrodes", *Journal of the Electrochemical Society* **148**:E13, 2001
45. O.R. Brown, B.M. Ikeda, and M.J. Wilmott. "Anodic films on fluorine anodes: the nature of fluorine overvoltage", *Electrochimica Acta* **32**:1163, 1987
46. L. Bai and B.E. Conway. "Electrochemistry of anode fluorine gas evolution at carbon anodes: part II studies on the 'CF' film by the current-interruption, AC impedance, ESCA and Auger techniques", *Journal of Applied Electrochemistry* **20**:916, 1990
47. D. Devilliers, B. Teisseyre, H. Groult, and M. Chemla. "Production of fluorine with large amplitude AC signals in KF·2HF melts", *Material Science Forum* **73-75**:381, 1991
48. H. Imoto, K. Ueno, and N. Watanabe. "A study of the anode effect in KF-2HF system. III. Influence of bath temperature and surface tension and addition of

- fluoride particles on the occurrence of the anode effect”, Bulletin of the Chemical Society of Japan **51**:2822, 1978
49. H. Groult, D. Devilliers, F. Lantelme, J.-P. Caire, M. Combel, and F. Nicolas. “Origin of the anodic overvoltage observed during fluorine evolution in KF-2HF”, Journal of the Electrochemical Society **149**:E485, 2002
  50. T. Nakajima (2005). “Applications of fluorinated carbon materials to primary and secondary lithium batteries”, *Fluorinated Materials for Energy Conversion*, T. Nakajima and H. Groult (Eds.), Elsevier, Oxford, pp. 31-60, Chap. 2.
  51. M.J. Root, R. Dumas, R. Yazami, and A. Hamwi. “The effect of carbon starting material on carbon fluoride synthesized at room temperature”, Journal of the Electrochemical Society **148**:A339, 2001
  52. L.B. Ebert. “Intercalation compounds of graphite”, Annual Review of Materials Science **6**:181, 1976
  53. U. Hoffmann and A. Frenzel. Z. Elektrochem, **37**:613, 1931
  54. A. Schleede and M. Wellmann. Z. Phys. Chem. **18**:1, 1932
  55. H. Touhara and F. Okino. “Property control of carbon materials by fluorination”, Carbon **38**:241, 2000
  56. T. Nakajima, M. Tohma, and Y. Kawabata. “Intercalation of fluorine into graphite in the KF·2HF melt”, Material Science Forum **73-75**:483, 1991
  57. A.M. Panich. “Nuclear magnetic resonance study of fluorine-graphite intercalation compounds and graphite fluorides”, Synthetic Metals **100**:165, 1999
  58. A.M. Panich, T. Nakajima, H.-M. Vieth, A.F. Privalov, and S.D. Goren. “Nuclear magnetic resonance study of fluorine-graphite intercalation compounds”, Journal of Physics: Condensed Matter **10**:7633, 1998
  59. V. Gupta, T. Nakajima, B. Zemva. “Raman scattering study of highly fluorinated graphite”, Journal of Fluorine Chemistry **110**:145, 2001
  60. V. Gupta, T. Nakajima, Y. Ohzawa, and B. Zemva. “A study on the formation mechanism of graphite fluorides by Raman spectroscopy”, Journal of Fluorine Chemistry **120**:143, 2003
  61. A.M. Panich and T. Nakajima. “Physical properties and C-F bonding in fluorine-graphite intercalation compounds as seen by NMR”, Molecular Crystals and

Liquid Crystals **340**:77, 2000

62. G. Nanse, E. Papirer, P. Fioux, F. Moguet, and A. Tressaud. "Fluorination of carbon blacks: an x-ray photoelectron spectroscopy study: I. a literature review of XPS studies of fluorinated carbons. XPS investigations of some reference compounds", Carbon **35**:175, 1997
63. T. Tojo, J. Hiraiwa, Y. Chong, and N. Watanabe. "Low polarization electrode impregnated with molten metal fluorides in fluorine cell", Materials Science Forum **73-75**:609, 1991
64. J. Li, K. Naga, Y. Ohzawa, T. Nakajima, A.I. Shames, and A.M. Panich. "Effect of surface fluorination on the electrochemical behaviour of petroleum cokes for lithium ion battery", Journal of Fluorine Chemistry **126**:265, 2005
65. N.D. Leifer, V.S. Johnson, R. Ben-Ari, H. Gan, J.M. Lehn, R. Guo, W. Lu, B.C. Muffoletto, T. Reddy, P.E. Stallworth, and S.G. Greenbaum. "Solid-state NMR studies of chemically lithiated  $CF_x$ ", Journal of the Electrochemical Society **157**:A148, 2010
66. A. Hamwi, M. Daoud, and J.C. Cousseins. "Graphite fluorides prepared at room temperature 2. A very good electrochemical behaviour as cathode material in lithium non-aqueous electrolyte cell", Synthetic Metals **30**:23, 1989
67. D. Devilliers, B. Teisseyre, M. Chemla, N. Watanabe, and T. Nakajima. "Electrochemical reduction of some graphite fluorides in propylene carbonate", Journal of Fluorine Chemistry **40**:1, 1988
68. J. Giraudet, C. Delabarre, K. Guerin, M. Dubois, F. Masin, and A. Hamwi. "Comparative performances for primary lithium batteries of some covalent and semi-covalent graphite fluorides", Journal of Power Sources **158**:1365, 2006
69. T. Nakajima, M. Koh, V. Gupta, B. Zemva, and K. Lutar. "Electrochemical behaviour of graphite highly fluorinated by high oxidation state complex fluorides and elemental fluorine", Electrochimica Acta **45**:1655, 2000
70. T. Nakajima, V. Gupta, Y. Ohzawa, H. Groult, Z. Mazej, and B. Zemva. "Influence of cointercalated HF on the electrochemical behaviour of highly fluorinated graphite", Journal of Power Sources **137**:80, 2004
71. T. Nakajima, D. Devilliers, and M. Chemla. "Preparation, structure and reduction

- of some graphite intercalation compounds”, *Journal of Fluorine Chemistry* **46**:461, 1990
72. T. Nakajima, V. Gupta, Y. Ohzawa, H. Iwata, A. Tressaud, and E. Durand. “Electrochemical properties and structures of surface-fluorinated graphite for the lithium ion secondary battery”, *Journal of Fluorine Chemistry* **114**:209, 2002
73. R. Santhanam (personal discussion), 2011
74. N. Watanabe. “Two types of graphite fluorides,  $(CF)_n$  and  $(C_2F)_n$ , and discharge characteristics and mechanisms of electrodes of  $(CF)_n$  and  $(C_2F)_n$  in batteries”, *Solid State Ionics* **1**:87, 1980
75. H. Imoto and N. Watanabe. “A study of the anode effect in KF-2HF system. II. Difference in anodic behaviour between edge plane and layer-plane of pyrolytic graphite”, *Bulletin of the Chemical Society of Japan* **49**:1736, 1976

## Appendices

### *Appendix 1:*

#### **Raman Spectroscopy**

Raman spectroscopy is an analytical technique that is used to measure molecular vibrations of various functional groups at infrared frequencies, induced by a beam of high-intensity photons. Raman is functionally similar to Infrared (IR) spectroscopy; however, Raman is a scattering method whereas IR is an absorption (transmission) method. The difference in the mechanism gives rise to what is referred to as, primarily, “Raman active” signals or “IR active” signals, derived from particular vibrational modes of various functional groups.

Raman active vibrations (or, the Raman effect) arises when the electron distribution in bonds around a molecule are distorted by the incident laser beam of visible light, which subsequently causes the light to scatter. The scattered light may be elastic or inelastic. Elastically scattered light (where the energy of the scattered light is identical to that of the incident beam) is called Rayleigh scatter, whereas the much smaller fraction of inelastically scattered light is called Raman scatter (or, effect). The associated change in wavelength of the inelastically scattered light is related to the energy involved in getting the molecule to vibrate. The Raman signals observed are particular to the molecule under examination. Although both Raman and IR occur in the same frequency range, the mechanistically different effects mean that the Raman activity of a given vibrational mode may differ markedly from its IR activity. Thus certain peaks may occur in one spectrum but be absent in the other. Since different bonds have characteristic vibrational frequencies, the resulting Raman and IR signals reflect the bonds present in the molecule, and various chemical and/or structural features. Whereas polar functional groups with low symmetry generally give strong IR signals, molecules with polarisable functional groups with high symmetry generally give strong Raman signals.

A Raman spectra is acquired by irradiating a sample with a laser source of visible or

near-IR monochromatic radiation. During irradiation, the spectrum of the scattered radiation is measured at an angle (normally 90°) relative to a spectrometer. Although the change in vibrational modes of the molecule produce a weak signal, the intensity of Raman bands are only 0.001% of the intensity of the source, there are many detectors for visible or near-IR signals currently available which are sensitive enough for this application. A particular problem with Raman spectroscopy is that continuous exposure to high intensity beams in a single position may lead to a charging effect on the specimen, which may lead to radiation damage at the scanned area. A depth resolution of 1 – 5 µm is achievable with Raman spectroscopy.

### **Thermogravimetric Analysis**

Thermogravimetric analysis (TGA) is a technique that measures the mass of the sample against time or temperature while the temperature is changed under a particular atmosphere. This method is useful for determining the purity of a sample and studying decomposition reactions. The graph of the resultant change in mass with respect to temperature is called a thermogravimetric curve. TGA tests may be run in a gradient temperature program or isothermally, under the flow of various gases or in air. The weight loss profile can be analyzed for the amount of or percentage weight loss at any given temperature, as well as the amount of or percentage of noncombusted material at some final temperature. TGA may also be used to measure the heat exchange in relation to the decomposition of a compound upon heating. Each downward step in the TGA trace corresponds to a weight loss due to the loss of various volatile gases and liquids present in the sample.

### **X-ray Diffraction**

X-ray diffraction (XRD) is a technique based on the elastic scattering of X-rays against atoms of a crystallographic plane to determine the physical dimensions of a crystalline structure. It is a non-destructive technique, and operates on the nanometre scale based on the interatomic spacing of atoms within the crystal. The two main types of XRD are X-

ray crystallography and X-ray powder diffraction. X-ray crystallography is a technique that is used to examine the structure of a single crystal. When the incident X-ray hits the single crystals of the sample, the electron beam is reflected at a particular angle that is unique to the crystallographic planes of the material. The resulting secondary beam is then captured by a detector. A beam of X-rays are directed at the crystal, and the intensity of the X-rays diffracted from the sample is recorded as a function of angular movement of both the detector and the sample. The diffraction pattern produced can be analyzed to reveal crystal details such as the spacing in the crystal lattice, bond lengths and angles. Other features that may be identified include crystal size, purity, and texture of the sample. In some cases, a single pure crystal cannot be obtained and so X-ray powder diffraction is used instead. This technique can still yield important information about the crystalline structure, such as crystal size, purity and texture, but the data may not be as complete as X-ray crystallography. The sample under investigation is usually ground down into a fine microcrystalline powder first. In some cases, the sample must be rotated to obtain the optimal diffraction pattern. XRD is an effective method of measuring the change in crystal structure due to the movement of species into, or out of, the unit cell of the crystal. A depth resolution of  $20 \text{ \AA} - 30 \text{ \mu m}$  is achievable with XRD.

## *Appendix 2:*

### **Preparation of Carbon-PTFE Electrode Samples by Sol-Gel Method**

[73] R. Santhanam (personal communication)

- Powdered Vulcan XE72 carbon (Cabot Corp.) or graphite powder was mixed with PTFE powder for the desired PTFE content
- The carbon-PTFE powder mixture was mixed with a 3-to-1, methanol-to-water solution ratio to produce a slurry
- The carbon-PTFE slurry was stirred overnight in a covered beaker
- The solvent was then left to evaporate slowly in open air, without heating
- The carbon-PTFE gel residue was left to dry at room temperature for 6 hours, followed by drying at 80 °C for 12 hours in an oven
- When dried, the gel was ground further using a mortar and pestle
- One gram of the carbon-PTFE compound was placed in a die and plunger for pelletizing the material
- The die and plunger was placed onto a hot pellet press (Carver standard bench top laboratory press) and the platens were lowered and heated to allow the die and plunger equilibrate to 250 °C
- A pressure of 7500 psi was then applied to the sample for 5 minutes
- The die and plunger was left to cool to room temperature before the pellet was carefully removed from the die
- A 1 inch diameter pellet with a thickness of 1 mm was produced

*Appendix 3:*

**Table A3.1: Full Table of Fitted Data for EIS Results**

Carbon Sample	Polarization Potential (V)	Rs ( $\Omega$ )	Capacitance ( $\mu\text{F}/\text{cm}^2$ )	R1 ( $\Omega$ )	$\chi^2$
Graphite Rod	Initial	3.11	15.5	12.5	$3.76 \times 10^{-3}$
	4	3.13	13.3	1.63	$1.74 \times 10^{-3}$
	5	4.103	1.74	17.6	$1.08 \times 10^{-2}$
	6	3.35	0.34	797	$1.13 \times 10^{-3}$
	7	8.21	1.45	11.2	$1.09 \times 10^{-2}$
	8	35.3	0.28	1130	$2.06 \times 10^{-4}$
	Carbon Rod	Initial	3.98	15.7	6.22
4		4.99	13.3	1.58	$1.01 \times 10^{-3}$
5		16.1	0.44	12.0	$3.05 \times 10^{-2}$
6		6.60	1.35	10.2	$1.78 \times 10^{-2}$
7		5.70	1.49	3.94	$9.30 \times 10^{-3}$
8		8.74	0.94	6.19	$1.46 \times 10^{-2}$
Toyo Tanso Amorphous Carbon		Initial	3.84	28.9	854
	4	4.13	23.3	1.83	$8.30 \times 10^{-4}$
	5	13.7	0.09	1480	$8.39 \times 10^{-3}$
	6	24.1	8.05	2.65	$1.30 \times 10^{-3}$
	7	19.6	0.06	2070	$4.16 \times 10^{-3}$
	8	29.4	0.08	1470	$1.86 \times 10^{-3}$
	Cameco Amorphous Carbon	Initial	6.23	17.3	2.90
4		11.4	11.4	4.20	$1.55 \times 10^{-3}$
5		31.8	0.11	395	$9.43 \times 10^{-3}$
6		46.5	0.03	4030	$3.01 \times 10^{-3}$
7		69.5	0.02	2340	$1.83 \times 10^{-2}$
8		54.3	0.02	3300	$5.99 \times 10^{-2}$
Vitreous Carbon		Initial	2.33	2.81	350
	4	2.48	0.48	508	$1.16 \times 10^{-3}$
	5	2.59	0.42	1990	$2.14 \times 10^{-4}$
	6	3.37	2.04	14.10	$1.43 \times 10^{-2}$
	7	3.36	0.11	1470	$7.24 \times 10^{-2}$
	8	4.76	0.10	893	$7.34 \times 10^{-3}$